NUMERICAL AND EXPERIMENTAL STUDY OF MARANGONI FLOW ON SLAG-LINE DISSOLUTION OF REFRACTORY

NUMERICAL AND EXPERIMENTAL STUDY OF MARANGONI FLOW ON SLAG-LINE DISSOLUTION OF REFRACTORY

By YI CHEN, B.A.

The Thesis Submitted to the School of Graduate Studies in Partial Fulfillment of the Requirements for the Degree Doctor of Philosophy

McMaster University, December 2011

DOCTOR OF PHILOSOPHY (2011) McMaster University

(Materials Science and Engineering) Hamilton, Ontario

TITLE: Numerical and Experimental Study of Marangoni Flow on Slag-Line Dissolution of Refractory

AUTHOR: Yi Chen, B.A.(Zhejiang University)

SUPERVISORS: Professor K.C. Coley and Professor M.S. Hamed

NUMBERS OF PAGES: vi, 150

ABSTRACT

The local corrosion of refractories at the slag/gas interface is a serious problem that limits the life of the refractories. Although, there have been several studies focused on understanding the Marangoni effect on the refractory dissolution process, there is little quantifiable analysis available. The aim of this study is to establish a better fundamental understanding of refractory dissolution mechanisms, and develop appropriate models for predicting the extent and rate of slag-line dissolution.

In the first part of this research, experimental studies using a high temperature dip technique were performed: MgO refractory in SiO_2-CaO-FeO_x-MgO slag and Al_2O_3-SiO_2-CaO-FeO_x-MgO. The experiments were conducted at varies temperature. There was significant evidence of a spinel phase formed at the slag/refractory interface for slags containing 20wt.% Al_2O_3. This existence of the spinel seems to have retarded the dissolution of the refractory. The decrease in erosion rate in the presence of spinel is in proportion to the decrease in the equilibrium MgO concentration at the slag/solid interface. The activation energy is calculated from the relationship of effective mass transfer coefficient vs. temperature and found in the range of mass transfer activation energy.

The second part of this search is developing a numerical model to predict the slag-line dissolution. An effective algorithm for analysis of unsteady Marangoni convection in

refractory slag line dissolution has been developed. The results show that the Marangoni effect plays a very important role in slag-line erosion at this condition; both the moving boundary condition and curved surface condition have significant effects on the slag-line erosion rate. The comparison of experimental and numerical results shows that the model can predict the refractory maximum corrosion distance caused by Marangoni flow at the slag line. However, the eroded material volume was predicted within 20~30% deviation.

ACKNOWLEDGEMENTS

I would like to express my sincerest gratitude to my supervisors, Prof. Kenneth Coley and Prof. Mohamed Hamed. They have supported me throughout my thesis with their patience and knowledge. I attribute my PhD degree to their encouragement and effort and without them this thesis would not have been completed.

I am deeply grateful to my ex-supervisor Prof. Geoffrey Brooks. He gives me the opportunity and confidence to begin this work.

I would like to thank you my committee member Prof. Gordon Irons for his support throughout this work. I am grateful for the assistant of Dr. Sharon Nightingale at University of Wollongong, Wollongong, Australia. She gives her valuable advice and provides one set of experimental samples.

I am indebted to many researchers, technical staffs and student colleagues. I am especially grateful to Dr. Fuzhong Ji, Jim Garrett and Graham Bishop for their technical assistance. Much respects for my officemates, Jianghua Li, Muhammad Rhamdhani, Kumar Krishnapisharody, Mansoor Barati, Takayuki Kaneyasu, and Ho Yong Hwang, thanks for providing a fun and truly helpful environment to learn.

I wish to thank the McMaster Steel Research Center for financial support. I would also like to thank Sharcnet for providing computer facilities for the numerical model.

My profound love and appreciation go to all members of my family for their encouragement and support, my Mom and Dad, Xiaofang Lin and Mao Chen; my brother Longbin Chen. To my family I dedicate this thesis.

Table of Content

List of Figures and Tables

Nomenclature

A	Reaction area
C	Concentration
Cs	Saturation concentration
D	Diffusion coefficient
E	Dissolution rate
Grc	Grashof number for concentration
h	Mapping function for the dissolvable rod
hz	Mapping function for the top surface
Ma	Marangoni number
Re	Reynolds number
S	Spreading coefficient
T	Temperature
t	Time
u	Velocity
βc	Concentration expansion coefficient
γ	Surface tension gradient
δ	Boundary layer thickness
ξ	Coordinate in radius direction

η	Coordinate in vertical irection
ϑ	Contact angle
μ	Viscosity
υ	Kinematic viscosity
ρ	Density
σ	Surface tension
τ	Shear stress
ψ	Stream function
Ω	Vorticity

Chapter 1 Introduction

Interfacial phenomenon is an important field of study in high temperature materials processing. Interfacial phenomena influence heterogeneous reaction rates and mass transfer away from interfaces.[1] An interface between two fluid phases can move spontaneously under the influence of interfacial tension gradients. Such interfacial motion is named the "Marangoni effect".[2] An interfacial tension gradient between two points on the interface provides a driving force for fluid flow towards the region of high interfacial tension. The fluid recirculates in the bulk, creating Marangoni flow. The interfacial tension gradient can be due to concentration, temperature or electrochemical potential gradients.[3] The Marangoni effect plays a major role in high temperature processing such as casting, crystal growth and welding.[4] This study focuses on the effect of Marangoni flow on refractory dissolution at the slag-gas interface.

Refractories are used in pyrometallurgical vessels and glass tanks for their high thermal shock resistance, ability to withstand high temperatures and aggressive chemical environment. In operation, refractories are degraded due to high temperatures, mechanical stress, and corrosive fluids. The refractories are often degraded locally at the slag/gas or slag/metal interface.[5] The local corrosion of refractories at the slag/gas interface is a serious problem that limits the life of the refractories.

When oxide refractories contact a molten slag, if the dissolution of refractory leads to an increase in surface tension of the slag, the region of the slag film in longer contact with the refractory will have higher surface tension and Marangoni flow will occur towards these regions. It has been observed that Marangoni flow can greatly accelerate the corrosion rate of refractory at slag/gas interface.[6]

Although, there have been several studies focused on understanding the Marangoni effect on the refractory dissolution process, there is little quantifiable analysis available. The aim of this study is to establish a better fundamental understanding of refractory dissolution mechanisms, and based on this, develop appropriate models for predicting the extent and rate of slag-line dissolution.

This study is based on experiments using a high temperature dip technique and numerical modeling simulation. Various slag compositions, reaction temperatures, and reaction times have been studied. A numerical model will be developed to simulate the flow and to predict the slag line erosion rate subject to the Marangoni effect.

Organization of the thesis:

This thesis presents a literature review, experimental results, numerical modeling, modeling discussion, the comparison of experimental results and modeling results, and finally a conclusion. Chapter 1 describes the motivation for this study; as well as the objectives and structure of the research. Chapter 2 provides a review of previous work

pertaining to this study. In Chapter 3, the experimental procedure is described in detail. This chapter also presents the experimental results and analysis of the dissolution kinetics. In chapter 4, a numerical model is developed to simulate the flow and the evolution of the erosion profile. Chapter 5 gives a comparison of the experimental results and numerical results. In chapter 6, a summary of the findings is presented and important conclusions are drawn.

Chapter 2 Literature Review

An outline of the previous studies relevant to the subject of the current study is presented in 7 sections of this chapter. Section 1 is allocated to describing the structure and nature of metallurgical slags and the effect of slag properties on refractory degradation. In the second section, a review is made of previous studies of the degradation mechanism of refractories. Section 3 provides review of the dissolution mechanism of MgO refractory. In section 4, a review is made of previous studies on the Marangoni effect. Section 5 provides a review of works on in refractory slag-line dissolution. Section 6 reviews the numerical studies in refractory slag-line dissolution. Section 7 reviews the numerical methods to solve moving boundary problems.

2.1 Slag Structure:

Liquid slags contain different oxides, (e.g. CaO, SiO_2, Al_2O_3, FeO, etc.), flurorides (e.g. CaF_2), and sulphides (e.g. CaS) at high temperatures, typically above 1200K. Slags are important by-products of metallurgical processes. They play an important role in metal production and refining. There have been various investigations of physical-chemical properties of slags. [4,5,7]

The nature of molten slags has been discussed in the literature in terms of two different theories, the molecular and the ionic.[7] In the molecular theory, the liquid slag constituents are assumed to exist as uncharged molecules such as SiO_2, CaO, FeO, etc. and the interaction between these components can result in the formation of compounds

such as $CaO.SiO_2$. However, the electronuetral character of species in the slag was questioned by many investigators since the findings of Aiken[57] who produced iron by electrolysis of liquid $FeO\text{-}SiO_2$. The fact that passing electric current through the oxide melt produces metal implies the existence of charged ions in the liquid. The ionic theory of liquid slags was first proposed by Hersaymenko and established by electrical conductivity measurements on different slags. It is now well accepted that liquid slags consist of ionic species including cations (e.g. Ca^{2+}, Fe^{2+}, etc.) and anions (e.g. SiO_4^{4-}, PO_4^{3-}, etc.). These oxides are present in two main types[7]: basic oxides, which donate O^{2-} ions to the slag, and acidic oxides, which accept O^{2-} ions, e.g. SiO_2, P_2O_5. Acidic oxides such as SiO_4^{4-} termed to be network formers. Silicate containing slags are the most common in metallurgy. Silicate slags are made of Si^{4+} cations, which are surrounded by 4 oxygen anions arranged in the form of tetrahedron. Those tetrahedrons are connected to each other by sharing the common oxygen, bridging oxygen. Cations such as Na^+, Ca^{2+}, Mg^{2+} termed to be network breakers, breaking these bonded oxygens and forming non-bridging oxygens, O^- and free oxygens, O^{2-}. When basic oxide is added to a network forming oxide, the oxygen bridges between groups are broken.[7]

The structure of liquid slag can be described with respect to the effect of metal oxide addition to silica, since most metallurgical slags contain SiO_2. The essential building unit in crystalline and molten silicates is the unbonded tetrahedron. In pure silica, each oxygen (bridging oxygen) connects two neighboring tetrahedra forming a complete network as shown in Figure 2.1[7]. Adding a basic oxide such as calcium oxide to the pure silicate slag, provides free oxygen and a calcium cation. The free oxygen breaks

down the connection between neighboring tetrahedra and the calcium cation provides charge balance for the system. If the ratio of CaO/SiO_2=2, all the connections between tetrahedra are broken down.

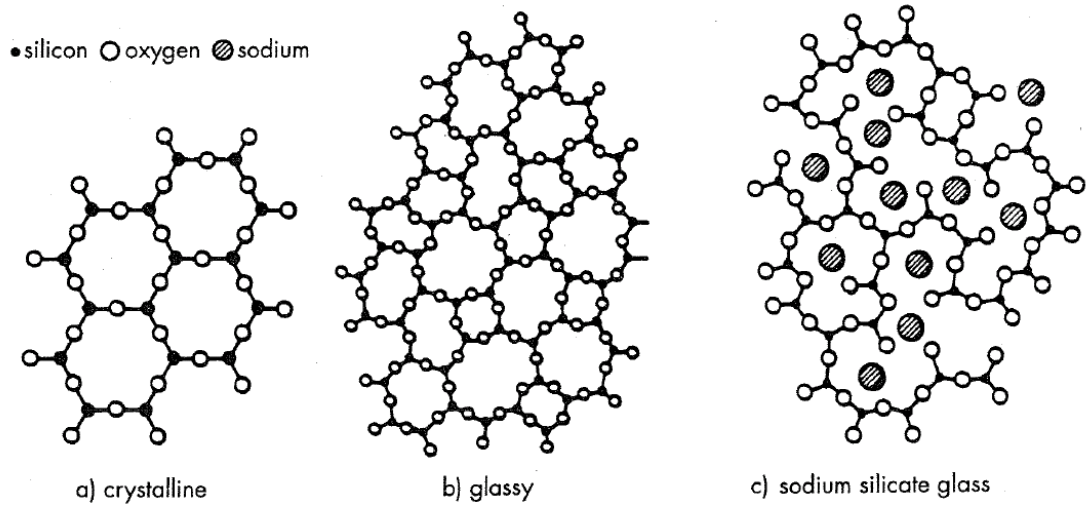

Figure 2.1 Schematic representation in 2-dimensions structure of (a) crystalline silica, (b) glassy silica, (c) sodium silicate glass[7]

The composition of a slag is often described in terms of its basicity ratio, which is the ratio of its basic and acidic components. Wide variation is found in the specific definition of this ratio. The simplest index of the basicity is the V ratio[7]

$$V=wt\%CaO/wt\%SiO_2 \quad (2.1)$$

There are several other indices of basicity have been used, for example[7]:

$$Basicity=(wt\%CaO+wt\%MgO)/wt\%SiO_2 \quad (2.2)$$

$$\text{Basicity} = \text{wt\%CaO}/(\text{wt\%SiO}_2 + \text{wt\%Al}_2\text{O}_3) \quad (2.3)$$

At pre-determined temperature, the composition of slag determines the physical properties of slag, such as slag viscosity and surface tension. Slag viscosity is measured by the ability of one slag layer of molecules to move over an adjacent layer of molecules. SiO_2 containing slag forms complete network based on the tetrahedral structure. The length of this structure determines the ease of molecule movement. So more acidic slag has higher viscosity and more basic slag has lower viscosity. Surface tension forms at the interface due to imbalance of attraction force acting at the surface between gas and liquid phases, which are governed by the chemical composition. Surface active elements such as O^{2-}, S^{2-}, are preferentially adsorbed at the surface, hence, lower the surface tension. Surface tension decreases by increasing temperature, except, there are two systems, which are found positive temperature coefficient. Firstly, slag melts containing high levels of SiO_2. As the temperature increase, the large complex structure gradually dissociate, producing an increasing number of unsatisfied molecular bonds at the surface, with increase in the free surface energy. Secondly, as the temperature increases, the surface active elements are progressively desorbed from the surface, hence, the surface tension of these systems increase. Surface tension can't increase indefinitely with temperature, eventually, it always tends to zero when the system approaches the critical temperature. So in these systems, a maximum surface tension must exist.

2.2 Refractory degradation mechanism:

The degradation of refractory is a complex phenomenon, involving both chemical and mechanical processes, which may act synergistically. As in any chemical reaction between a solid body and a liquid, corrosion of refractories by molten liquids involves chemical reaction as well as reactant and product transport. In this process, the rate of reaction is affected by the refractories' composition, physical texture, and product transport through the phase boundary, as well as the characteristics of the melt and reaction products.[1] The effects of slag composition, slag penetration in refractory, and refractory dissolution on refractory degradation are respectively reviewed in this section.

2.2.1 The Effect of Slag Composition on Refractory Degradation:

The chemical compositions of slag and refractory are the most important factors in refractory dissolution. First of all, in refractory dissolution, the slag basicity affects the refractory solubility in the slag[8-10]. Basic refractories tend to dissolve in acidic slags, and, acidic refractories tend to dissolve in basic slags. Since most refractory used in the metallurgical industry is basic, mainly, MgO based, the refractory is more likely to be attacked by acidic slags. The dissolution of MgO into CaO-SiO_2-FeO slag is a good example of this behavior. The solubility of MgO in CaO-MgO-SiO_2-FeO slag at 1600^{o}C is shown in Figure 2.2[5]. This figure is derived from the CaO-MgO-SiO_2-FeO phase diagram. It shows clearly that MgO solubility decreases with increasing basicity. In general, to limit the refractory dissolution, the refractory and liquid in contact should be

of similar nature. For example, SiO_2 refractories are used in contact with acid slag. MgO and CaO are basic, so they have good corrosion resistance in contact with basic melts.

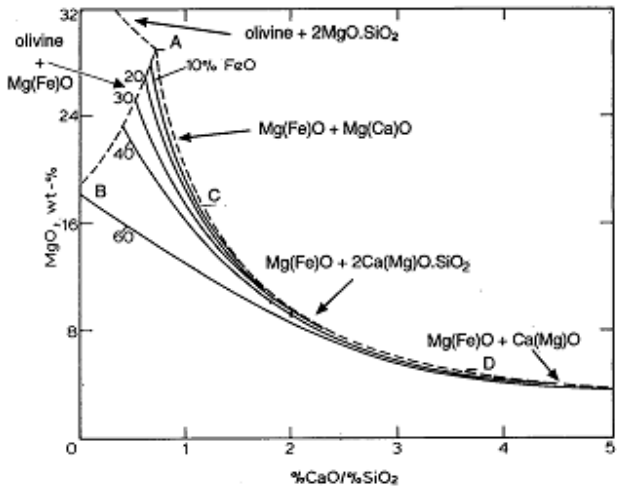

Figure 2.2 Solubility of MgO, as magnesio-wustite, in the system CaO-MgO-SiO_2-FeO at 1600°C as a function of slag basicity and FeO concentration.[5]

The chemical compositions of slag and refractory affect not only the thermodynamics, but also kinetics of refractory dissolution. For example, when the dissolution of refractory in slag is governed by diffusion a reacting species, the dissolution rate can be expressed as follow:[8]

$$J=D(C_s-C_m)/\delta, \qquad (2.4)$$

where D is the diffusion coefficient, C_s is the saturation concentration of refractory in the melt, C_m is the concentration of reactant in the melt, and δ is the effective boundary layer thickness. (D/δ) can be defined as the mass transfer coefficient.

Assume that a thin film forms at the solid/liquid interface in which the flow is laminar. Figure 2.3 shows the curves of hypothetical concentration versus distance and velocity versus distance in the liquid phase. The tangent to the concentration profile intersects the distance axis at δ and is called the thickness of the concentration boundary layer. The tangent to the velocity profile intersects at δ' and is called the velocity boundary layer. Since δ' is greater than δ in weakly agitated melts, the concentration boundary layer determines the mass transfer rate. Both δ' and δ decrease with increasing fluid velocity. When a steady state is reached, δ' and δ become constant. In the present work, unless otherwise stated, the boundary layer thickness refers to concentration boundary layer thickness. [59]

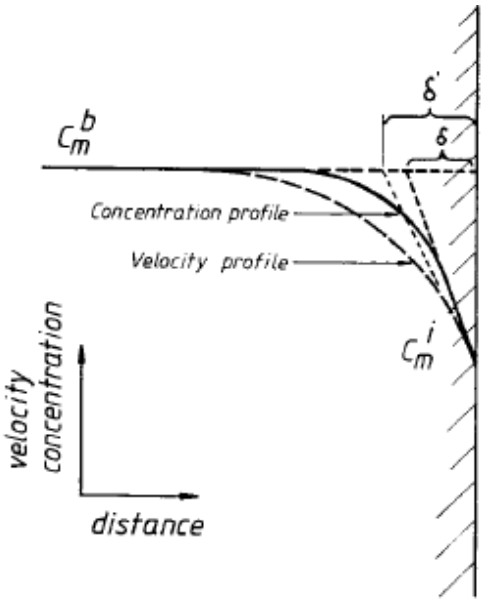

Figure 2.3 Velocity and concentration profiles near a solid-liquid interface [59]

The mass transfer coefficient (D/δ) can be determined by geometry, transport properties of the fluid and flow conditions. When (D/δ) is constant, the dissolution rate is dependent on (C_s-C_m). To minimize the dissolution rate, it is necessary to minimize (C_s-C_m). For example, with increasing MgO content in the slag, the dissolution rate of the MgO refractories will decrease.[8]

When a basic oxide is added to a network forming oxide, the oxygen bridges between groups are broken. So addition of a basic oxide to an acidic oxide will generally decrease the viscosity. The viscosity of the liquid has a significant effect on the diffusion coefficient, hence, affecting the dissolution kinetics of the refractory. [7]

2.2.2 Mechanism of Penetration:

Both slag penetration into the refractory grain boundary and refractory dissolution into slag take place when the refractory degrades. First, the refractory grains and cracks are penetrated by liquid. This is highly dependent on the micro-structure of the refractory. The refractory open pores, grain boundaries, and microcracks, are the main channels for the initial slag penetration. In this case, the penetration rate, dh/dt, of the slag into a capillary can be expressed by Eq.(2.5), which is derived from the equations given by Washburn:[8, 11]

$$V = \frac{dh}{dt} = \frac{r^2 \Delta P}{8 \upsilon h} \qquad (2.5)$$

$$\Delta P = \Delta P_C + \Delta P_S = (\frac{2\sigma\cos\theta}{r} - \rho g h) \quad (2.6)$$

where r is the capillary radius, ΔP is the capillary pressure difference between the two ends, ΔP_c is the capillary pressure, ΔP_s is the hydrostatic pressure caused by the penetrated slag, θ is the contact angle, σ is the surface tension, υ is the dynamic viscosity of the slag, ρ is the density of the penetrated slag, h is the slag penetration depth, and t is time.[8, 11]

The hydrostatic pressure ΔP_s may be neglected in comparison with ΔP_c because $\Delta P_{s<<}\Delta P_c$ in the initial stage of penetration. The relationship between the penetration height and time is obtained by integrating Eq. (2.5) from t=0 to t and h=0 to h:[11]

$$h = K_C t^{1/2}, K_C = (\frac{r\sigma\cos\theta}{2\upsilon})^{1/2} \quad (2.7)$$

Eq.(2.7) indicates that the rate of slag penetration increases with increasing radius of the pores and the surface tension of the slag, and with decreasing slag viscosity.[11]

Eq.(2.7) also indicates that the molten slag viscosity has a significant effect on slag penetration. Furthermore, slag viscosity is also very important in refractory dissolution. If the dissolution of the refractory in the liquid leads to increased viscosity, then the mass transport through the adjacent melt layer will be slower so that the melt layer becomes

progressively saturated. On the other hand, if the viscosity of the melt layer is decreased then diffusion through the melt becomes more rapid, and no saturated layer may form.[8]

At higher temperatures the penetration rate increases with decreasing slag viscosity. As temperature decreases away from the hot face, slag viscosity increases so the slag is too viscous to penetrate further. In this case, slag penetration can be suppressed by increasing slag viscosity. This behavior is represented schematically in Figure 2.4.[8, 9]

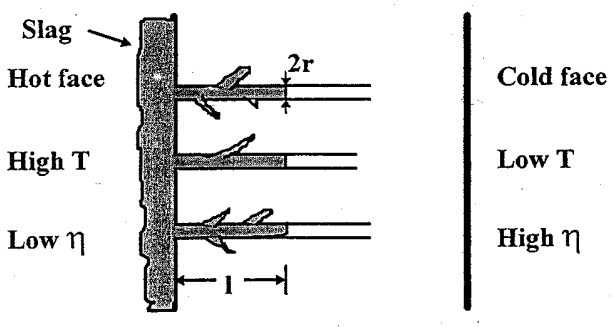

Figure 2.4 Schematic diagram of liquid (slag) penetration in typical kiln lining[8]

2.2.3 Kinetics of Dissolution:

The dissolution of refractories into molten slag can be a direct dissolution process or an indirect dissolution process. Direct dissolution occurs between a solid and a liquid as atoms from the solid dissolve directly into the liquid. As dissolution continues, the reaction products diffuse away from the interface. There is also indirect dissolution process. Indirect dissolution occurs when one or more solid reaction phase form on the solid interface separating the refractory from the liquid. In this case, the dissolution rate is determined by mass transport through the solid reaction phase.[8, 12, 13]

Direct dissolution rates of refractory into slag are governed by the following three mechanisms: (a) the transfer of the reactant species from the melt to the solid/liquid interface (b) chemical reaction (or solution) at the interface, (c) the transport of the product species away from the interface to the bulk of the melt. The rate determining step is the slowest step that controls the overall rate. [12]

If any two or more steps take place at comparable rates, then it is referred to as mixed control. In the case of reaction control, the dissolution process may be directly controlled by a reaction with respect to reactant species, the initial rate can be expressed by:[8]

$$J=K\cdot A\cdot(C_o-C_{eq}), \qquad (2.8)$$

where J is the dissolution rate, K is the rate constant, A is the reaction area, C_o is the concentration of reactant in the bulk, and C_{eq} is the concentration at the interface. Thus, in a reaction control process, surface irregularities such as grooves and porosity, which increase the reaction area in the above equation, have a significant effect. In this case, stirring of the melt has no effect on the dissolution rate.

In a situation where the rate of removal of reaction products by diffusion is slower than the rate of chemical reaction, a solute rich boundary layer builds up, whose interface with the refractory is saturated with reaction products. The dissolution processes are then governed by the diffusion of reactants to, or the products away from, the interface through the boundary layer.

The rate of dissolution can be expressed as follows:[8]

$$J=D(C_o-C_i)/\delta, \quad (2.9)$$

Where D is diffusion coefficient of the reaction product in the bulk liquid, δ is defined as the effective boundary layer thickness. The solubility of the refractory in slag is one of the main effects in mass transfer controlled dissolution process and will be discussed in section 2.3.

The effective boundary layer thickness δ is determined by the flow conditions, such as velocity and viscosity. In the mass transfer process, if there is some forced or natural convection, for example, stirring the melt or rotating the refractory sample, the thickness of the boundary layer δ is reduced. If the forced convection is strong enough, the dissolution can become a reaction controlled process.[8]

For a variety of different cases, the effective boundary layer thickness has been studied. The boundary layer thickness for mass transport from a vertical cylinder to a solution with natural convection caused by density difference driving forces has been derived by Elenbaas [14] as:

$$\delta = 1.96\left(\frac{D_i \upsilon_i x}{g\Delta\rho}\right)^{1/4} \exp\left(-\frac{2\delta}{2R+\frac{1}{2}\delta}\right) \quad (2.10)$$

where υ is the kinematic viscosity, R is the radius of the solution, x is the distance from the leading edge, Δρ is the fractional density difference, which can be expressed as follows:[14]

$$\Delta\rho = \frac{\rho_i - \rho_\infty}{\rho_\infty} \tag{2.11}$$

Levich obtained the following equation for the concentration boundary layer thickness of a solute species dissolving from a rotating disk:

$$\delta = 1.61\left(\frac{D}{\nu}\right)^{1/3}\left(\frac{\nu}{\omega}\right)^{1/2} \tag{2.12}$$

Where, δ (cm) the boundary layer thickness, D (cm^2/s) is the diffusion coefficient, ω (rad/s) is the angular velocity of the disk, and ν (cm^2/s) is the kinematic viscosity. If the boundary layer leads to, the formation of a solid interface, that becomes an "indirect dissolution". Sanghage and Yurek[12, 13, 15] used a rotating disk apparatus to study Al_2O_3 dissolution in a CaO-MgO-Al_2O_3-SiO_2 slag system to study the indirect dissolution. The formation of a spinel ($MgAl_2O_4$) layer was found at the Al_2O_3 sample surface. It was found that the indirect dissolution rate is much lower than the direct dissolution rate. Indirect dissolution reduces the dissolution rate due to the change of the controlling step of the overall reaction. For direct dissolution, diffusion through the liquid boundary layer is the controlling step. For indirect dissolution, diffusion through the solid phase becomes the controlling step. The formation of spinel at solid-liquid interface, thus the indirect dissolution decreases the Al_2O_3 concentration at spinel/melt interface. For direct dissolution, the melt is saturated with Al_2O_3 at Al_2O_3/melt interface. For indirect dissolution the melt is not saturated with Al_2O_3 at spinel/melt interface. The decreasing of Al_2O_3 concentration at the interface decreases the driving force for diffusion, thus decreases the dissolution rate.[12, 13, 15]

In practical situations, dissolution is often under mixed control and it's difficult to distinguish between the reaction and diffusion control. Experiments must be performed over a wide range of conditions to demonstrate the dissolution mechanism convincingly.[8]

2.3 Dissolution of MgO refractory:

MgO is widely used as a refractory in industrial furnaces, because of its high temperature resistance and slag resistance. The dissolution of MgO refractories has been widely studied. [8, 16-21, 61]

The dissolution of MgO refractory is limited by the MgO solubility in slag which is a strong function of the acidity and basicity of the slag as discussed in section 2.2. Zhang and Sarpoolaky [17] investigated the saturation solubility of magnesia in slags and found that slag basicity has a critical influence on the MgO solubility. Fused and sintered magnesia grains were reacted with EAF and BOF slags at 1600^{o}C for 3 hours and at 1700^{o}C for 6 hours. By checking the quaternary MgO-CaO-Al_2O_3-SiO_2 phase diagram, it is found that in the EAF slag (CaO/SiO_2=1.38) the saturated MgO concentration is about 12.1 wt-% at 1600^{o}C, and 17.1 wt-% at 1700^{o}C. In a BOF slag (CaO/SiO_2=3.29), the saturation solubility of MgO is estimated at about 5.0 wt-% at 1600^{o}C and 7.0 wt-% at 1700^{o}C. The content of MgO in EAF slag is much lower than the saturation solubility of MgO at 1600^{o}C and 1700^{o}C, while the BOF slag was almost saturated with MgO at both

temperatures. EAF slags were more able to dissolve MgO since they were far away from saturation.[17]

Bose and McGee[21] used MgO single crystals and various slag compositions to determine the effect of slag composition on the dissolution of MgO. The experiments were conducted at 1600^{o}C by using a high temperature dip technique. It was found that slags were more corrosive with low MgO concentrations than high MgO concentrations even at the same basicity. This is consistent with the solubility discussion given in section 2.3. Additions of TiO_2 or SiO_2 increased the dissolution because the decrease of the slag liquidus temperature, which can affect both the thermodynamics and the kinetics. Thermodynamically, decreasing of the liquidus temperature increases the saturation concentration. Increasing the saturation concentration increases the driving force for dissolution.

The wetting behavior between the refractory and the slag is one of the critical aspects in the refractory dissolution. Some studies showed that oxide additions can affect the contact of MgO with solids or with slags.[8, 22, 19] Using MgO-SiO_2-FeO slag, at 1200^{o}C against single crystal or dense MgO in a sessile-drop technique and high temperature X-ray radiograph, Fukuyama [19] showed that the contact angle between the slag and MgO varied from 10^{o} to 30^{o} and was dependent on the reaction time, the Fe/SiO_2 mass ratio, and the oxygen partial pressure. When Fe/SiO_2=2.05, the contact angle decreased from 30^{o} to 10^{o} by increasing the reaction time. When Fe/SiO_2=1.44,

contact angle was independent of the reaction time. In the system Fe/SiO_2=2.05, two solid phases, magnesiowustite ((Mg,Fe)O) and olivine $(Mg,Fe)_2SiO_4$) were observed at the slag and MgO interface.

There are several theories to explain the mechanism of the dissolution of MgO in slags. Bates[18] used the high temperature dip technique to examine the dissolution of single MgO crystal in a $CaO-Al_2O_3-SiO_2$ (40/20/40 Wt-%) melt at 1400°C. Four different solid reaction products were observed. Adjacent to the MgO surface, there was a two-phase composition of $2CaO{\cdot}MgO{\cdot}2SiO_2$-MgO/$CaO{\cdot}MgO{\cdot}SiO_2$-MgO. Adjacent to this, there was $MgAl_2O_4$ spinel crystals with edges extending into the two phase structure. The spinel on the silicate side was uniform with a layer of MgO rich $2CaO{\cdot}Al_2O_3{\cdot}SiO_2$ between the spinel and the silicate. These results suggest that the dissolution of MgO refractory is controlled by an indirect dissolution process.

Zhang and Seetharaman[20] used a high temperature dip technique at 1573K-1673K to investigate the dissolution of MgO in $CaO-FeO-CaF_2-SiO_2$ slags under static conditions. By using SEM-EDS, the MgO dissolution process was shown to consist of two steps: (a) the formation of a solid-solution $Mg_{1-x}Fe_xO$ and (b) the dissolution of solid solution in the slag. This result is consistent with the work of Fukuyama[19] who showed that at 1200°C olivine $(Mg,Fe)_2SiO_4$ and magnesiowustite (Mg,Fe)O layers formed at the slag/MgO interface when MgO reacted with the FeO and SiO_2 contained slags. Zhang and Seetharaman also found that the solid solution layer thickness increased with the

concentration of CaF_2 below 15 wt-% but decreased at higher CaF_2 levels. The main reason for this is that fluoride can decrease the silicate melt viscosity by breaking of silicate polymers, hence increase the mass transfer rates in the slag.[20]

2.4 Marangoni Effect

James Thomson recognized in 1855 that an interface between two fluid phases could move spontaneously under the influence of interfacial tension gradients.[2] Thomson introduced drops of alcoholic liquors into the surface of water and found strong radial surface movements away from the points of introduction. He also observed surface movements in water absorbing alcohol from the vapor phase. Similar phenomena were later investigated by Marangoni and this type of flow became known as ” Marangoni convection”. Since Thomson's experiments, spontaneous interfacial convection has been found to exist in a myriad of other systems involving aqueous and organic phases.[2] Marangoni convection plays a significant role in high temperature processes such as melting, smelting, casting, and welding.[4, 62] In this section, there will be two sub-sections: the general Marangoni effect will be discussed first, and subsequently, the importance of Marangoni in the metallurgy field will be examined.

2.4.1 General Marangoni Effect:

The driving force for spontaneous interfacial motion is the difference in interfacial tension. The interfacial tension gradients arise as a result of local changes along an

interface due to variations in: (1) the concentration of a surface-active solute C, (2) the electrical potential Ψ or (3) the temperature T. These gradients lead to a shear stress, which can be expressed by:[23]

$$\tau = \frac{d\sigma}{dx} = \frac{\partial\sigma}{\partial T} \bullet \frac{dT}{dx} + \frac{\partial\sigma}{\partial c} \bullet \frac{dc}{dx} + \frac{\partial\sigma}{\partial e} \bullet \frac{de}{dx} \qquad (2.13)$$

where σ is surface tension, T is temperature, C is concentration, *e* is electrochemical potential.

Marangoni flow can be characterized by the dimensionless Marangoni number that represents the ratio between the interfacial force and the viscous force:[24]

$$Ma = (\frac{d\sigma}{dx}) \frac{L^2}{\mu D} \qquad (2.14)$$

where L is the mass transfer film thickness(m), (dσ/dx) is the interfacial tension gradient across the liquid film(N/m^2), D is the diffusivity of transferring solute in the liquid(m^2/s) and μ is the viscosity of the liquid(Ns/m^2).

A surface-active solute can lower interfacial tension between the liquid-metal and gas. The relationship between the interfacial tension, σ, and the solute concentration, C, can be described by the Gibbs adsorption isotherm equation (2.15): [3]

$(\partial\sigma/\partial C) = -\Gamma s\ (RT/C)$. (2.15)

Where R is Boltzmann constant and T is temperature. Equation(2.16) indicates that the excess of the solute at the interface relative to the bulk, Γs, can be seen to be positive for $(\partial\sigma/\partial Cs)<0$. The solutes dissolved in liquid metals are positively adsorbed, as for the Fe-O, and Cu-O systems. Changes in the electrical potential at the interface can also alter the interfacial tension, which cause display electrocapillary flows. Concentration gradients and potential gradients are capable of providing a large driving force for interfacial motion.[3]

Interfacial flow occurs in reactions in which inequalities of surface tension arise spontaneously over the interface across which reaction occurs. The classic example for this phenomenon is the vaporization of ether from water. This was described by Langmuir and is represented in Figure 2.5. Eddies of liquid bring ether to the surface at A' where it is adsorbed and lowers the surface tension. Eddies of gas B remove the ether at random and raise the surface tension locally so that horizontal interfacial movements occur, and eddy flow into the A' region is enhanced.[1]

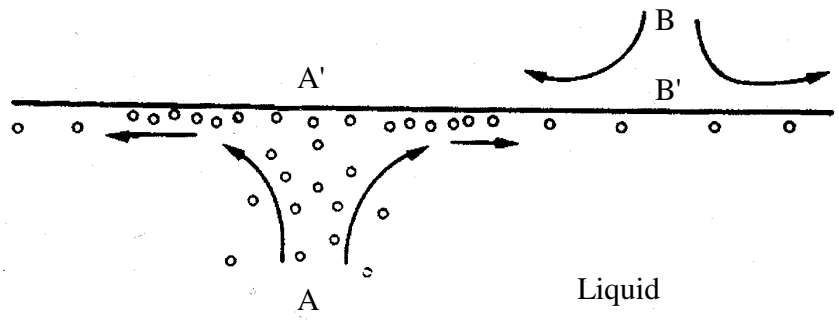

Figure 2.5 An eddy of liquid A, brings a small volume of undepleted solution of surface active agent to the surface, whilst an eddy of gas B, depletes the surface of the active solute. Thus the surface A' spreads to B' and carries some underlying liquid with it.[1]

Liquid metals and slags generally have high surface or interfacial tensions. When surface active components such as oxygen and sulfur are present in liquid metals, they can create Marangoni flows. [23]

Vigorous interfacial movements have been observed when oxygen gas is jetted onto the surface of liquid tin, copper and iron. Figure 2.6 shows the situation with liquid tin at 1100^{o}C, as photographed by Brimacombe and Weinberg.[3] A small jet of oxygen is being directed at the center of the top surface of the liquid tin in a small crucible. Directly beneath the jet, tin oxide is produced and looks bright because of its high emissivity. Because the oxide wets the metal and has a much lower surface tension than the unoxideised tin, which is at a distance from the jet, it has a high spreading coefficient. Thus the oxide is drawn out radically towards the sides of the crucible in streaks,

dissolving rapidly as it moves. In addition the metal near the oxide, which must be high in oxygen, probably has a much lower surface tension than the metal near the walls, so that a radial flow of metal is induced towards the side of the crucible from the center. The net result is radial movement of oxide and metal with velocities up to 150cm s^{-1} in a 4.5 cm diameter crucible. It has been shown that these movements are not caused by the momentum of the gas emerging from the jet.[3]

Subsequently, Barton and Brimacombe showed in experiments with copper, that such phenomena increased the transfer rates of oxygen into the copper some forty times over the rates which would be obtained in an otherwise weakly stirred metal.[3]

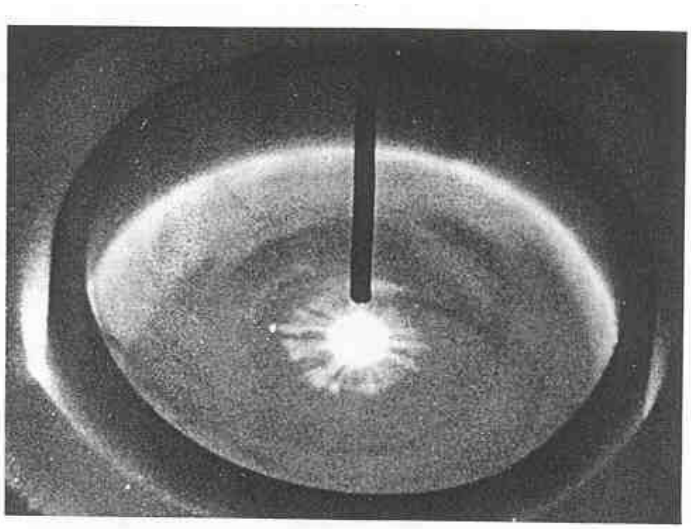

Figure 2.6 Surface driven flow of tin oxide over the surface of liquid tin. The bright oxide is produced by the oxygen jetted at the center of the tin surface and is drawn out radially by surface tension forces at the same time as it dissolves. Velocities are of the order of 100cms^{-1}[3]

Spreading of the metal surface in the presence of metal oxide will only result if the surface tension of the metal is greater than the sum of the metal oxide surface tension and the interfacial tension of the metal-metal oxide interface. This can be expressed in terms of the initial spreading coefficient, S, defined as:[3]

$$S=\sigma_M-(\sigma_{MO}+\sigma_{M/MO}), \quad (2.16)$$

which must be positive for spreading, where σ_M is the surface tension of metal, σ_{MO} is the surface tension of metal oxide, $\sigma_{M/MO}$ is the interfacial tension of the metal-metal oxide interface. The spreading velocity of an interface is linearly dependent on the ratio, S/μ, where μ is the liquid viscosity.[3]

Brimacombe also investigated the Marangoni effect in electrochemical system. Figure 2.7 shows photographs of turbulence set up by the reaction:

$$[In]_{Hg}+3(Fe^{3+})=(In^{3+})+3(Fe^{2+}) \quad (2.17)$$

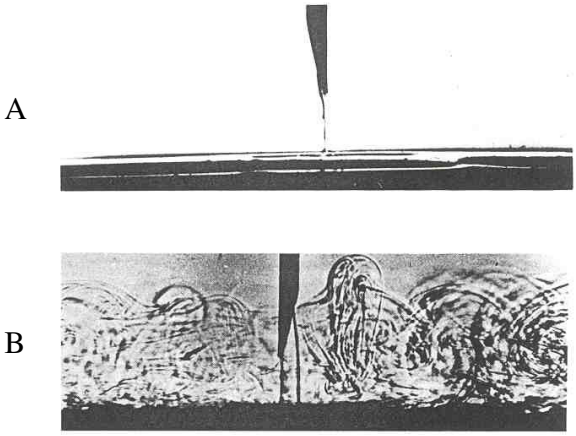

Figure 2.7 Photographs showing interfacial turbulence set up during transfer of indium from a mercury amalgam to an eddy of concentrated ferric nitrate solution which is introduced to the surface through a hypodermic needle: (A) concentrated solution falling to the surface, (B) turbulence set up a moment later. The field is about 2cm wide.[3]

This reaction occurs between an indium amalgam (dark) and aqueous phase (light) containing dilute ferric nitrate. Concentrated ferric nitrate is being added from a hydrodynamic needle to simulate the arrival of an eddy rich in ferric nitrate at the interface. Figure 2.7 (a) shows the arrival of the concentrated solution; Figure 2.7 (b) the turbulence setup a moment later. Typical maximum distances moved in the surface are about 2cm for each eddy and velocities of sideways movement may be up to 30cms^{-1}. The effect of this turbulence is very important, because it occurs in the interfacial region where reaction takes place. In this case it increases mass transfer rates up to three times in well-stirred systems and more in less well-stirred systems.[3]

2.4.2 Marangoni Effect in Metallurgy

There have been a wide range of studies about the Marangoni effect in metallurgy, specially in as the formation of emulsions, welding and slag foaming.[22, 25-30, 62]

It has been proposed that the formation of emulsions in the steelmaking process involves Marangoni convection.[27, 30] The formation of emulsions was observed in the process of desulfurization and dephosphorisation of liquid steel. Kozakevitch[29] followed the desulfurization of liquid steel by molten slag and observed the remarkable change in the shape of the sessile drop of the steel in the liquid slag. Riboud and Lucas simultaneously measured the mass transfer of Al from the metal to the slag and the slag/metal interfacial tension.[27] A massive drop in the apparent slag/metal interfacial tension was associated with a high mass transfer rate. The apparent slag/metal interfacial tension increased when the mass transfer rate slowed, coming back to the initial value. The dramatic change in the apparent slag/metal interface tension associated with rapid mass transfer is usually referred to as dynamic interfacial tension. When the slag/metal interfacial tension is very low, any disturbance or turbulence can cause droplets of one phase to move into the other phase. This is usually referred to as emulsification and the formation of a metal emulsion in the slag phase leads to very fast kinetics for the refining reactions because of the huge surface area/mass ratio. Chung and Cramb[24] suggested that interfacial chemical reactions induce Marangoni flow and natural convection at the slag/metal interface. This

interfacial flow can give rise to interfacial waves which, due to the Kelvin-Helmholtz instability, become unstable, and lead to spontaneous emulsification of slag in the steel and steel in the slag. Thus from a refining process viewpoint a low interfacial tension is very advantageous and modern metal production processes make use of this. However, refining also requires separation of the slag and metal, which is not favored by a low interfacial tension.[60]

A second example in metallurgy involving the Marangoni effect is in welding. The problem of variable weld penetration in autogenous tungsten insert gas (TIG) welding of stainless and ferritic steels has been studied.[25, 31] There have been several theories suggesting that small differences in minor element concentrations in the steel result in changes in the surface properties of the weld pool by affecting either the interfacial energies or the fluid flow motion in the weld pool. Small differences in the concentrations of the surface-active elements such as sulphur and oxygen, cause substantial changes in the surface tension of iron and other elements.[25] Heiple and Roper[31] suggested that variable weld penetrations are due to differences in fluid flow in the weld pool arising from differences in both the direction and magnitude of thermocapillary forces. These forces are controlled by the concentration of surface-active elements; such as sulphur and oxygen in the metal. They also pointed out that when the sulphur or oxygen concentration exceeded a certain critical value (around 50 ppm), the temperature coefficient of surface tension ($d\gamma/dt$) changed from a negative to a positive value. They suggested that since a large temperature gradient exists between the center

and the edge of the weld pool (of order of 500k/mm), a large surface tension gradient will be produced across the surface. The resulting Marangoni flow will occur from a region of low surface tension to a region of high surface tension. These surface flows subsequently trigger circulation flows in the molten weld pool. For most pure metals, as well as iron and steel with low O and S contents, the surface tension decreases with increasing temperature, which results in a negative surface tension temperature coefficient, Figure 2.8(a). In this case, the surface tension will be greater in the cooler regions at the edge of the weld pool and which induces a radially outward surface flow. This flow carries hot metal to the edge of the pool. The consequent recirculation of the melt back to the centre results in a wide shallow weld. In contrast to this, in Fe-based melts with S or O concentration greater than 60 ppm, ($d\gamma/dt$) will be positive as shown in Figure 2.8(b) and thus the surface tension is greatest in the high temperature region at the center of the pool, which induces a radially inward flow. This flow produces a downward flow in the center of the weld pool, which transfers hot metal to the bottom of the pool the where melt recirculates back the sides resulting in a deep and narrow pool. Keene has pointed out that systems which exhibit a positive (($d\gamma/dt$) must go through a maximum at some temperature and thus produce a complex flow similar to that shown in Figure 2.8(c).

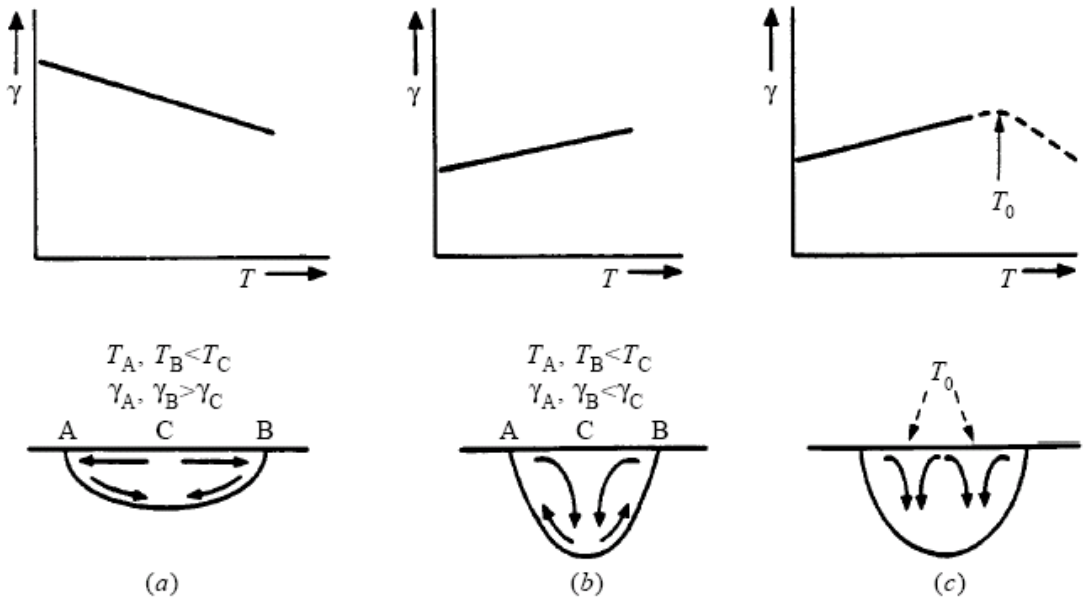

Figure 2.8 Schematic diagram illustrating the Heiple-Roper theory for variable weld penetration [31]

2.5 Previous Experimental studies:

Several previous experimental studies have been reported in the literature[23, 32-37].

Mukai [32, 33, 35, 38] has made several investigations of the Marangoni effect in refractory slag-line corrosion and proposed mechanisms of slag-line corrosion in the case of slag surface tension increasing with dissolved refractory, and in the case of slag surface tension decreasing with dissolved refractory.

In the solid silica SiO_2(s)-(PbO-SiO_2) slag system, the slag surface tension is increased due to the dissolved SiO_2. The flow patterns were principally composed of wide zones of rising film and narrow zones of falling film, according to the contour of the specimen, as shown in Figure 2.9. In the case of a cylindrical specimen, the position of the falling zone moves gradually on the surface of the specimen. However, the prism specimen always has one zone of rising film at, and around, each corner of the specimen and one narrow zone of falling film at each plane side of the specimen, as shown in Figure 2.10.[32, 33]

Mukai[32, 33] proposed that since the contact time of the upper film with the specimen is longer than that for the lower film, the upper film has a higher SiO_2 content, due to the dissolution of SiO_2 from the specimen into the film. The difference in SiO_2 content causes a surface tension gradient in the vertical direction. Since the surface tension of a PbO-SiO_2 slag increases with increasing SiO_2 content, the slag film is continuously pulled up by the surface tension gradient. When the weight of the risen slag exceeds the surface tension gradient, the falling film is formed. The degradation rate is controlled by mass transport of the dissolved component, SiO_2, in the slag film assisted by the Marangoni flow of the film. So the local degradation proceeds largely as a result of the wall-washing of solid silica with a fresh thin, rising slag film induced by the Marangoni effect. [32, 33]

In the solid silica SiO_2(s)-(FeO-SiO_2) slag system, SiO_2 reduces the surface tension of the slag. The local degradation zone of this system forms a steep groove and the vertical

width of the local degradation zone is narrower than that of the SiO_2(s)-(PbO-SiO_2) slag system. In this system, the SiO_2 content in the upper part of the slag film surface is higher than in the lower part of the surface, SiO_2 content also decreases with distance from the specimen. Thus, by reducing the SiO_2 concentration in the slag, the surface tension far away from the specimen is higher than the surface tension near the specimen, the slag film is pulled away by the surface tension gradient from the specimen as shown in Figure 2.10 [33].

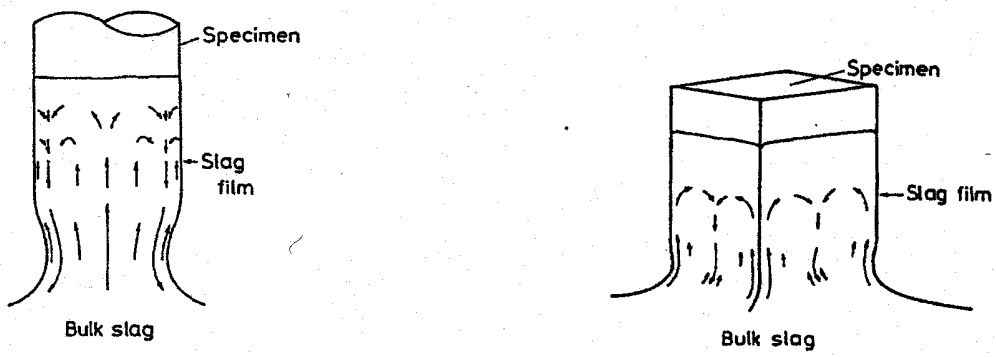

Figure 2.9 Typical flow pattern of slag film on a cylindrical and a prism silica specimens immersed in PbO-SiO_2 slag .[33]

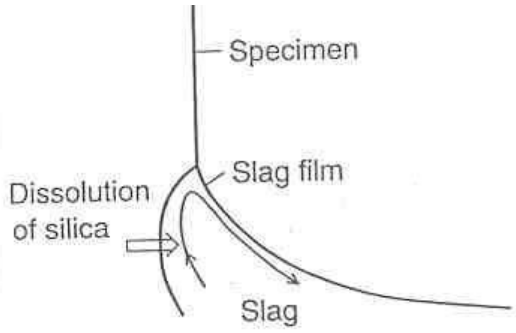

Figure 2.10 Marangoni flow in FeO-SiO_2 slag film on silica specimen due to concentration gradient of SiO_2 dissolved from the specimen[33]

Nightingale and Brooks conducted stirring studies of dissolution of MgO refractory in CaO-SiO_2 slag under forced convection. They showed that the rate of dissolution was controlled by mass transfer at speeds up to about 600 rpm, beyond which chemical reaction rate appeared to become dominant.[55]

Fagerlund and Sun[23, 36] carried out studies comparing the refractory corrosion rate caused by Marangoni flow and forced convection. A high temperature dip technique was used where, cylindrical SiO_2 samples were partially immersed into slag with various SiO_2 contents, from 15wt% to 30wt%, at 1300^{o}C for 2 hours. These results were compared with results from experiments at the same conditions but using the rotating SiO_2 samples. The critical rotation speed was defined as the speed at which the visible necking effect, caused by Marangoni flow, seemed to disappear. The critical rotation speed (V_{cr}) was found for different SiO_2 contents in the slag. It was found that by increasing the SiO_2

content in the slag from 15wt% to 30wt%, the critical rotation speed increased from 8.8cm/s to 16.2cm/s. However, when the SiO_2 concentration in the bulk increased, the concentration difference between the bulk of the slag and the slag near the interface decreased. Because the concentration gradient between the bulk of the slag and the slag near the interface is the driving force for Marangoni flow, a lower concentration gradient should cause a lower driving force for Marangoni flow, and hence a lower V_{cr} would be expected. This theory is inconsistent with the experimental observations reported in [23]. The interpretation of this phenomenon is the effect of viscosity. Reynolds number $\mathrm{Re} = \frac{uD}{\mu}$ and Marangoni number $Ma = \frac{\Delta\sigma\delta}{\mu D}$. Where, u is the velocity, D is the diameter of the SiO_2 rod, μ is the dynamic viscosity, $\Delta\sigma$ is the surface tension gradient, and δ is the boundary layer thickness. As the viscosity increases with increasing of SiO_2 and surface tension gradient decreases, both of Re and Ma decrease. As the results of those two effects, the critical velocity increases as the SiO_2 content increases[36].

Mukai[35] studied the corrosion of MgO-Al_2O_3 crucible refractory at the slag-metal interface. An up-and-down motion is observed at slag-metal interface on X-ray photographs. Figure 2.11 schematically shows this phenomenon. With the dissolution of the refractory, the local concentration of metal cations and oxygen anions increases in the adjacent slag. Hence, oxygen anions transport to slag metal interface and thus, increasing the oxygen concentration in the adjacent molten metal. This results in a decreasing of the slag-metal interfacial tension. So, the interfacial tension is lower near the refractory

sample due to a higher oxygen concentration. Thus, Marangoni flow forms from the low interfacial tension to high interfacial tension, the molten metal is be pulled away from the refractory by the flow and the slag fills into the gap.

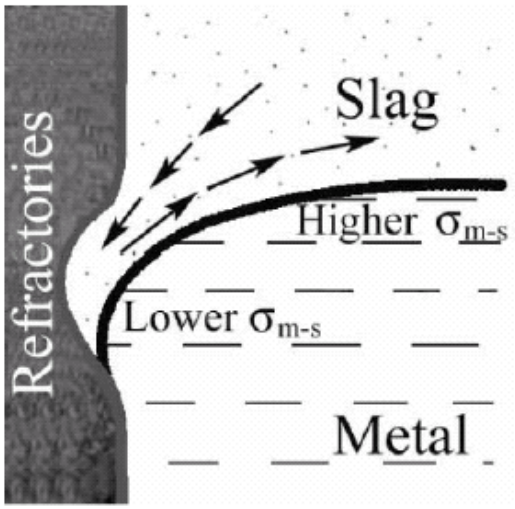

Figure 2.11 Schematic diagram of motion of the slag-metal interface.[35]

Mukai[34] also performed an analysis of the process by which local corrosion of an immersion MgO-C nozzle occurs at the interface between liquid metal and slag. As shown in Figure 2.12, when the wall of nozzle material is initially covered with a slag film, the film not only wets the oxides but dissolves them in preference to graphite. This changes the interface to a graphite-rich layer. Since the metal phase wets graphite better than the slag, the metal phase creeps up the surface of the specimen as indicated in Figure 2.12(b) and dissolves graphite in preference to the oxide. Once the graphite-rich layer disappears due to dissolution into metal, the slag can again penetrate the boundary

between the metal and the specimen, and the process is repeated. This cycle produces a local corrosion zone at the metal-slag interface.

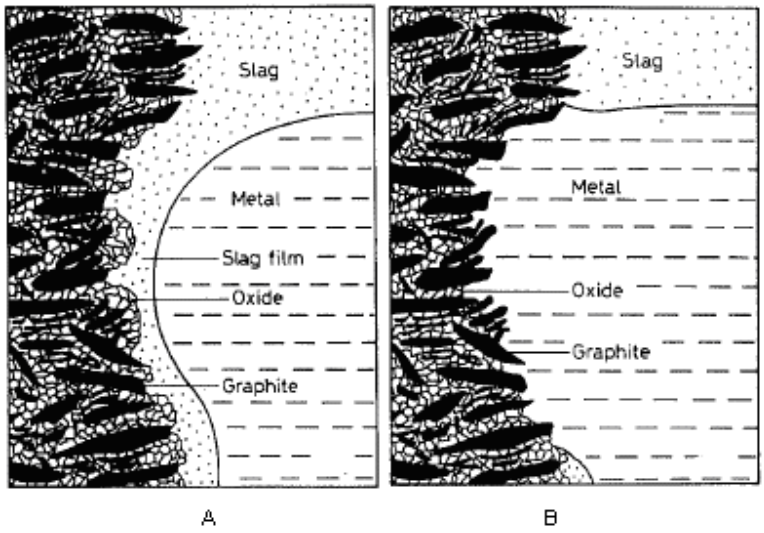

Figure 2.12 Schematic representation of the manner in which local corrosion of immersion nozzle proceeds.[34]

2.6 Mathematical Models:

Some mathematical studies have been performed and models developed to quantify the corrosion of refractory due to the Marangoni effect[40-46]. The following discussion will examine existing models.

2.6.1 Hrma Model[40]

Hrma[40] studied the dissolution rate governed by free surface convection caused by a surface tension gradient, as presented schematically in Figure 2.13. The dissolution

occurs at the liquid and solid interface. The formulations are based on the following assumptions:

1. The dissolved solid remains saturated at the interface and the interfacial tension gradient is continuously kept at a high level.

2. The density-driven free convection is not too intensive compared to the surface tension flow, the surface free convection is predominant

3. The dissolution process is diffusion controlled, not reaction controlled; hence, at the boundary, the solution is saturated.

4. The solid-liquid and liquid-gas interface in the meniscus are nearly parallel.

5. The liquid in this meniscus thus forms only a thin layer and the dissolution of the solid in the meniscus area is essentially into a thin liquid layer.

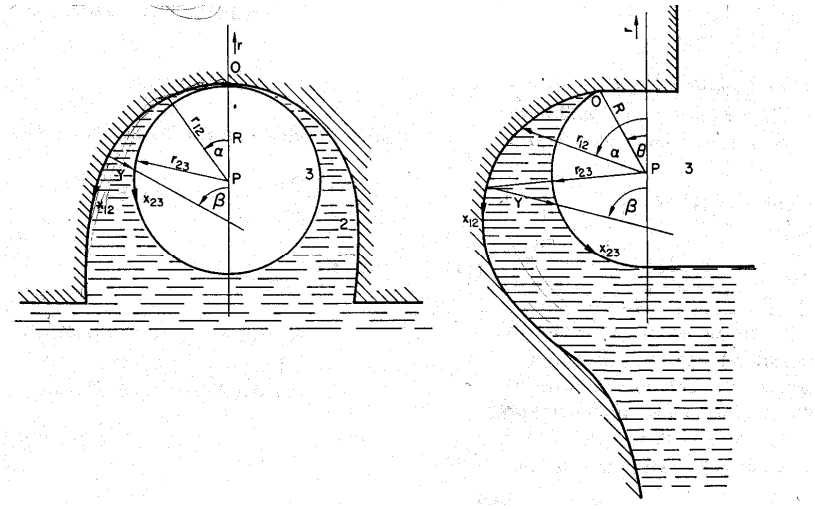

Figure 2.13 The cross section of the corrosion cavity and groove for flux-line and upward drilling, 1. solid, 2. liquid, 3. gaseous phase[40]

A semi-empirical mathematical model was developed based on the material balance: since the dissolved solid remains saturated at the solid-liquid interface, so the materials dissolved into the interface should be equal to the materials transfer from the interface, the mass balance of solute at steady state can be expressed as follows:

$$\frac{d}{dx_{12}}\int_0^Y Cv_x dy + D_o(\frac{\partial C}{\partial y})_{y=0} = 0 \qquad (2.18)$$

where x_{12} is the distance measured along the solid-liquid interface, v_x is the velocity component directed along x_{12}. D_o is the diffusion coefficient of the solute in solvent for the concentration at the interface, C is the concentration and y is the distance from interface measured in the direction of the normal, Y is the thickness of the liquid layer in the meniscus.

The relationship between the rate of dissolution u_s and the mass flux density at the interface $j_{o,}$

$$j_o = -\rho_1 D_o (\frac{\partial C}{\partial y})_{y=0}, \tag{2.19}$$

is given by :

$$u_s \sin\beta = -D_o (\frac{\partial C}{\partial y})_{y=0} \tag{2.20}$$

where ρ_1 is the density of dissolving solid.

Eliminating the meniscus thickness Y and reorganizing Equation 1 and 2, the dissolution rate u_s was given as:

$$u_s = B\Delta C(\frac{D_o^2 \Delta\sigma^* g}{\nu})^{1/3} \tag{2.21}$$

Where B is a constant, ΔC is the difference between concentration at the solid-liquid interface and concentration of the bulk, $\Delta\sigma^* = \Delta\sigma/\sigma$ ($\Delta\sigma$ is the surface tension difference between solid-liquid interface and the bulk, σ is the surface tension of bulk), and ν is kinematic viscosity.

The parameter B in this equation is a function of the velocity and concentration distributions in the meniscus and also the geometrical shape of both interfaces building up the meniscus. Hrma used two methods to calculate the constant B: a theoretical method and an experimental method. The theoretical method calculates B by using various velocities, concentration distributions and corrosion profiles. B can be calculated between to be 0.2~0.4[40].

Hrma used the following systems to validate the model: sodium nitrite-methanol and α-naphthol-octanol. The rate of dissolution governed by surface free convection has been measured at the flux-line at 20^{o}C. The time dependence of the change in diameter at the flux line is shown in Figure 2.14. The rates of dissolution u_s were found from the slopes of the linear parts of the curves. So the material constants and the rates of dissolution were available and the values of B could be calculated from Eq.(2.21). Using this experimental method, Hrma suggested B should in the range 0.3~0.4[40].

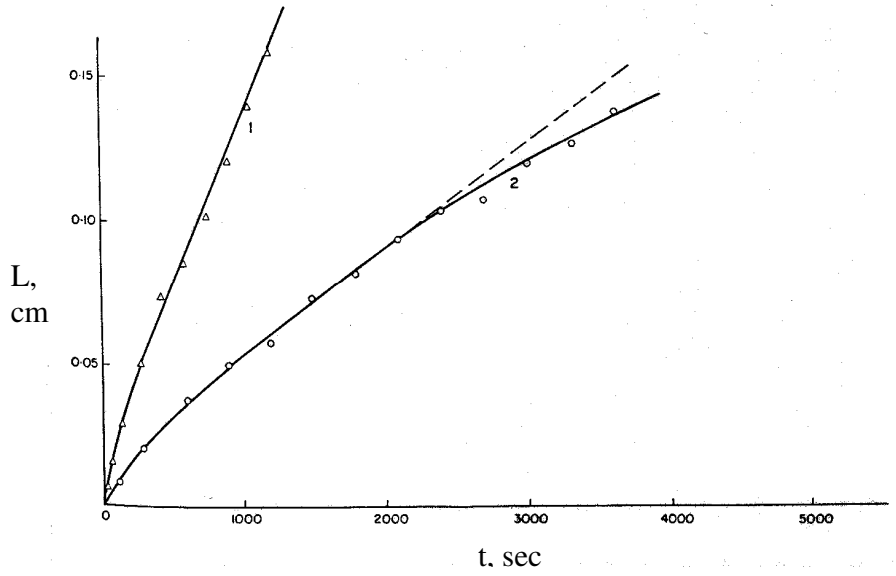

Figure 2.14 Time dependence of dissolution of (1) α-naphthol-octanol and (2) sodium nitrite in methanol; the linear loss was measured at the flux-line[40]

The Hrma model considered the effects of surface tension gradients, contact angle and wetting behavior in slag line corrosion. However, there are some significant weaknesses in this model. First, the model assumed a rectangular geometry. In experimental conditions, the geometry is not rectangular. The variation from the rectangular geometry should be included to develop a more accurate model. Secondly, this model uses a constant B, but an accurate B value is difficult to obtain. Thirdly, it is assumed that surface tension has a linear relationship with concentration, but the relationship between surface tension and concentration is complex and not always linear. Accurate surface tension data for slag is difficult to obtain, which will affect the accuracy of the model.

2.6.2 Numerical Models

J. Szekely and V. Stanek[43, 47] analyzed the dissolution of solids in contact with a liquid in simple geometry, and performed mathematical analysis of this process. The problem was formulated by considering the appropriate equation of motion and the diffusion equation. It was found that in the presence of a surface tension gradient between the interface and bulk, the dissolution rate was accelerated, particularly at low values of Reynolds number.

M. Dunkl and R. Bruckner [44, 48] numerically analyzed corrosion of refractory materials in a glass melt under three types of convection flow (concentration, density, surface tension) and discussed a comparison between theory and experiment. This paper was an extension of previous mathematical models and made some improvements based on calculation of effective diffusion coefficient in a refractory-glass system.

Tsotridis[41] developed a numerical model focused on predicting the dissolution of a partially immersed vertical crucible wall into a molten substance. The physical situation is presented in Figure 2.15. Three convection flows were considered in this paper: convection flow caused by a density gradient arising from a temperature gradient, convection flow caused by density gradient arising from a concentration gradient and convection flow due to surface tension gradient. The model was developed on the following assumptions:

1. Heat lost by conduction through the walls of the crucible results in a temperature gradient in which the melt adjacent to the crucible wall was cooler, and therefore denser, than in the center. This temperature gradient induces a density gradient, which drives convection currents downwards at the vertical crucible walls.

2. The crucible material is slightly soluble in the melt. Dissolution of the crucible wall in the melt is a diffusion controlled process. Thus the depth and shape of the corrosion dependes on a number of parameters: (1) diffusion coefficient; (2) the saturation concentration of the dissolved material in the melt; and (3) the flow pattern of the molten material, especially the velocity near the wall.

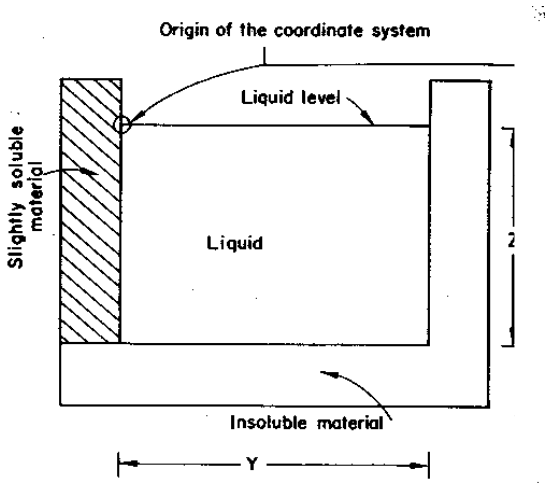

Figure 2.15 Schematic representation of the physical domain considered in [41].

The problem was formulated by considering the Navier-Stokes equations coupled with the energy and diffusion equations. The velocity field was determined by the equations of motion and energy, where the concentration distribution was determined by the convective diffusion equation, the Marangoni number and surface tension were imposed at the boundary conditions. A two-dimensional transient flow numerical algorithm was developed which simultaneously solves the equations of motion and diffusion.[41]

The shapes of the corrosion profiles were studied for different concentration distributions and flow patterns.

Although the Tsotridis model can give predictions of the solid dissolution process, there are some weaknesses in this model. These weaknesses limit the application and accuracy of the model. First, the wetting behavior between liquid and solid is not considered in this model. For a dissolution process, the wetting behavior between liquid and solid is very important. A “wetting” system will have more corrosion than a non-wetting system and this is a crucial aspect in the corrosion process. Secondly, the model assumes that the change in the geometry during the corrosion process does not affect the flow pattern. However, the geometry change is expected to affect the flow patterns, especially near the wall and the melt surface. Thirdly, the model assumed a flat free surface. Actually, the free surface is not flat but is expected to deform due to the Marangoni flow.

2.6.3 Potschke Model

Potschke[45, 46] developed a simple model to describe the rate of refractory corrosion at a slag surface[46] and slag-metal interface[45]. Both of his models are based on mass transfer. In this model, the height of the corrosion capillary was calculated by the Laplace equation:

$$y = \sqrt{\frac{4\sigma_0}{\rho_0 g}} \sin[0.5(\psi - \theta)] \tag{2.22}$$

where σ_0 is the surface tension of the initial melt, ρ_0 is its density, θ is the wetting angle, and ψ is the angle of an inclined plane wetted by the melt. When $y = h_{\max}$ the corrosion groove reaches its maximum height. The fully-developed corrosion groove was assumed to be a half circle. The velocity of Marangoni convection inside the groove was given as:

$$u = \frac{1}{4}\frac{\partial \sigma}{\partial C}\frac{gradC}{\eta_s}d \tag{2.23}$$

where d is the thickness of the liquid layer which covers the corrosion groove, and it is defined as:

$$d = \frac{\sigma_0 \cos\theta}{\rho_0 g S_{\max}}\left[\frac{S_{\max} - S_i}{S_{\max}}\right] \tag{2.24}$$

$S_{\max}$ is the maximum corrosion distance in the horizontal direction.

$gradC$ is concentration gradient, $\frac{\partial \sigma}{\partial C}$ is surface tension gradient due to concentration of the dissolved material. The subscript 0 indicates the initial, and s indicates the saturation condition. The effective mass transfer coefficient can be calculated as:

$$\beta = \sqrt{\frac{4Du}{\pi S_{\max}}} \tag{2.25}$$

where D is the effective diffusion coefficient of the refractory material.

The total corrosion rate at steady-state can be obtained as the mass transfer coefficient multiply by the driving concentration difference.

$$V_{corr} = 360 \frac{\rho_s}{\rho_R} \beta (C_s - C_0) \tag{2.26}$$

ρ_R is the density of the refractory material.

This model is relatively simple and easy to apply. The comparison between the experimental data measured by Dunkl and the calculation results shows the model fits the experimental data relatively well. The simplicity of this model also results in limitation. The corrosion rate is calculated from the saturated concentration at the interface, and the initial concentration in the bulk melt, which didn't consider the increasing of bulk concentration. Also, the detailed information about the dissolution procedure, such as flow condition, can not obtained by this model.

2.7 Numerical Methods to Solve Moving Boundary

The refractory slag-line corrosion problem is a moving boundary problem. Algorithms for moving boundary problems for the Navier-Stokes equations have been reviewed by Floryan and Rasmussen[49]. These algorithms are based on Eulerian, Lagrangian, and mixed formulations. The method used in this study is based on applying mapping technique to describe the moving interface. Analytical mapping fuctions are used to transfers the irregular physical domain into a regular computational domain. The mapping functions are unknown and had to be determined as part of the solution procedure. This technique is computationally efficient and accurate,[50]

In this section, numerical techniques for solving moving boundary problems will be reviewed. These techniques can be classified into two main categories: (a) surface tracking or predominantly Lagrangian methods, (b) volume tracking or Eulerian methods. In the Lagrangian methods, the grid is configured to conform to the shape of the interface, and thus it adapts continually to it. The Eulerian methods usually employ a fixed grid formulation, and the interface between the two phases is not explicitly tracked but is reconstructed from the properties of appropriate field variables, such fluid fractions. Under these broad categories of Lagrangian and Eulerian methods, the following numerical techniques have been developed thus far by researchers in the area of moving boundary problems.

2.7.1 Transformation Methods with Body-Fitted Coordinates

In these methods[50] the irregular physical boundary is mapped by body-fitted, but structured, meshes on which the field equations are solved and moving boundaries tracked. The difficulties in the mapping methods are the multiple-valued interface. It is still possible to generate boundary conforming grids beyond this stage by solving partial differential equations in each phase, with the added expense of solving these questions. Several techniques have been developed to track the moving boundaries, including the Lagrangian-Eulerian formulation, deformed-cell method, and marker and cell method.

Boundary-fitted grids often experience difficulties in the form of grid skewness under severe interface convolution and need to be reconfigured under topological changes of the interface. Such events need to be identified and dealt with a process that will involve considerable logical and algorithmic complexity. Furthermore, the grid points and values of the field variables have to be redistributed in the vicinity of the interface, which may lead to additional numerical dissipation.[50]

2.7.2 Boundary Element Methods (BEM)

Due to the facility offered by the BEM in terms of the reduction of the dimensions of the problem, it has been extensively employed in front tracking. Dendritic structures and Saffman-Taylor fingers have been simulated with considerable success. The BEM is well suited for problems with linear field equations. But its application to nonlinear problems with convection and for physical situations involving time-dependent boundary conditions and topological changes is still under intensive development.[50]

2.7.3 Volume Tracking Methods

Volume-tracking methods[50] differ fundamentally from surface-tracking methods discussed above in that the interface is not explicitly defined or tracked but is reconstructed at every step. The Volume-of-Fluid (VOF) method makes use of a fluid fraction variable f, assigned values of 1 and 0 in the two phases, which is calculated as field variable over the domain. The interfacial cells are then identified as those with fractional values of f. The volume fraction is then advected with the local flow velocity. Over the years, more accurate schemes for advecting the volume fractions have been developed extensively for dealing with passive liquid-gas interfaces. Two classes of algorithms have been employed, namely, piecewise constant and piecewise linear, yielding different degree of accuracy, to recover the interface shape. There also has been effort of combining the VOF method with the finite-element method to simulate solididication and filling processes. [50]

The most striking disadvantage of VOF schemes is that while mergers and breakups of the interface can be handled, they can not be treated with precision. The main difficulty arises in the reconstruction of the interface which involves a considerable number of logical operations. [50]

2.7.4 Level Sets Methods

In the level sets methods[50, 51], the free boundary is defined by the level line of a smooth function φ. The level set function is assumed to be positive in the liquid, negative

in the gas at least twice continuously differentiable. The motion is analyzed by advecting the values of φ with velocity field v, the variable φ satisfies:

$$\frac{\partial \varphi}{\partial t} + v \bullet \nabla \varphi = 0$$

this equation is deduced from the assumption that each particle of liquid moves with the liquid velocity along the characteristic curved. In the level sets approach, is transformed by setting $v_N = v \frac{\nabla \varphi}{\|\nabla \varphi\|}$ to obtain a Hamilton-Jacobi equation:

$$\frac{\partial \varphi}{\partial t} + v_N \|\nabla \varphi\| = 0$$

The quantity v_N denotes the normal velocity along the gradient of φ. The resolution of this equation needs only the normal component of the velocity in the neighborhood of the interface.

The advantage of the level set method is the ability to easily handle merging and pinching problem. [56] The drawback of the level sets approach is the degeneration of φ. When the gradient of φ vanishes in the neighborhood of the free surface, that is the function φ becomes flat, the accuracy on the approximation of the interface decreases dramatically.[51]

Chapter 3 Experiments

In this chapter, the experimental setup, experimental results and discussion will be presented. All the experiments can be classified into two catalogs. One set of experiments is using CaO, SiO_2, Al_2O_3, MgO, Fe_2O_3 slag reacted with MgO refractories. This set of experiments was conducted at the University of Wollongong in Australia by Dr. Brooks and Dr. Nightingale, and the results were analyzed at McMaster University by the author. The effect of Al_2O_3 in this slag is analyzed. Another set of experiments employed CaO-Al_2O_3 slag and MgO refractory. The experiments were conducted at different temperatures to determine the effect of reaction temperature and deduce the reaction mechanism. In this chapter, the first section will discuss the experimental setup for the system using CaO, SiO_2, Al_2O_3, MgO, Fe_2O_3 slag and MgO refractories. In the second section, the experimental system for CaO, SiO_2, slag and MgO refractories is presented.

3.1 Experiments on MgO(s)- CaO-SiO_2-MgO-FeO(l) System

This study is designed to investigate the dissolution of MgO refractory under static conditions. Experiments exposing MgO to different slag compositions and corrosion times have been performed to identify the dissolution mechanisms. Chemical analysis of refractories and slag was used to aid in understanding the kinetics of dissolution. An existing semi-empirical mathematical model was applied to the experimental results obtained.

3.1.1 Experimental Setup

Cylindrical MgO samples (20mm OD and 25mm in length) were used with a density of greater than 96% theoretical (3.46×10^3 kg/m^3). The composition of the MgO samples is listed in Table 3.1.* Master slags were prepared by mixing the appropriate amounts of high purity CaO, SiO_2, Al_2O_3, MgO and Fe_2O_3 in a tumble mixer for a minimum of 8 hours before melting the mixture in a platinum crucible at 1550^{o}C in air using a muffle furnace. The master slags were then ground and re-melted in the muffle furnace. This procedure was followed 3 times to produce a homogeneous slag. Two slag compositions were used in these experiments. The slag compositions used are listed in

Table 3.2; 140g of slag were used for each experiment.

Table 3.1 Chemical Composition of MgO Samples (wt%)

MgO [%]	97
Fe_2O_3 [%]	0.6
SiO_2 [%]	0.6
CaO [%]	1.2

* samples supplied by Rojan Advanced Ceramics, Henderson, Western Australia

Table 3.2 Slag compositions by XRF (wt%)

Weight%	CaO	SiO_2	Al_2O_3	MgO	FeO
Slag A	46	46	0	3	5
Slag B	36	36	20	3	5

A resistance heated vertical tube furnace was used for all experiments. The hot zone in the furnace was approximately 50mm long with a temperature variation of $\pm 2^{o}C$ at $1500^{o}C$ and $1535^{o}C$. Dried compressed air flowed through the furnace at a rate of 150ml/min. The MgO samples were partially immersed into slag for 15, 30, 60, and 90min at $1530^{o}C$ to an approximate depth of 10mm. They were lifted out of slag and quenched in water immediately upon completion of the experiment.

Chemical analyses of the slags recovered from the experiments were carried out by Bluescope Steel laboratory in Port Kembla using well established XRF techniques and standards.

Each of the quenched samples was sectioned using a diamond wheel and ground and polished to a 1μm finish using standard methods. Polished samples were gold coated before SEM analysis. SEM/EDX analysis was conducted by a Philips 515 SEM\Link QX2000. EDX was used for investigating the composition of reaction products. An accelerating voltage of 7 keV was used for the analysis.

3.1.2 Experimental Results:

A total of 8 experiments were carried out. Photographs of refractory samples were taken and the profiles of the refractory samples are summarized in Figure 1. Clear slag-line corrosion was observed in all samples. It was also that the depth of corrosion increased with time for both slag compositions. Slag B (20% Al_2O_3) had a lower corrosion rate than slag A (without Al_2O_3).

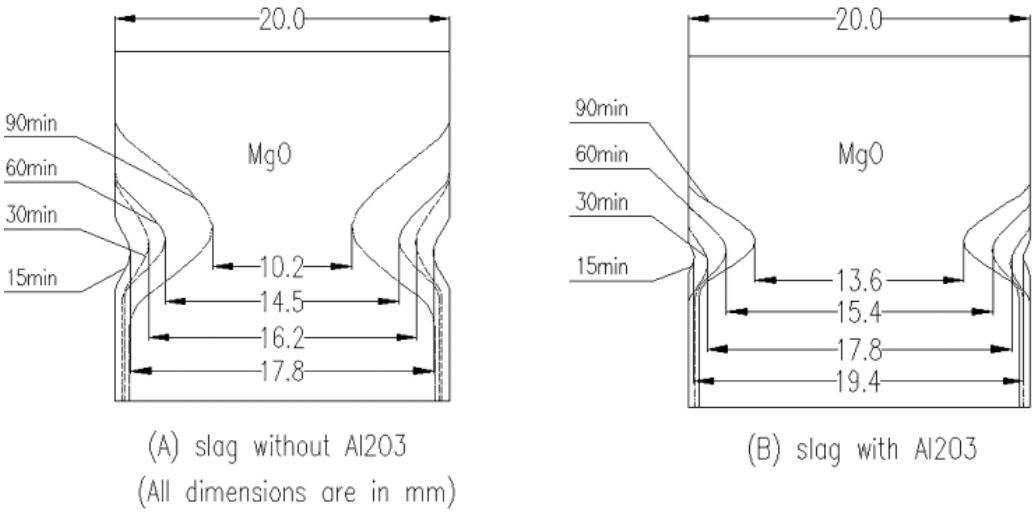

Figure 3.1 Change in diameter of MgO samples as a function of time.

Upward drilling, another surface tension driven phenomenon was also observed for all samples. The phenomena of upward drilling was described by Busby[52] and Preston[53]. This section is not focused on this aspect of refractory corrosion, so the upward drilling is not included in the analysis.

A typical SEM image of the interface of the sample reacted with slag A after 15 minutes is shown in Figure 3.2(a) and the interface of the sample reacted with slag B after 30 minutes is shown in Figure 3.2(b). It was found that the refractory/slag interfaces were smooth, with no evidence of grains being dislodged. The slag had penetrated into the MgO grain boundary network in the region near the interface, but the MgO grains themselves remained intact. The typical grain boundary EDS analysis spectrum for sample reaction with slag B after 30 minutes is shown as Figure 3.3(a) and the typical refractory grain EDS analysis spectrum for this sample is shown in Figure 3.3(b). SiO_2 and CaO were detected in the MgO grain boundaries and no SiO_2 or CaO found in MgO grains, confirming that the grain boundaries have undergone slag penetration. The MgO concentration in the bulk slag was found to increase with time, as shown in Figure 3.5.

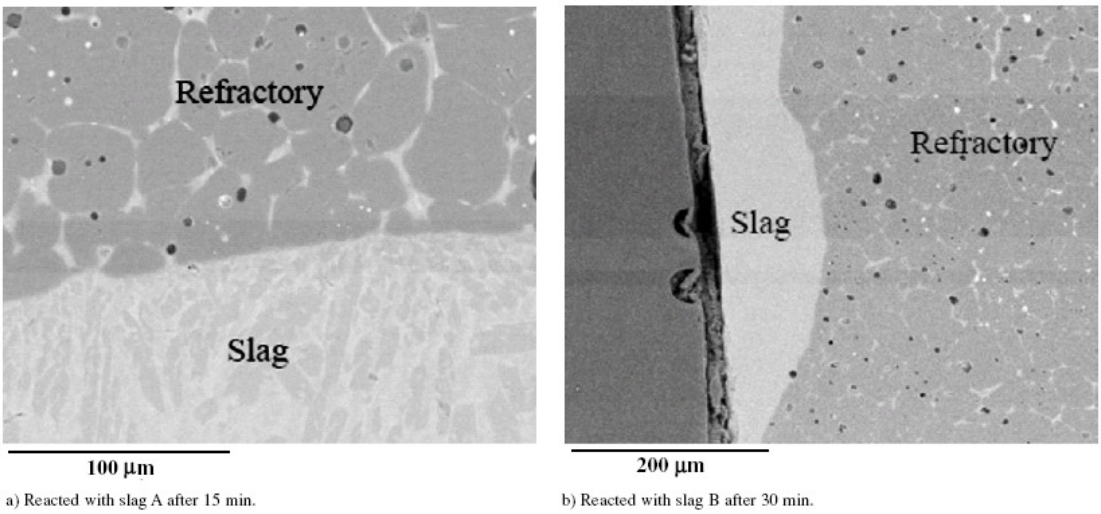

Figure 3.2 Typical SEM micrograph of the slag/MgO interfacial region

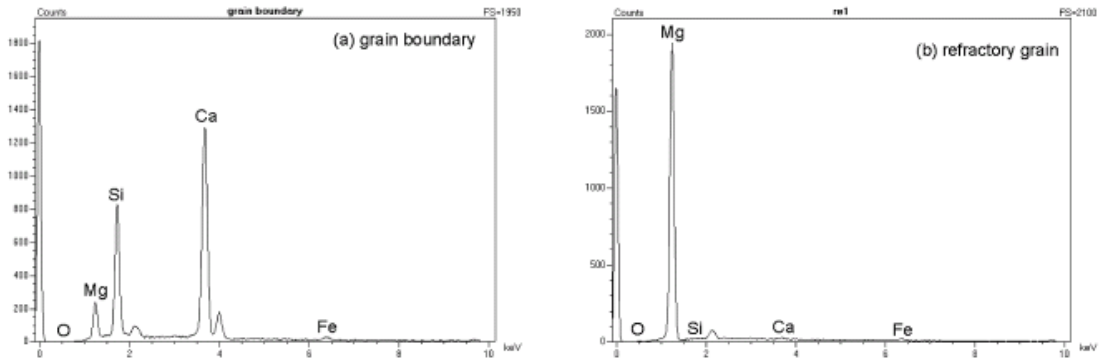

Figure 3.3 EDS spectrums for grain boundary and refractory, reacted with slag A after 90 minutes

A new phase was found on the surface of all magnesia samples immersed in Slag B (20% Al_2O_3). Figure 3.6 shows typical micrographs of this new phase for refractory after exposure to the Al_2O_3 containing slag B for 15 minutes. Figure 3.7 shows typical micrographs of the slag/refractory interface after 90 minutes. EDS analyses show that this new phase contains much more Al_2O_3 than the surrounding slag phase, ranging from 60%~72%. This phase also contained MgO and iron oxide (when analyzed as FeO, concentration was 6%~11%). The composition and cubic form of the crystals combined with the phase diagram of Al_2O_3-SiO_2-CaO-MgO system with 20% of Al_2O_3 shown in Figure 3.4 all suggests that the new phase is $MgO \cdot Al_2O_3$ spinel, with some Fe in solid solution.

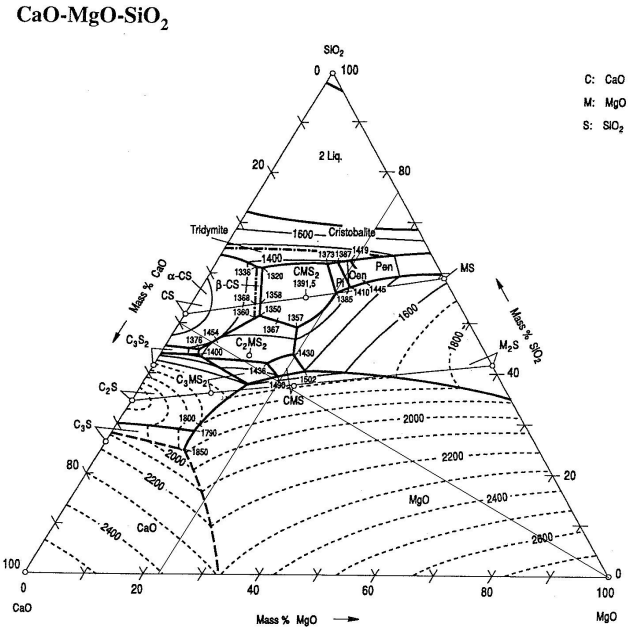

(A)

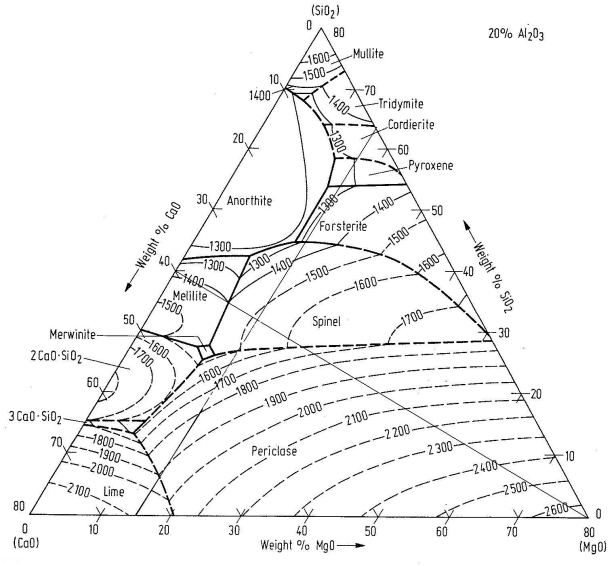

(B)

Figure 3.4

A: Phase diagram of CaO-SiO_2- MgO system [7]

B: Phase diagram of Al_2O_3-SiO_2-CaO-MgO system with 20% of Al_2O_3 [7]

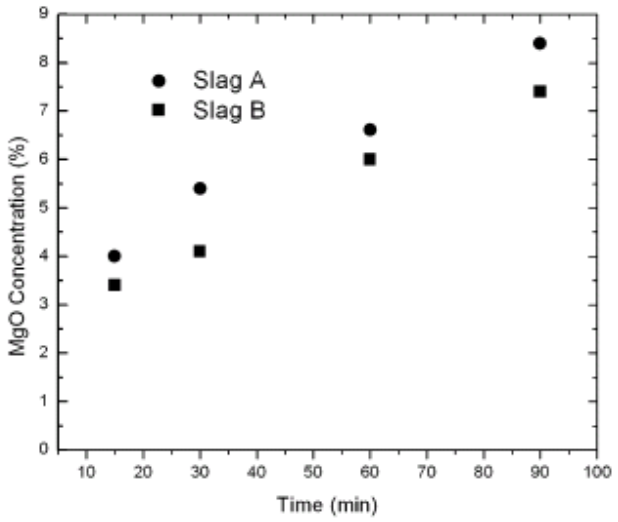

Figure 3.5 Wt% MgO by XRF in the bulk slag as a function of time

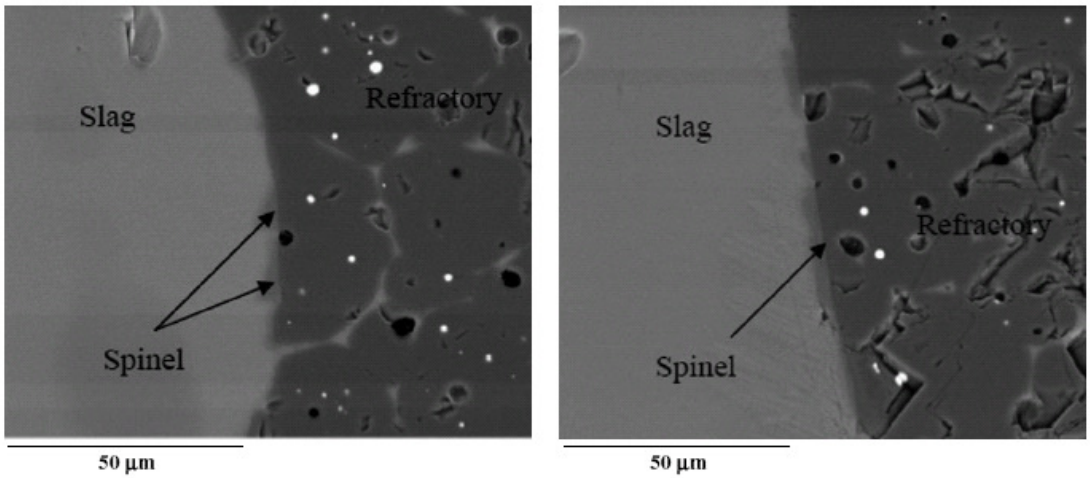

Figure 3.6 Micrograph of slag/MgO interface, MgO immersed in slag B after 15 minutes

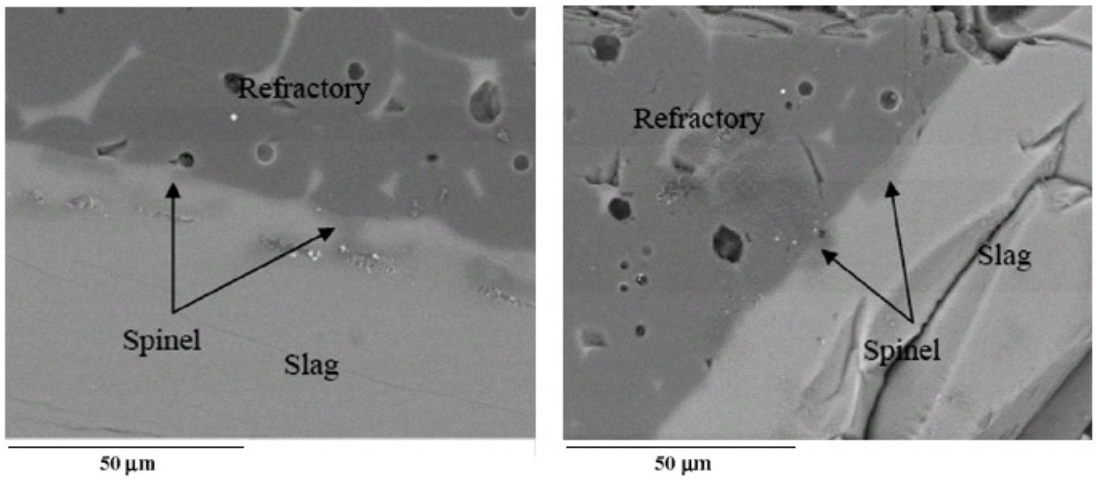

Figure 3.7 Micrograph of slag/MgO interface, MgO immersed in slag B after 90 minutes

3.1.3 Semi-empirical Model:

Hrma[40] studied the dissolution rate governed by surface free convection caused by a surface tension gradient, as presented in Section 2.6.1. In his model, he developed a semi-empirical mathematical model to describe the dissolution rate. In this section, Hrma's[40] mathematical model was used to analyze the experimental data from this study by applying Eq.(3.1). The time dependence of the change in diameter at the flux line is shown in Figure 3.8. By drawing the slope of the curve, the dissolution rate u_s could be found. Table 3.3 summarizes the material constants[7] and the rates of dissolution. These data were used to calculate the value of B, which is also listed in Table 3.3.

$$u_s = B\Delta C\left(\frac{D_o^2 \Delta\sigma^* g}{v}\right)^{1/3} \qquad (3.1)$$

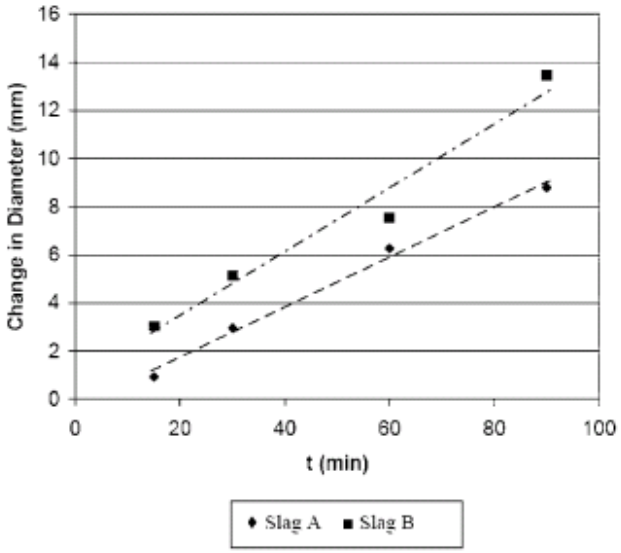

Figure 3.8 Time dependence of dissolution of MgO-Slag systems

Table 3.3 The properties of MgO-Slag system

	Density (kg/m^3)	Viscosity (Pa·S)	Diffusion coefficient (m^2/s)	Concentration gradient
Slag A	2.74×10^3	0.23	5.47×10^{-9}	0.20
Slag B	2.82×10^3	0.50	2.51×10^{-9}	0.14

	Surface tension (N/m)	Surface tension gradient (N/m)	Contact angle (^{o})	Dissolution rate (m/sec)	B
Slag A	400	30	10	2.33×10^{-6}	0.19
Slag B	460	30	10	1.67×10^{-6}	0.44

In general, surface tension data on slags is inconsistent in the literature and is a source of error in such calculations. The MgO diffusion coefficient in the MgO-CaO-SiO_2-Al_2O_3 system is not available in the literature, so the MgO diffusion coefficient in MgO-CaO-SiO_2 system was used for Slag A instead. However, the higher viscosity of Slag B does suggest that the diffusion coefficient will be lower, as per the Stokes-Einstein equation as Eq.(3.2), where μ is the viscosity, r is the radius of diffusion species, K_B is Boltzmann constant, T is temperature. As Eq.(3.2) suggests an inverse relationship between D and viscosity, D was recalculated for Slag B by using diffusion coefficient of Slag A and relation of D and μ. The diffusion coefficient was calculated as 2.51×10^{-9} m^2/s.

$$D = \frac{K_B T}{6\pi\mu r} \tag{3.2}$$

As described in the literature review (section 2.2.3), because of the spinel formation, the dissolution of MgO in Slag B is indirect dissolution. The dissolution rate for indirect dissolution at steady state is controlled by the concentration gradient between the saturation concentration of MgO at the solid-liquid interface, for this case, which is spinel phase, and the concentration in the bulk. The saturation concentration of MgO at the spinel phase can be obtained from phase diagram at Figure 3.4 (B). From phase diagram, MgO saturation concentration can be obtained as 17%. At the beginning of dissolution, MgO concentration is 3%. The concentration gradient for the dissolution at the beginning stage is $\triangle c_{spinal} = c_{eq} - c_i = 14\%$. From the phase diagram at Figure 3.4 (A), MgO concentration for slag A also can be obtained as 23%. The concentration gradient at the

beginning stage is $\triangle c_{MgO} = c_{eq} - c_i = 20\%$. The driving force for the dissolution is concentration gradient. So the ratio between concentration gradient in these two systems is: $\frac{\triangle c_{spinel}}{\triangle c_{MgO}} = \frac{14\%}{20\%} = 0.70$. The ratio of dissolution rate between these two systems is calculated as: $\frac{1.67 \times 10^{-6}}{2.33 \times 10^{-6}} = 0.72$. The consistency of these two ratios supports the hypothesis that spinel layer formation slows down MgO dissolution rate by decreasing the MgO saturated concentration at the solid-liquid interface. In this system, once formation and dissolution of the spinel reaches the steady state, the thickness of the spinel layer remains constant. The rate determining step of dissolution MgO is the dissolution of spinel. The spinel layer thickness doesn't have any affect on the dissolution rate. The spinel layer has a lower saturated MgO concentration, which results in a lower concentration gradient between spinel and bulk slag. The driving force of MgO dissolution is concentration gradient between slag-refractory interface and the bulk slag. So, the lower the concentration gradient, the lower the dissolution rate.

3.1.4 Kinetic Analysis Based on Slag Chemistry:

Mass transfer coefficients were calculated using the chemical analyses of the slag, the measured surface area of the sample at the end of the experiment and the volume of the slag using the following equation:[54]

$$-In\left[\frac{(C_{eq}-C_f)}{(C_{eq}-C_i)}\right]=k\frac{At}{V} \tag{3.3}$$

where V is volume of slag, t is time, A is the MgO-liquid interfacial area, C_{eq} is the concentration of MgO at the interface, C_f is the final concentration in the slag and C_i is initial concentration of MgO in the slag.

Calculation of the interfacial area allowed the effective mass transfer coefficient K to be determined using Eq.(3.3). Results are shown in Figure 3.9.

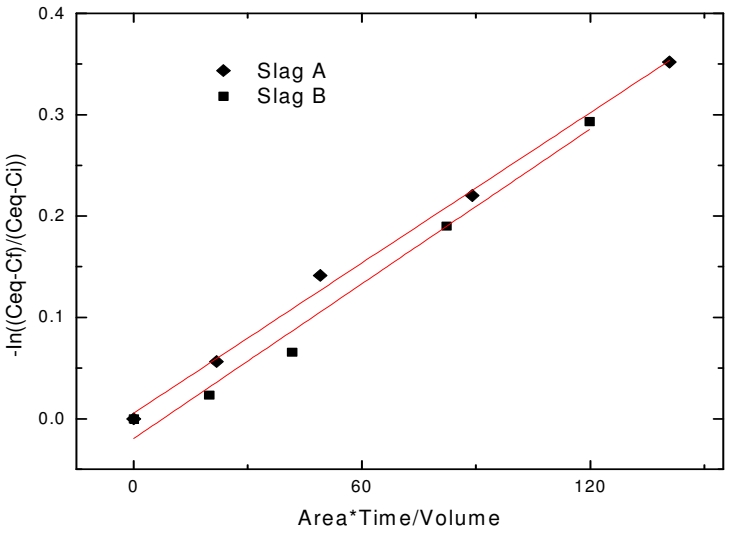

Figure 3.9 Effective mass transfer coefficient calculation

From this figure, the effective mass transfer coefficients can be obtained as:

K=2.47×10^{-6}m/s for slag with no Al_2O_3

K=2.55×10^{-6}m/s for slag containing Al_2O_3

The effective mass transfer coefficients calculated from Eq.(3.3) show no difference between those two different systems. Since the saturated MgO concentration used in the case of slag containing Al_2O_3 system is considered as MgO concentration in equilibrium with the spinel phase, the same effective mass transfer coefficients further proved that formation of spinel phase slow down MgO dissolution rate by lowering the saturated MgO concentration at the interface. By using these effective mass transfer coefficients, the boundary layer thickness can be estimated to be about 2mm. This is in agreement with the value measured by Sandhage and Yurek[12] for static dissolution of Al_2O_3. It is also important to note that the change in bulk concentration measured reflected not just the process of slag line corrosion but also some contribution from upward drilling and general dissolution below the slag line and thus these values for the mass transfer coefficients are only indicative.

3.1.5 Discussion:

Experiments with Slag A (0% Al_2O_3)

MgO underwent direct dissolution in the alumina free slag, with no solid reaction product forming at the interface. Calculation of MgO saturation concentration for this slag performed using MTDATA software* gives a value of 21.2% at 1530°C. The MgO concentration in the bulk slag is considerably lower than this concentration at the

* MTDATA is a commercial thermodynamic software package developed at the National Physical Laboratory in the UK, which is able to calculate complex multi-component phase equilibria in gas-liquid-

interface, so there was still significant driving force for dissolution even after 90 minutes. Although, slag was found in the refractory grain boundary, penetration of liquid slag was not the main mechanism for the refractory to degrade. The microstructure of the refractory shown in Figure 3.2 shows smooth interface, which would not be the case if refractory grains were dislodged by slag penetration. Dissolution is the main mechanism for refractory degradation in this series of experiments.

The general shape of the corrosion profile suggests that fluid flow, both parallel and normal to the slag refractory interface, occurred simultaneously. This is consistent with the work of Mukai et al[33]. The results from the Hrma model are also consistent with the observed loss of refractory at the slag line and support the idea that surface tension driven flow explains this phenomenon. The model is based on an assumption that dissolution is mass transfer controlled. If so, the slag at the interface should be saturated with solute, and a boundary layer with a concentration gradient across its thickness would be expected to form. The calculation of boundary layer thickness will be discussed next in the kinetic analysis section.

The general shape of the corrosion profiles and the successful application of Hrma model support the proposition that the overall process is controlled by surface driven mass transfer, even though no boundary layer could be observed. This is further supported by

---

solid system. It uses a Gibbs Energy minimization routine to establish the thermodynamic equilibrium of a defined system.

work conducted on the same system under conditions of forced convection which show a change from mass transfer to chemical reaction rate control occurs as sample rotation speeds increase.[39]

Experiments with Slag B (20% Al_2O_3)

When MgO reacted with the slag containing Al_2O_3, the dissolution rate was lower than for slag containing no Al_2O_3. A spinel phase, $MgO \cdot Al_2O_3$ was observed at slag-MgO interface. Maximum theoretical MgO concentration for this slag gives a value of 17% at 1530^{o}C. The measured MgO concentration in the bulk slag is considerably lower than this in all cases. Slag line corrosion profiles were still consistent with surface tension driven flow, but the value of B was not in the range predicted by the Hrma model. The formation of a solid reaction product at the interface complicates the analysis of mechanisms controlling dissolution. The formation of spinel in Al_2O_3 containing slag leads to indirect dissolution, which is not considered in Hrma model. However, by using the saturated MgO concentration in spinel phase, Hrma model still can be applied to indirection dissolution.

By comparing the dissolution rate measured from the change in MgO rod diameter with time between slag A and slag B, it is found that the ratio of dissolution rate between slag A and slag B is very close to the ratio of concentration gradient of MgO at the initial stage of dissolution. This finding proves that the spinel phase lowers the MgO dissolution rate by lowering the saturation concentration at the interface. The lower the saturated

concentration gradient, the lower the concentration gradient between the slag-MgO interface and bulk, which is the driving force for the dissolution process.

The development of a large boundary layer would be in agreement with the results published for alumina dissolution in a MgO bearing slag. Under static conditions a boundary layer thickness greater than 1600μm was found for the dissolution of alumina by Sandhage and Yurek.[12]

3.1.6 Conclusion:

The corrosion of MgO refractory in SiO_2-CaO-FeO_x-MgO slag and Al_2O_3- SiO_2-CaO-FeO_x-MgO slag system has been studied at 1530^oC from 15min to 90min. The change of MgO concentration with time was observed. There was significant evidence of a spinel phase having formed at the slag/refractory interface for slags containing 20wt.% Al_2O_3. The existence of spinel seems to have retarded the dissolution of the refractory. The Hrma model, based on the assumption that surface tension driven mass transfer controls the dissolution process and a simplified geometry and flow field, provided a reasonable estimate of the rate of MgO dissolution for direct dissolution. The same mechanism for indirect dissolution is verified by comparing the ratios of dissolution rate and saturated concentration of MgO at the slag-refractory interface. The kinetic analysis is performed based on slag chemistry. The effective mass transfer coefficient is calculated from the kinetic analysis. The systems with and without Al_2O_3 have the same mass transfer coefficient. This proved that the indirect dissolution retards the MgO dissolution rate by

formation of spinel phase, which lowers the saturation concentration of MgO at the interface.

3.2 Experiments on MgO(s)-CaO-Al_2O_3(l) system:

The experiments discussed in the foregoing section were conducted at the University of Wollongong in Australia by Dr. Brooks and Dr. Nightingale, and the results were analyzed at McMaster University by the author. To further investigate the dissolution of MgO refractory under static conditions, the following experiments were designed. Experiments based on MgO exposed to slag for different corrosion times over a range of temperatures have been performed to identify the dissolution mechanisms. Chemical analysis of refractories and slag was used to aid in understanding the kinetics of dissolution. An existing semi-empirical mathematical model was applied to the experimental results obtained.

3.2.1 Experimental Setup:

Cylindrical MgO samples (20mm OD and 25mm in length) were used with a density of greater than 99.6% theoretical (3.3×10^3 kg/m^3). The composition of the MgO samples is listed in Table 3.4.* Master slags were prepared by mixing the appropriate amounts of high purity CaO and Al_2O_3 in a platinum crucible for 40 minutes at 1600°C in air. The

* samples supplied by Custom Technical Ceramic Company in USA

master slags were then ground and re-melt. This procedure was followed 3 times to produce a homogeneous slag. In order to minimize the uncertainty of high temperature properties in the experiments, simple slag compositions were chosen. $CaO\text{-}Al_2O_3$ slag was used in the experiments. The slag composition after pre-melt is listed in Table 3.5; 60g of slag were used for each experiment.

Table 3.4 Major Chemical Composition of MgO Samples (wt%)

MgO [%]+ additive	99.6
Fe_2O_3 [%]	0.01
SiO_2 [%]	0.03
CaO [%]	0.02

A CM 1710BL high temperature box furnace was used for all experiments. The apparatus is shown in Figure 3.10. The hot zone in the furnace was approximately 50mm long with a temperature variation of $\pm 2^oC$ at 1550^oC and 1650^oC. 60g slag is used for all experiment. A platinum crucible is used to contain slag. The MgO rod is supported by an Al_2O_3 tube. The MgO samples were partially immersed to an approximate depth of 20mm into slag for certain time at a design temperature. They were lifted out of slag and quenched in air immediately upon completion of the experiment. Experimental times of 30, 60, 90, 120 and 150 minutes were employed at temperature of 1575^oC, 1600^oC,

1625^{o}C and 1650^{o}C. The minimum temperature was set to be sufficient to allow a free flow of the slag; the maximum was the highest temperature obtainable in the furnace.

Table 3.5 Slag compositions by ICP (wt%)

Weight%	CaO	Al_2O_3
Slag	48	52

Chemical analyses of the slags recovered from the experiments were carried out using well established ICP techniques and standards.

Each of the quenched samples was sectioned using a diamond wheel and ground and polished to a 1μm finish using standard methods. Polished samples were gold coated before SEM analysis. SEM/EDX analysis was conducted by a Philips 515 SEM\Link QX2000. EDX was used for investigating the composition of reaction products. An accelerating voltage of 7 keV was used for the analysis.

To enhance the flow of the thesis, the details of experimental error analysis are presented in Append (2).

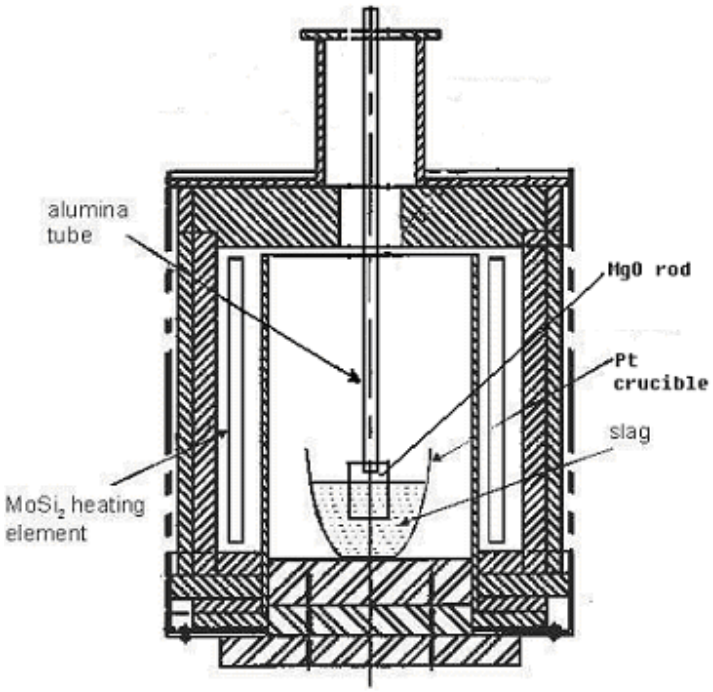

Figure 3.10 Sketch of experimental setup

3.2.2 Experimental Results:

A total of 20 experiments were carried out. Clear slag-line corrosion was observed in all samples. A typical optical microscopy image of the interface of a sample reacted with slag for 90 minutes at 1625^{o}C is shown in Figure 3.11(a) and the SEM image of the same sample is shown in Figure 3.11(b). It was found that the refractory/slag interfaces were smooth, with no evidence of grains being dislodged. The slag had penetrated into the MgO grain boundary network in the region near the interface, but the MgO grains themselves remained intact. A typical grain boundary EDS analysis spectrum for a sample after 60 minutes exposure to slag is shown as Figure 3.12(a) and a typical

refractory grain EDS analysis spectrum for this sample is shown in Figure 3.12(b). Al_2O_3 and CaO were detected in the MgO grain boundaries and no Al_2O_3 or CaO was found in MgO grains, confirming that the grain boundaries have undergone slag penetration. The MgO concentration in the bulk slags was found to increase with time, as shown in Figure 3.13.

The maximum corrosion distance is defined as the change of MgO rod radius at the meniscus range. The maximum corrosion distance as a function of time at different temperatures is shown in Figure 3.14. Since the meniscus is where refractory failure occurs. The maximum corrosion distance can be used to represent the degree of refractory degradation. The slope of the maximum corrosion distance vs. time is defined as corrosion rate.

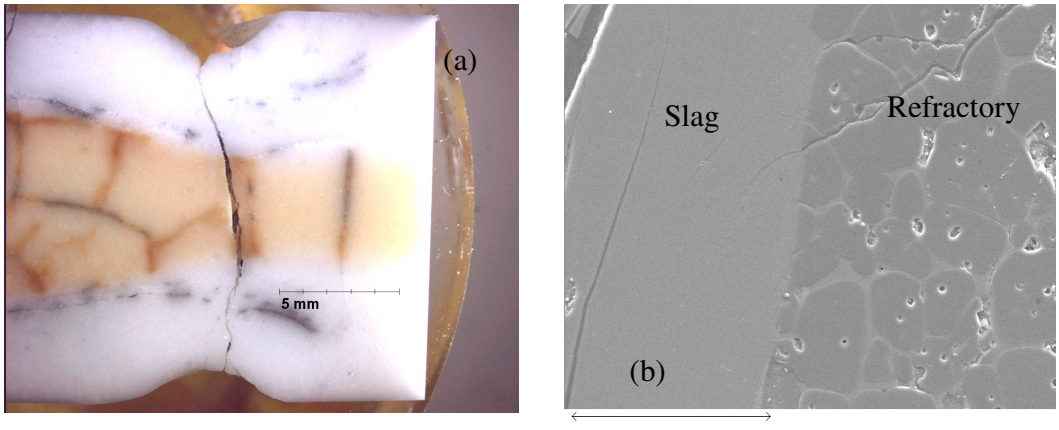

Figure 3.11 Typical optical and SEM micrograph of the slag/MgO interfacial region, reacted at 1625°C for 90 minutes

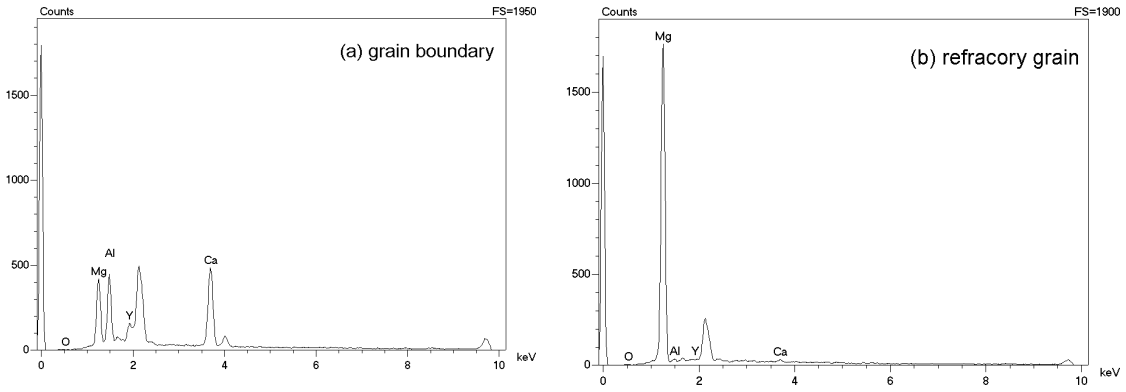

Figure 3.12 EDS spectrums for grain boundary and refractory, reacted at 1600°C for 120 minutes

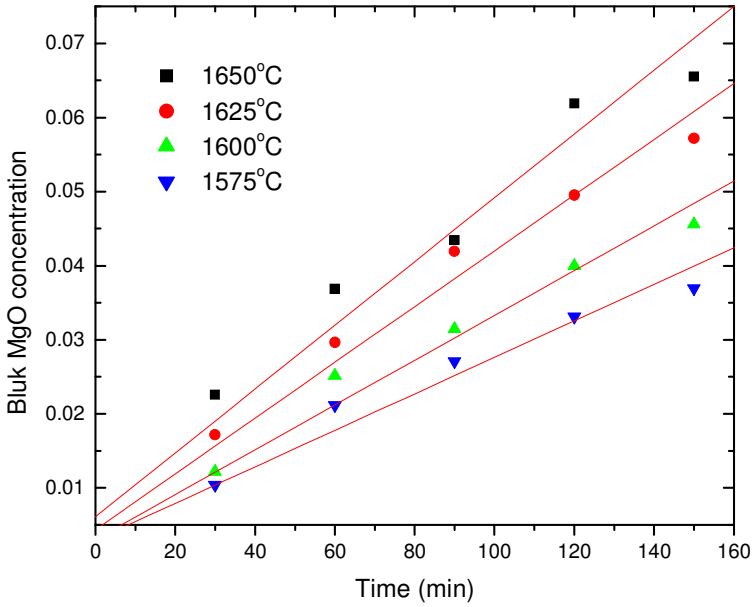

Figure 3.13 MgO concentration in the bulk by ICP as a function of time

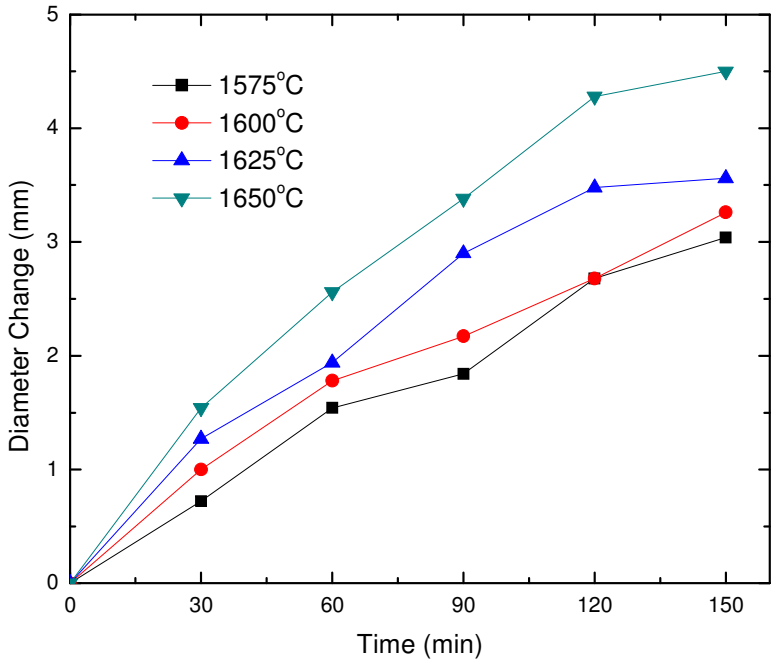

Figure 3.14 Diameter change as a function of time

3.2.3 Mathematical Model:

Hrma's[40] mathematical model was used to analyze the experimental data from this study. The time dependence of the change in diameter at the flux line is shown in Figure 3.14. By drawing the slope of the curve, the dissolution rate u_s could be found. Table 3.6 summarizes the material constants[7] and the rates of dissolution. These data were used to calculate the value of B, which is also listed in Table 3.6.

Table 3.6 The properties of $CaO\text{-}Al_2O_3$ Slag system

	Density (kg/m^3)[7]	Viscosity (Pa·S)[7]	Diffusion coefficient (m^2/s)[7]	Concentration gradient
1575°C	2.82×10^3	0.50	8.78×10^{-9}	0.11
1600°C	2.82×10^3	0.43	1.02×10^{-8}	0.12
1625°C	2.82×10^3	0.35	1.25×10^{-8}	0.13
1650°C	2.82×10^3	0.25	1.75×10^{-8}	0.14

	Surface tension (mN/m)[7]	Surface tension gradient (mN/m)	Contact angle (°)[7]	Dissolution rate (m/sec)	B
1575°C	583	205	10	3.40×10^{-7}	0.34
1600°C	580	200	10	3.76×10^{-7}	0.32
1625°C	577	195	10	4.04×10^{-7}	0.28
1650°C	573	190	10	5.00×10^{-7}	0.28

The B numbers obtained from Hrma's model are 0.28~0.34. Hrma predicted that the B number should be 0.3~0.4. It is found that the model results are very sensitive to the surface tension data and the diffusion coefficient. The accuracy of those data is very

limited, which could account for the difference between measured and expected value for B.

3.2.4 Discussion:

$CaO\text{-}SiO_2$ slag reacted with MgO refractory; there is no spinel formation is observed in the SEM pictures. At various temperatures from 1575°C~1650°C, the progress in the corrosion profiles can be observed.

The general shape of the corrosion profile suggests that the fluid flow both parallel and nornal to the slag refractory interface occurred simultaneously. This is consistent with the work of Mukai et al.[33] The results from Hrma model are also consistent with the observed loss of refractory at the slag line and support the idea that surface tension driven flows can explain this phenomenon. The model is based on an assumption that dissolution is mass transfer controlled. If so, the slag at the interface should be saturated with solute, and the formation of a boundary layer with a concentration gradient across its thickness would be expected to form. The lifting of the sample out of the slag at the end of the experiments is likely to have disturbed any boundary layer that may have formed, so that reliable measurements of its thickness were not possible.

The general shape of the corrosion profiles and the successful application of Hrma model support the proposition that the overall process is controlled by surface driven mass transfer, even though no boundary layer could be observed.

3.2.5 Kinetic Analysis of Slag Chemistry:

Mass transfer coefficients were calculated using the chemical analyses of the slag, the measured surface area of the sample at the end of the experiment and the volume of the slag using the following equation:

$$-In\left[\frac{(C_{eq}-C_f)}{(C_{eq}-C_i)}\right]=k\frac{At}{V} \qquad (3.4)$$

where V is volume of slag, which is calculated as (initial slag volume)*(1+MgO concentration in the bulk slag), t is time, A is the MgO-liquid reaction area, the surface area of groove at the slag line is used area in this calculation, C_{eq} is the concentration of MgO at the interface, C_f is the final concentration in the slag and C_i is initial concentration of MgO in the slag.

The greatest uncertainty in Eq.(3.4) is reaction area A. The simplest interpretation is that A is the entire surface immersed in the slag. However as mass transfer occurs at the slag-refractory interface, the area of the corrosion groove maybe more important. So the values of mass transfer coefficient *k* are presented by using different reaction area. Figure 3.15 ~ Figure 3.18 use groove area for the area to calculate *k*. The entire immersed refractory area also used to calculate *k* and summarized in Table 3.7.

Calculation of the interfacial area allowed the effective mass transfer coefficient *k* to be determined using Eq.(3.4). Results are shown in Figure 3.15-Figure 3.18.

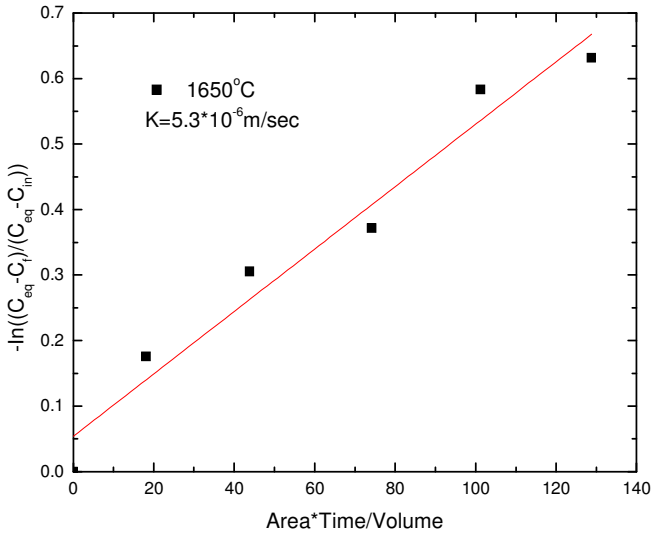

Figure 3.15 Kinetic plot of $CaO\text{-}Al_2O_3$(l)-MgO(s) at 1650°C, assuming first-order rate

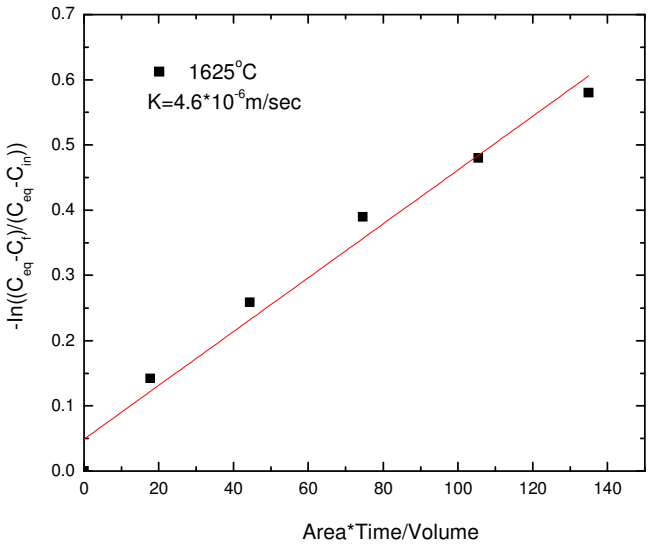

Figure 3.16 Kinetic plot of $CaO\text{-}Al_2O_3$(l)-MgO(s) at 1625°C, assuming first-order rate

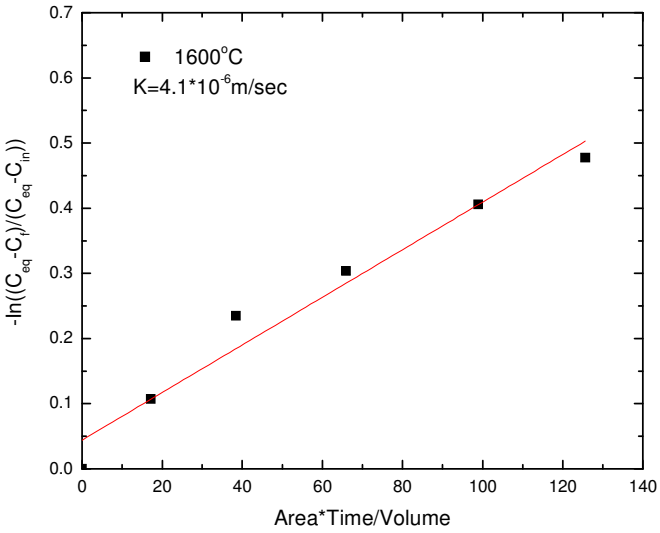

Figure 3.17 Kinetic plot of $CaO\text{-}Al_2O_3$(l)-MgO(s) at 1600°C, assuming first-order rate

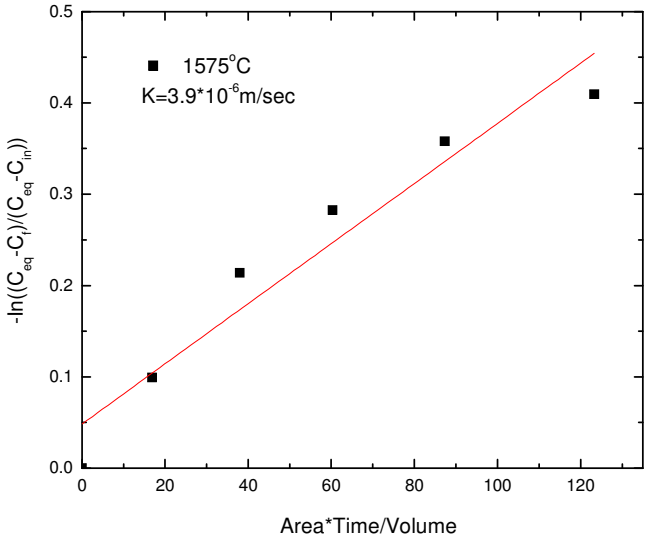

Figure 3.18 Kinetic plot of $CaO\text{-}Al_2O_3$(l)-MgO(s) at 1575°C, assuming first-order rate

The effective mass transfer coefficient for the system varies from 5.3×10^{-6}m/s to 3.9×10^{-6}m/s, and decreases with decreasing of temperature, as plotted in Figure 3.19.

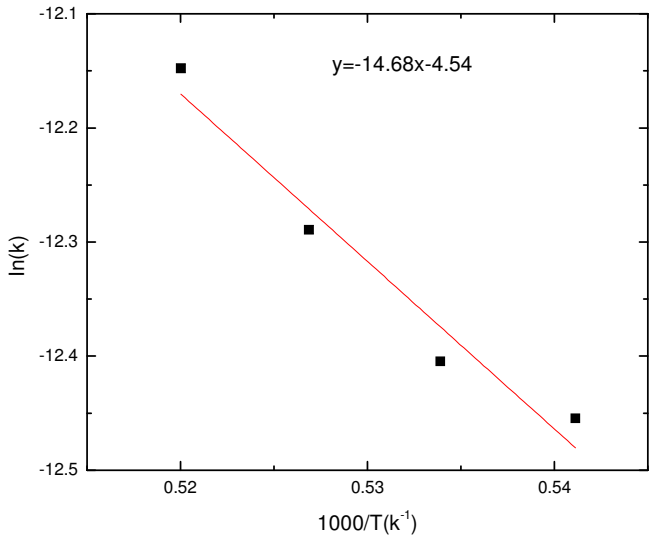

Figure 3.19 Kinetic plot between In(k) and 1000/T from experimental data

The effective mass transfer coefficient is dependent of temperature within the experimental temperature range. The activation energy for the mass transfer can be calculated by plotting In(k) vs. 1/T as show in Figure 3.19. The activation energy was found to be 122 kJ/mol. This value is slightly higher than the activation energy for a diffusion controlled process, i.e., 20~80kJ/mol,[59] but much less than the activation energy of chemical reaction, i.e., 400 to 600 kJ/mol.[58] This supports the hypothesis that the whole MgO refractory dissolution process is a mass transfer control process.

The effective mass transfer coefficient is simply defined as $\frac{D}{\delta}$, where D is the diffusion coefficient, and δ is the boundary layer thickness. By using these effective mass transfer coefficients, the boundary layer thickness can be estimated to be about 1.6mm. This is in agreement with the value measured by Sandhage and Yurek[12] for static dissolution of Al_2O_3 and the results from the experiments of MgO(s)-CaO-SiO_2-FeO(s) system described in section 3.1. It is also important to note that the change in bulk concentration measured reflects not just the process of slag line corrosion but also some contribution from upward drilling and general dissolution below the slag line. Therefore the mass transfer coefficients are only indicative.

The reaction area used in Eq.(3.4) is the groove area at the slag line. The same calculation is performed by using Eq.(3.4), but replacing the reaction area with the surface area of MgO rod contacting with slag, including the area blew the slag line and the bottom of the rod. This calculation can be used to estimate the overall mass transfer coefficient. The results of effective dissolution rate are summarized in Table 3.7.

Table 3.7 summarized the dissolution rate from kinetic of slag chemistry by using the groove area, the dissolution rate from kinetic of by slag chemistry by using the whole interface area, and the dissolution rate determined by linear fitting depth of erosion groove to Hrma's model.

To compare the dissolution rate from Hrma's model, which is calculated from the max corrosion distance on slag line by time, with the dissolution rate calculated from kinetic analysis, take the following steps to convert the linear dissolution rate to volume dissolution rate.

Assuming the eroded groove is cylindrical trough, the dissolved volume of MgO rod at slag line can be calculated as:

$$V_{MgO} = \frac{\pi r^2}{2} \bullet \pi d \tag{3.5}$$

where r is the radius of the cylindrical trough and d is the diameter of original MgO rod.

The volume of dissolved MgO as a function of cylindrical trough radius can be expressed as:

$$\frac{dV_{MgO}}{dr} = d(\frac{\pi r^2}{2} \bullet \pi d) / dr = \pi^2 rd \tag{3.6}$$

The dissolved MgO concentration as a function of time can be expressed as:

$$\frac{dc}{dt} = \frac{d((V_{MgO} \bullet \rho_{MgO}) / V_{slag})}{dt} \tag{3.7}$$

Density of MgO ρ_{MgO} is a constant, Eq(3.7) can be transformed as:

$$\frac{dc}{dt} = \frac{d(V_{MgO} / V_{slag})}{dt} \bullet \rho_{MgO} = \rho_{MgO} \bullet (V_{slag} \bullet \frac{dV_{MgO}}{dt} - V_{MgO} \bullet \frac{dV_{slag}}{dt}) / V_{Slag}^{\ 2} \tag{3.8}$$

Since, $\frac{dV_{slag}}{dt} = \frac{d(V_{MgO} + V_{slag(i)})}{dt}$ (3.9)

Where $V_{slag(i)}$ is initial slag volume.

$$\frac{dV_{slag}}{dt} = \frac{dV_{MgO}}{dt} \tag{3.10}$$

Eq(3.8) can be simplified as:

$$\frac{dc}{dt} = \frac{dV_{MgO}}{dt}\left(\frac{1}{V_{Slag}} - \frac{V_{MgO}}{V_{Slag}^{2}}\right)\bullet\rho_{MgO} \tag{3.11}$$

Assume the whole process is followed first order kinetics:

$$\frac{dc}{dt} = \frac{k\bullet A}{V_{slag}}\bullet(c_{eq} - c_f) \tag{3.12}$$

Where c_f is bulk MgO mass per units slag volume, c_{eq} is MgO mass per units slag volume at the slag-MgO interface. Eq(3.11) equals to Eq(3.12), the following equation is obtained:

$$\rho_{MgO}\bullet\frac{dV_{MgO}}{dt}\left(\frac{1}{V_{Slag}} - \frac{V_{MgO}}{V_{Slag}^{2}}\right) = \frac{k\bullet A}{V_{slag}}\bullet(c_{eq} - c_f) \tag{3.13}$$

where $\frac{V_{MgO}\bullet\rho_{MgO}}{V_{Slag}} = c_f$, $\frac{dV_{MgO}}{dt} = \frac{dV_{MgO}}{dr}\frac{dr}{dt} = \pi^2 rd\bullet\frac{dr}{dt}$, $A = \pi rd$

Separate the variables and simply Eq(3.13), the rate can be expressed in linear dissolution rate as:

$$k = \pi\frac{(\rho_{MgO} - c_f)}{(c_{eq} - c_f)}\frac{dr}{dt} \tag{3.14}$$

Where $\frac{dr}{dt}$ is the radius change by time, which is half of the linear dissolution rate.

The effective mass transfer coefficient calculated from Eq.(3.14) is also summarized in Table 3.7.

Table 3.7 Comparison of mass transfer coefficients obtained by kinetic analysis of slag chemistry and measurement of linear dissolution

Experimental Temperature	Mass transfer coefficient (m/sec) calculated from linear dissolution using Eq(3.14)	Mass transfer coefficient (m/sec) from kinetic analysis of slag chemistry	Mass transfer coefficient (m/sec) from kinetic analysis of slag chemistry with total reaction area
1575°C	7.15×10^{-6}	3.9×10^{-6}	7.2×10^{-7}
1600°C	7.37×10^{-6}	4.1×10^{-6}	8.1×10^{-7}
1625°C	7.38×10^{-6}	4.6×10^{-6}	9.7×10^{-7}
1650°C	8.87×10^{-6}	5.3×10^{-6}	1.1×10^{-6}

The dissolution rates calculated from kinetic analysis of slag chemistry with total reaction area are significantly lower than the dissolution rate calculated from kinetic analysis of slag chemistry but with the reaction area of groove surface area only. The area of groove surface is A_1 and the total area is A_t. The mass transfer coefficient calculated with total area is k_t, the mass transfer coefficient calculated with groove surface area is k_1 and the

mass transfer coefficient for on the area blow the slag line and on the bottom of the rod is k_2. The overall dissolution rate can be expressed as:

$$\frac{dc}{dt} = \frac{k_t \bullet A_t}{V_{slag}} \bullet (c_{eq} - c_f) \tag{3.15}$$

To calculate mass transfer coefficient based on groove surface area only, the assumption is made that there is no dissolution from the MgO rod blow the slag line and no dissolution from the bottom of the rod. So the dissolution rate also can be expressed as:

$$\frac{dc}{dt} = \frac{k_1 \bullet A_1}{V_{slag}} \bullet (c_{eq} - c_f) \tag{3.16}$$

So a greater surface area results a smaller mass transfer coefficient. In this calculation, it is assumed that k_2=0. In real case, there is dissolution from the MgO rod blow the slag line and also from the bottom of the rod, so $k_2 \neq 0$. However, dissolution from these sites is slow. Whilst assuming all dissolution comes from the groove results in an over estimate of the mass transfer coefficient, including the total area of the rod will result in an average value that that is an underestimate of the corrosion rate in the groove. It would be expected that the mass transfer coefficient calculated from Eq.(3.14) would lie in somewhere between the other two values. Clearly this is not the case. The reason could be the assumption that the shape of dissolved MgO is a cylindrical trough. When using Eq.(3.4) to calculate the mass transfer coefficient, the width and depth of erosion profile on cross section are measured and the reaction area is calculated by assuming the erosion profile on the cross section is ellipse. If using the assumption of cylindrical trough to calculate the reaction area and used in Eq.(3.4), the mass transfer coefficients could be

calculated as $8.1*10^{-6}$m/s, $8.3*10^{-6}$m/s, $8.4*10^{-6}$m/s and $7.7*10^{-6}$ms/ for experimental temperature 1650^{o}C, 1625^{o}C, 1600^{o}C and 1575^{o}C respectively. Except the experimental temperature at 1650^{o}C, the rest of data points are greater than the mass transfer coefficient calculated from Eq.(3.14).

3.2.6 Conclusion:

The corrosion of MgO refractory in CaO- Al_2O_3 slag system has been studied at 1575^{o}C-1650^{o}C from 30min to 150min. The change of MgO concentration with time was observed. The Hrma model, based on assuming that surface tension driven mass transfer controls the dissolution process and a simplified geometry and flow field, provided a reasonable estimate of the rate of MgO dissolution for direct dissolution. The effective mass transfer coefficients were calculated and found to be dependent on temperature. The activation energy for the dissolution process was obtained as 120kJ/mol, which supports that the whole process is controlled by diffusion. The effective mass transfer coefficient calculated from kinetic analysis of change in slag composition with total reaction area and with only groove surface area are calculated. The actual mass transfer coefficient should be between those two mass transfer coefficients.

Chapter 4 Numerical Modeling

4.1. Introduction:

Slag line corrosion of refractory has been quantitatively studied by Hrma[40] and Tsotridis [41]. In Hrma's study, he quantitatively correlated the phenomenon of slag line corrosion with the surface tension, he did not present a rigorous solution of the flow and concentration fields, which are likely to be important parameters in understanding the corrosion mechanisms.

Tsotridis[41] presented a numerical algorithm to simulate of the flow and concentration fields. He was able to calculate the corrosion rate based on the concentration field. In developing this model Tsotridis made several simplifying assumptions. The first assumption is, that, the shape of eroded wall has no effect on the flow pattern, hence, the shape of the eroded wall has no effect on the subsequent corrosion rate. Therefore, Tsotridis used a constant rectangular physical domain, and during the computation, the domain remained unchanged. In the real case, as the dissolvable wall is eroded by the fluid, the shape of the wall will change, and hence the erosion profile has an effect on the flow pattern. The second assumption is that, the shape of the liquid top surface is flat, which means the wetting behavior between the liquid and the solid is not important in the corrosion process. From the experimental observations, the upper surface of the liquid is not flat. A meniscus shape can be observed at the deformed top surface. In the present work, the relative importance of those two assumptions have been investigated.

In this study, an algorithm has been developed to predict the slag line erosion rate subject to the Marangoni effect. A cylindrical crucible filled with molten slag is used as the physical domain, see Fig 4.1. Flow of the molten slag is caused by different forces: (1) density driven buoyancy force. When the MgO rod is dissolved into the melt, a concentration gradient of the solute in the melt is set up near the rod, which changes the melt density adjacent to the rod. (2) surface tension driving force. The presence of dissolved species in the melt creates a surface tension gradient at the free surface resulting in surface flow, known as Marangoni flow. The relative magnitude and the interaction between the two types of flow determine the rate of corrosion and the shape of the corrosion profile. The corrosion is analyzed in terms of the Grashof number (ratio of buoyancy to viscous forces) and the Marangoni number (ratio of surface tension to viscous forces).

In the current work the geometry of the solution domain is regularized using a coordinate transformation method. Because the corrosion profile is irregular, the physical domain becomes irregular as time progresses. The coordinate mapping technique is used to transfer the irregular physical domain into a regular rectangular computational domain. The field equations are expressed in the terms of the stream function and vorticity. All spatial derivatives are discretized using the second-order finite difference discretization method. Time derivatives are discretized using a first-order one step implicit method.

4.2 Mathematical Formulation:

Consider the wall of a cylindrical crucible containing slag as shown in Figure 4.1. The upper surface of the slag is described by z=hz(r). The left side rod is dissolvable into the liquid, O is the point of origin. The motion of the liquid is driven by variations of surface tension due to the solid concentration differences in the liquid. The shape of the dissolved MgO rod can be describe by function h(z,t), which is a function of time, and can be determined by concentration gradient in r-direction at the wall. The flow and the concentration fields are determined by solving the Navier-Stokes equations coupled with the mass diffusion equations. All equations are mutually dependent since the surface tension is a function of concentration.

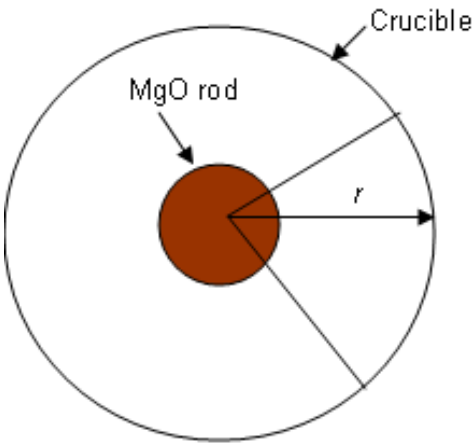

A. Top view of physical domain

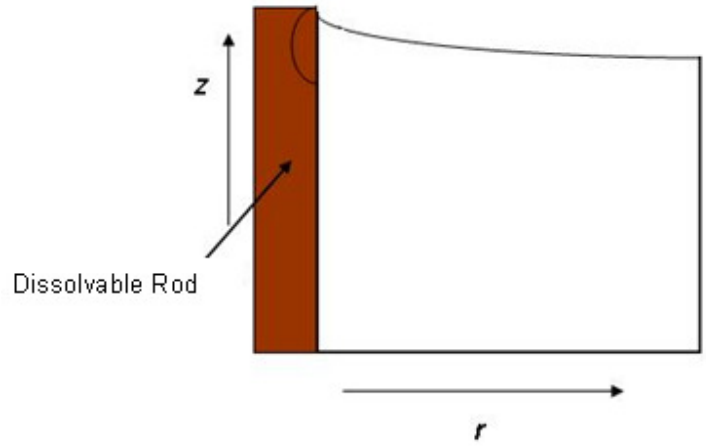

B. Side view of physical domain, from the center line to the right.

Figure 4.1 Sketch of physical domain

The governing equations are:

Equation of continuity:

$$\frac{1}{r'}\frac{\partial(r'u_r')}{\partial r'}+\frac{\partial u_z'}{\partial z'}=0 \tag{4.1}$$

Equation of motion:

in *r* direction

$$\frac{\partial u_r'}{\partial t'} + u_r' \frac{\partial u_r'}{\partial r'} + u_z' \frac{\partial u_r'}{\partial z'} = -\frac{1}{\rho'} \frac{\partial p'}{\partial r'} + \upsilon' [\frac{\partial^2 u_r'}{\partial r'^2} + \frac{\partial^2 u_r'}{\partial z'^2}] \tag{4.2}$$

in *z* direction:

$$\frac{\partial u_z'}{\partial t'} + u_r' \frac{\partial u_z'}{\partial r'} + u_z' \frac{\partial u_z'}{\partial z'} = -\frac{1}{\rho'} \frac{\partial p'}{\partial z'} + \upsilon' [\frac{\partial^2 u_z'}{\partial r'^2} + \frac{\partial^2 u_z'}{\partial z'^2}] - \frac{g'}{\rho_o'} (\frac{\partial \rho'}{\partial c'}) c' \tag{4.3}$$

Diffusion equation based on Fick's law:

$$\frac{\partial c'}{\partial t'} + \frac{\partial}{\partial r'} (u_r' c') + \frac{\partial}{\partial z'} (u_z' c') = D' [\frac{\partial^2 c'}{\partial r'^2} + \frac{\partial^2 c'}{\partial z'^2}] \tag{4.4}$$

Where ' represents dimensional quantities, ρ is the density, ρ_o is a reference density, υ is the kinematic viscosity, P is pressure, *t* is time, u_r is velocity in the r-direction, u_z is the velocity in the z-direction, c is the bulk concentration of dissolved solid in the melt, D is the diffusion coefficient. The last term on the right-hand side of Eq.(4.3) represents the buoyancy force, which is caused by density variations due to concentration gradient within the liquid.

The basic assumptions are as follows:

(1) The flow is laminar.

(2) Density (except in the buoyancy term), viscosity and diffusion coefficient are constant within the variation of concentration.

(3) The dissolution process is diffusion controled. The rate of dissolved species transfer through solid-liquid interface is much faster than the dissolved species transfer from the

interface to the bulk liquid. So, at the solid-liquid interface, the concentration of the solid material always remains at saturation.

(5) The whole system remains isothermal. Therefore the temperature effect can be neglected.

The boundary conditions required to complete the problem have to express the following physical conditions:

(1) Velocity components are zero at the solid wall:

$u_r' = u_z' = 0$ at the side wall and bottom wall

(2) There is no mass diffusion through the left side centre line, bottom wall and top surface:

$\frac{\partial c'}{\partial r'} = 0$ at the left rod

$\frac{\partial c'}{\partial r'} = 0$ at the bottom and top surface

(3) At the free surface, the kinematic boundary condition is:

$$u_r' \frac{\partial hz}{\partial r} - u_z' = 0 \tag{4.5}$$

the dynamic boundary condition at normal direction:

$$\mu'\left(\frac{1-h_r^2}{N^2}\right)\left(\frac{\partial u_r'}{\partial z'} + \frac{\partial u_z'}{\partial r'}\right) + 2\mu' \frac{h_r}{N}\left(2\frac{\partial u_z'}{\partial z'} + \frac{\partial u_r'}{\partial r'}\right) = -\gamma'\left(\frac{\partial c'}{\partial r'} + hz\frac{\partial c'}{\partial z'}\right) \tag{4.6}$$

where μ' is the viscosity and γ' is the surface tension gradient, $= \frac{\partial \sigma'}{\partial c'}$, $h_r = \frac{\partial h}{\partial r}$.

(4) At the liquid-solid interface, the concentration of dissolved components remain saturated.

The governing equations (4.1)-(4.4) and the boundary conditions are nondimensionalized by introducing the following relationships:

$$r=\frac{r'}{L'},\ z=\frac{z'}{L'},\ u=\frac{u'}{u*},\ v=\frac{v'}{u*},\ t=\frac{t'}{t*},\ c=\frac{c'}{\Delta c'}$$

where L' is the characteristic length, characteristic velocity $u*=\frac{\gamma'\Delta c'}{\mu'}$, $\Delta c'=c_s'-c_b'$, c_s' is the saturated concentration, c_b' is the concentration in the bulk, characteristic time $t*=\frac{L'}{u*}$.

The nondimensional equations of continuity, momentum, and diffusion are:

Equation of continuity:

$$\frac{1}{r}\frac{\partial(ru_r)}{\partial r}+\frac{\partial u_z}{\partial z}=0 \tag{4.7}$$

where u_r is dimensionless velocity in the r direction, u_z is dimensionless velocity in z direction,

Equation of motion:

equation of motion in r direction

$$\mathrm{Re}(\frac{\partial u_r}{\partial t}+u_r\frac{\partial u_r}{\partial r}+u_z\frac{\partial u_z}{\partial z})=-\frac{\partial p}{\partial r}+[\frac{\partial}{\partial r}(\frac{1}{r}\frac{\partial}{\partial r}(u_r r)+\frac{\partial^2 u_z}{\partial z^2}] \tag{4.8}$$

equation in z direction:

$$\mathrm{Re}(\frac{\partial u_z}{\partial t}+u_r\frac{\partial u_z}{\partial r}+u_z\frac{\partial u_z}{\partial z})=-\frac{\partial p}{\partial z}+[\frac{1}{r}\frac{\partial}{\partial r}(r\frac{\partial u_z}{\partial r})+\frac{\partial^2 u_z}{\partial z^2}]+Grc\frac{c}{\mathrm{Re}} \tag{4.9}$$

Diffusion equation based on Fick's law:

$$Ma(\frac{\partial c}{\partial t}+\frac{\partial}{\partial r}(u_r c)+\frac{\partial}{\partial z}(u_z c))=\frac{1}{r}\frac{\partial}{\partial r}(r\frac{\partial c}{\partial r})+\frac{\partial^2 c}{\partial z^2} \tag{4.10}$$

where

$$Gr_c=\frac{\beta_c g' L'^3(c_s'-c_b')}{\upsilon'^2},\ \beta_c=-\frac{1}{\rho'}(\frac{\partial \rho'}{\partial c'}),\ \mathrm{Re}=\frac{u^* L'}{\upsilon'},\ Ma=\frac{\gamma'\Delta c' L'}{D'\mu'}$$

Grc is the Grashof number for concentration gradients, β_c is the concentration expansion coefficient, Re is the Reynolds number and Ma is the Marangoni number.

The boundary conditions:

(1) $u_r=u_z=0$ at the side wall and bottom wall

(2) $\frac{\partial c}{\partial r}=0$ at the side wall, $\frac{\partial c}{\partial z}=0$ at the bottom (4.11)

(3) the kinematic boundary condition:

$$u_r\frac{\partial hz}{\partial r}-u_z=0 \tag{4.12}$$

dynamic boundary condition at normal direction:

$$(\frac{1-(\frac{\partial hz}{\partial r})^2}{N})(\frac{\partial u_r}{\partial z}+\frac{\partial u_z}{\partial r})+\frac{\partial hz}{\partial r}\frac{1}{N}(2\frac{\partial u_z}{\partial z}+\frac{\partial u_r}{\partial r})=-(\frac{\partial c}{\partial r}+\frac{\partial hz}{\partial r}\frac{\partial c}{\partial z}) \tag{4.13}$$

(4) At the dissolvable liquid-solid interface, the concentration of dissolved components remains saturated: Cs=1.0 at the interface.

4.3 Numerical Methods

4.3.1 Stream Function and Vorticity Formulation

Introducing the stream function and, the vorticity technique. Stream functions are defined as:

$$u_r = \frac{1}{r}\frac{\partial \psi}{\partial z},\ u_z = -\frac{1}{r}\frac{\partial \psi}{\partial r} \tag{4.14}$$

The dimensionless vorticity is defined as:

$$\Omega = \frac{\partial u}{\partial y} - \frac{\partial v}{\partial x} = -\frac{1}{r}[\frac{\partial^2 \psi}{\partial r^2} - \frac{1}{r}\frac{\partial \psi}{\partial r} + \frac{\partial^2 \psi}{\partial z^2}] \tag{4.15}$$

Eliminating the pressure term by cross differentiating Eq.(4.3), and Eq.(4.4), and using the relationship for the stream function and vorticity , the following equation is formed:

$$\mathrm{Re}(\frac{\partial \Omega}{\partial t} + \frac{1}{r}\frac{\partial \psi}{\partial z}\frac{\partial \Omega}{\partial r} - \frac{1}{r}\frac{\partial \psi}{\partial z}\frac{\Omega}{r} - \frac{1}{r}\frac{\partial \psi}{\partial r}\frac{\partial \Omega}{\partial z}) = (\frac{\partial^2 \Omega}{\partial r^2} + \frac{1}{r}\frac{\partial \Omega}{\partial r} - \frac{\Omega}{r}) + \frac{\partial^2 \Omega}{\partial z^2} + \frac{Grc}{\mathrm{Re}}\frac{\partial c}{\partial r} \tag{4.16}$$

$$Ma(\frac{\partial c}{\partial t} + \frac{1}{r}(\frac{\partial \psi}{\partial z}\frac{\partial c}{\partial r} - \frac{\partial \psi}{\partial r}\frac{\partial c}{\partial z}) = \frac{\partial^2 c}{\partial r^2} + \frac{1}{r}\frac{\partial c}{\partial r} + \frac{\partial^2 c}{\partial z^2} \tag{4.17}$$

The boundary condition for Eq.(4.15)~Eq.(4.17) are:

(1) $\psi = 0$ for all boundaries (4.18)

(2) C=*Cs* at the left rod. (4.19)

(3) $\frac{\partial c}{\partial z} = 0$ for the bottom wall and top surface (4.20)

(4) $\frac{\partial c}{\partial r} = 0$ for the right wall. (4.21)

(5) $\Omega = -\nabla^2\psi$ for the left rod, right and bottom wall. (4.22)

(6) $\frac{1-(\frac{\partial hz}{\partial r})^2}{N}(-2\frac{1}{r}\frac{\partial^2\psi}{\partial r^2}+\frac{1}{r^2}\frac{\partial\psi}{\partial r}-\Omega)+2\frac{\partial hz}{\partial r}\frac{1}{N}(-2\frac{\partial^2\psi}{\partial r\partial z}\frac{1}{r}+\frac{\partial\psi}{\partial z}\frac{1}{r^2})=-(\frac{\partial c}{\partial r}+\frac{\partial hz}{\partial r}\frac{\partial c}{\partial z})$ solve Ω at the top surface. (4.23)

where $N=\sqrt{1+(\frac{\partial hz}{\partial r})^2}$

4.3.2 Coordinate Transformation

The flow problem has to be solved numerically on an irregular, time-dependent solution domain. The transformation must apply to transfer the irregular physical domain into a regular computational domain. Figure 4.2 shows the physical domain and the computational domain before and after coordinate transformation. The new coordinates (ζ, η) are defined as:

$$\zeta=\frac{r_o-r}{H(z,t)},\eta=\frac{z}{Hz(r)} \quad (4.24)$$

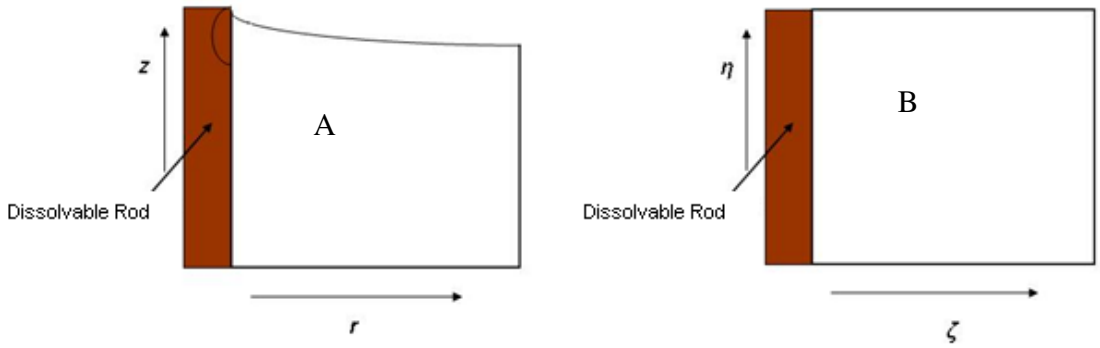

Figure 4.2 Sketch of the model problem: (A) Side view of physical domain

(B) computational domin

This coordinates map the domain onto a fixed regular domain in the computational (ζ, η) plane permitting use of standard finite-difference discretization techniques for spatial derivates. The mpping function *h(z,t)* is unknown and has to be calculated by the mass conservation, which can be calculated as

$$h = \sqrt{hi^2 - E \times \Delta t \times hi \times 2} \tag{4.25}$$

where Δt is length of the time step, *hi* is the *h* from the previous time step, E is defined as dissolution rate, which can be calculated as :

$$E = -C_s^{\,2} \frac{\partial c}{\partial r} \frac{1}{Ma} \tag{4.26}$$

The governing equations written in terms of ψ and Ω take the following forms:

$$\Omega + \nabla^2 \psi / (x_0 - \xi h) = 0 \tag{4.27}$$

$$\begin{aligned} &\mathrm{Re}[-\frac{\partial \Omega}{\partial \xi}\frac{\partial h}{\partial t}\frac{\xi}{h} + \frac{\partial \Omega}{\partial t} - \frac{1}{(x_0 - \xi h)hh_x}(\frac{\xi\eta}{hh_z}\frac{\partial h}{\partial \eta}\frac{\partial h_z}{\partial \xi} - 1)(\frac{\partial \Omega}{\partial \eta}\frac{\partial \psi}{\partial \xi} - \frac{\partial \psi}{\partial \eta}\frac{\partial \Omega}{\partial \xi}) \\ &+ \frac{\Omega}{(x_0 - \xi h)^2 h_z}(\frac{\partial \psi}{\partial \xi}\frac{\xi}{h_z}\frac{\partial h}{\partial \eta} - \frac{\partial \psi}{\partial \eta})] = \nabla^2 \Omega + \frac{Grc}{\mathrm{Re}\, h}(\frac{\partial c}{\partial \xi} - \frac{\partial c}{\partial \eta}\frac{\partial h_x}{\partial \xi}\frac{\xi}{h_z}) \end{aligned} \tag{4.28}$$

$$\begin{aligned} &Ma[-\frac{\partial c}{\partial \xi}\frac{\partial h}{\partial t}\frac{\xi}{h} + \frac{\partial c}{\partial t} - \frac{1}{(x_0 - \xi h)hh_z}(\frac{\xi\eta}{hh_z}\frac{\partial h}{\partial \eta}\frac{\partial h_z}{\partial \xi} - 1)(\frac{\partial c}{\partial \eta}\frac{\partial \psi}{\partial \xi} - \frac{\partial \psi}{\partial \eta}\frac{\partial c}{\partial \xi})] \\ &= \nabla^2 c + \frac{2}{(x_0 - \xi h)h}(\frac{\partial c}{\partial \xi} - \frac{\partial c}{\partial \eta}\frac{\partial hz}{\partial \xi}\frac{\eta}{h}) \end{aligned} \tag{4.29}$$

$$\begin{aligned} \nabla^2 = &\frac{1}{h^2}\frac{\partial^2}{\partial \xi^2}(1 + \frac{\xi^2}{h_z^{\,2}}(\frac{\partial h}{\partial \eta})^2) - \frac{2}{h^2 h_x^{\,2}}\frac{\partial^2}{\partial \xi \partial \eta}(\frac{\eta}{h}\frac{\partial h_z}{\partial \xi} + \frac{\xi}{hz}\frac{\partial h}{\partial \eta}) + \frac{1}{h_x^{\,2}}\frac{\partial^2}{\partial \eta^2}(1 + \frac{\eta^2}{h^2}(\frac{\partial h_z}{\partial \xi})^2) \\ &+ \frac{2}{h^2 h_z^{\,2}}(\frac{\partial}{\partial \eta}(\frac{\partial h_x}{\partial \xi})^2\eta + \frac{\partial}{\partial \xi}(\frac{\partial h}{\partial \eta})^2\xi) - \frac{1}{hh_z}(\frac{\partial}{\partial \eta}\frac{\partial^2 h_z}{\partial \xi^2}\frac{\eta}{h} + \frac{\partial}{\partial \xi}\frac{\partial^2 h}{\partial \eta^2}\frac{\xi}{h_x}) \\ &- \frac{1}{(x_0 - \xi h)h}(\frac{\partial}{\partial \xi} - \frac{\partial}{\partial \eta}\frac{\partial h_z}{\partial \xi}\frac{\eta}{h}) \end{aligned}$$

where

The boundary conditions are:

(1) $\psi = 0$ for all the walls and top surface. (4.30)

(2) $\Omega+\nabla^2\psi/(x_0-\xi h)=0$ for the left rod and right wall (4.31)

(3) $\Omega+\nabla^2\psi=0$ for the bottom walls (4.32)

$$\frac{1}{\sqrt{1+(\frac{\partial h_z}{\partial\xi})^2\frac{1}{h^2}}}((-\Omega+\frac{\Omega}{hc}(\frac{\partial h_z}{\partial\xi})^2)+\frac{2}{(x0-\xi h)h}(\frac{\partial\psi}{\partial\xi}(-\frac{1}{x0-\xi h}+\frac{1}{(x0-\xi h)h^2}(\frac{\partial h_z}{\partial\xi})^2$$

$$+\frac{2}{h^2h_z}\frac{\partial h}{\partial\xi}\frac{\partial h}{\partial\eta}+\frac{\xi}{hh_z(x0-\xi h)}\frac{\partial h_z}{\partial\xi}\frac{\partial h}{\partial\eta}+\frac{1}{h}\frac{\partial^2\psi}{\partial\xi^2}(\frac{1}{h^2}(\frac{\partial h_z}{\partial\xi})^2-1+\frac{\partial h_z}{\partial\xi}\frac{\partial h}{\partial\eta}\frac{2\xi}{hh_x})+ \quad (4.33)$$

$$\frac{\partial\psi}{\partial\eta}\frac{1}{hh_z}(\frac{\partial^2h_z}{\partial\xi^2}+\frac{2}{h^2h_x}(\frac{\partial h_z}{\partial\xi})^4-(\frac{\partial h_z}{\partial\xi})^3\frac{1}{(x0-\xi h)h}-(\frac{\partial h_z}{\partial\xi})^2\frac{\partial^2h_z}{\partial\xi^2}\frac{1}{h^2})+\frac{\partial^2\psi}{\partial\eta^2}(\frac{\partial h_z}{\partial\xi})^2\frac{1}{hh_z{}^2}$$

$$(1+(\frac{\partial h_z}{\partial\xi})^2\frac{1}{h^2})+\frac{\partial^2\psi}{\partial\xi\partial\eta}\frac{2}{h^2h_z}(\frac{\partial h_z}{\partial\xi})^2(-\frac{\partial h_z}{\partial\xi}\frac{1}{h}-\frac{\partial h}{\partial\eta}\frac{\xi}{h_z}))+\frac{\partial c}{\partial\xi}\frac{1}{h}(-1+\frac{\partial h_z}{\partial\xi}\frac{\partial h}{\partial\eta}\frac{\xi}{h_zh})=0$$

(5) $-\frac{\partial c}{\partial\xi}(\frac{\partial h_z}{\partial\xi}\frac{1}{h^2}+\frac{\xi}{hh_z}\frac{\partial h}{\partial\eta})+\frac{\partial c}{\partial\eta}\frac{1}{h_z}(1+\frac{\xi}{h}\frac{\partial h}{\partial\eta})=0$ for concentration at top and bottom boundaries (4.34)

(6) $-\frac{\partial c}{\partial\xi}+\frac{\partial c}{\partial\eta}\frac{\eta}{h_z}\frac{\partial h}{\partial\eta}=0$ for the concentration at the left rod (4.35)

4.3.3 One-Step Implicit Method:

A one-step implicit method is used to solve the problem. It is assumed that all quantities are known at time t=nΔt, and their values at t=(n+1)Δt are sought. The flow field and concentration equations are solved at the t=(n+1)Δt keeping the location of the interface unchanged at the inner iteration. After the solution of the flow field and concentration are obtained, the new interface location is calculated by using Eq.(4.25) at the outer iteration. The complete solution procedure involves iterations between the inner and the outer problems until all the conditions are satisfied with the desired accuracy. A flow chart of the calculation procedure is shown in Figure 4.3.

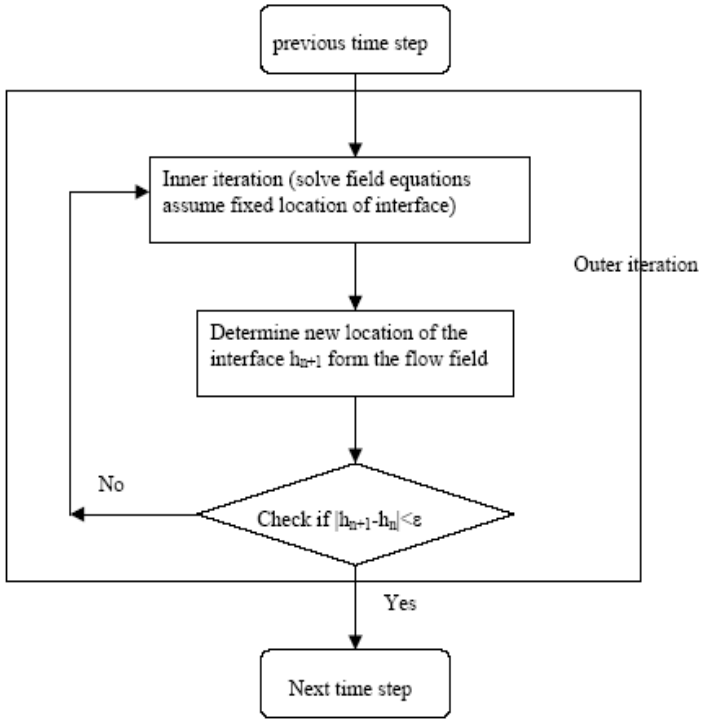

Figure 4.3. Flow chart for the proposed algorithm

The Inner Problem:

The field equations are written at time t=(n+1) Δt in the form:

$$\Omega^{n+1} + \nabla^2 \psi^{n+1} / (x_0 - \xi h^{n+1}) = 0 \tag{4.36}$$

$$\begin{aligned} &\mathrm{Re}[\frac{\Omega^{n+1} - \Omega^n}{\Delta t} - \frac{\partial \Omega^{n+1}}{\partial \xi}\frac{\partial h^{n+1}}{\partial t}\frac{\xi}{h} - \frac{1}{(x_0 - \xi h^{n+1})h^{n+1}h_z}(\frac{\xi\eta}{h^{n+1}h_z}\frac{\partial h^{n+1}}{\partial \eta}\frac{\partial h_x}{\partial \xi} - 1) \\ &(\frac{\partial \Omega^{n+1}}{\partial \eta}\frac{\partial \psi^{n+1}}{\partial \xi} - \frac{\partial \psi^{n+1}}{\partial \eta}\frac{\partial \Omega^{n+1}}{\partial \xi}) + \frac{\Omega^{n+1}}{(x_0 - \xi h^{n+1})^2 h_z}(\frac{\partial \psi^{n+1}}{\partial \xi}\frac{\xi}{h_z}\frac{\partial h^{n+1}}{\partial \eta} - \frac{\partial \psi^{n+1}}{\partial \eta})] \\ &= \nabla^2 \Omega^{n+1} + \frac{Grc}{\mathrm{Re}\, h^{n+1}}(\frac{\partial c^{n+1}}{\partial \xi} - \frac{\partial c^{n+1}}{\partial \eta}\frac{\partial h_z}{\partial \xi}\frac{\xi}{h_z}) \end{aligned} \tag{4.37}$$

Where $\frac{\partial \Omega}{\partial t}$ has been replaced by backward, first-order finite-difference approximation. In the above, superscripts n and n+1 refer to the time steps, and h^{n+1} is known from the previous outer iteration (or from the previous time step in the cast of the first outer iteration). The diffusion equation has the similar form as Eq.(4.37) with $\frac{\partial \Omega}{\partial t}$ is replaced by $\frac{\partial c}{\partial t}$ and Re is replaced by Ma.

A rectangular computational grid of size $\Delta\xi$, $\Delta\eta$ in the directions of ξ, η is considered, with grid lines parallel to the ξ and η axes and such grid fits exactly the geometry of the computational domain, with the side and bottom walls and the interfaces as certain grid lines. Around a typical interior grid point (ξ_o, η_o) we adopt the convention that quantities at (ξ_o, η_o) and eight neighboring points are denoted by subscripts 0, 1, …, 8 as shown in Figure 4.4. Equations are written at each interior grid point and the spatial derivatives are approximated by using second-order finite-difference method. Appendix (1) gives the detailed coefficient calculation for each interior grid point.

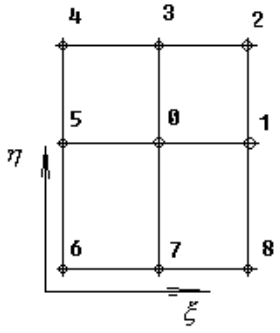

Figure 4.4. Sketch of a typical computational module used in the interior of the solution domain

The boundary condition for Eq.(4.27), (4.28) and (4.29) are given by (4.30)~(4.35). For (4.30) the values of ψ^{n+1} are known at all grid points on the solid walls. For (4.31), a boundary condition for Ω^{n+1} is required at the grid points on the left rod, right wall and bottom. We use a second-order approximation for the left rod and right wall:

$$\Omega_w^{n+1} = (\psi_{i+1}^{n+1} - 8\psi_i^{n+1})/(2\Delta\xi^2) \tag{4.38}$$

where subscript w refers to the rod or wall values, subscript *i* refers to the internal grid point most immediate to w and subscript (*i*+1) refers to the next grid point in the same direction. A similar formula for the bottom of the wall has the form:

$$\Omega_w^{n+1} = (\psi_{i+1}^{n+1} - 8\psi_i^{n+1})/(2\Delta\eta^2) \tag{4.39}$$

the boundary condition for the vorticity at the top surface is obtained from Eq.(4.33). In this equation $\psi_{i+1}^{n+1}, \frac{\partial\psi^{n+1}}{\partial\xi}, \frac{\partial^2\psi^{n+1}}{\partial\xi^2}, \frac{\partial\psi^{n+1}}{\partial\eta}, \frac{\partial^2\psi^{n+1}}{\partial\eta^2}, h^{n+1}, \frac{\partial h^{n+1}}{\partial\eta}, \frac{\partial^2 h^{n+1}}{\partial\eta^2}, \frac{\partial c^{n+1}}{\partial\xi}$ are considered to be known, $\frac{\partial h^{n+1}}{\partial\eta}, \frac{\partial^2 h^{n+1}}{\partial\eta^2}$ are evaluated using standard backward-difference approximations based on values of h^{n+1} from the previous outer iteration (or from the previous time step in the case of the first iteration). Concentration gradient $\frac{\partial c^{n+1}}{\partial\xi}$ is evaluated using standard central-difference approximation. $\frac{\partial\psi^{n+1}}{\partial\eta}, \frac{\partial^2\psi^{n+1}}{\partial\eta^2}$ are determined using one-sided difference approximation. All spatial discretization formulae are second-order accurate.

For the concentration equation, values c^{n+1} are known at the right wall. At the remaining three boundaries, c^{n+1} is determined from the discretized boundary conditions Eq.(4.34) and Eq.(4.35) using second-order finite-difference formula.

Assuming the location of the interface h^{n+1} and the value of vorticity Ω^{n+1} at the interface are known, the problem Eq.(4.27)-(4.29) supplemented by the concentration equation and the boundary conditions described above, can be solved either directly or iteratively. The present study, uses an iterative method, based on the Gauss-Seidel procedure. Values from the last outer iteration (or the previous time step in the case of the first outer iteration) are used as an initial guess for the field variables. The systematic iterative procedure between the various equations consisted of performing one complete Gauss-Seidel iteration of Eq.(4.27), followed by a similar iteration of Eq.(4.28) and then a complete iteration of the concentration equation Eq. (4.29), followed by recalculation of the boundary values of Eq.(4.30)~Eq.(4.35). The iterations were performed until the convergence criteria $\left|\mathrm{Re}\, s_{q(j+1)}\right| < \varepsilon_1$ ($\varepsilon_1 = 2\times10^{-5}$) were satisfied at all grid points. In the above, Res denotes residuum of any of the discretized field equations, subscript q stands for any of the flow quantities, and subscript *j* denotes the inner iteration number.

The Outer Problem:

Evaluation of the new location of the interface:

The equation of the new location calculation involves the concentration gradient at the boundary, can be solved from Eq.(4.25) and Eq.(4.26):

$$h_{i+1}^{n+1} = \sqrt{(h_{i+1}^{n})^2 - C_s{}^2 \frac{\partial c_{i+1}^{n+1}}{\partial \xi} \frac{1}{Ma} \times \Delta t \times 2} \tag{4.40}$$

where subscript n denotes the outer iteration, i denote the inner iteration. h_{i+1}^{n+1} represents the most recent approximation of h at time $t = \Delta t(n+1)$, and h_{i+1}^{n} denotes h from previous time step $t = \Delta t * n$. For a sufficiently small time step a good approximation h_{i+1}^{n} of the interface is always available. $\frac{\partial c_{i+1}^{n+1}}{\partial \xi}$ is discretized using standard backward difference formula. Problem Eq.(4.40) can be solved directly. Numerical solution of Eq.(4.40) is very efficient and the required computational time is negligible, compare with the time required to determine solution of the inner problem. Typically, one or two outer iterations would reduce the error to several orders of magnitude less than the error accepted in the solution of the inner problem.

A complete iterative cycle consists of determination of the flow field (inner problem) followed by determination of the new approximation for Eq.(4.40). Such iterations are carried out until the convergence criteria $\left|h_{i+1}^{n+1} - h_i^{n+1}\right| < \varepsilon_2$ ($\varepsilon_2 = 10^{-14}$) and $\left|\mathrm{Re}\, s_{q(j+1)}\right| < \varepsilon_1$ ($\varepsilon_1 = 2 \times 10^{-5}$) are satisfied at all grid points along the interface.

4.4 Conclusion:

An algorithm for analysis of unsteady Marangoni convection in refractory slag line dissolution has been developed. The algorithm solves the unsteady-state boundary problem for the Navier-Stokes and diffusion equations. The unknown time-dependent

solution domain is mapped onto a fixed rectangular computational domain. A one step implicit method is used to solve the equations; inner loop resolved field equations and outer loop resolved the mapping function. When both inner loop and outer loop are satisfied with the desired accuracy, the complete solution is achieved.

Chapter 5 Performance of the Algorithm and Comparison of Numerical with Experimental Results

5.1 Introduction

In this chapter, the comparison of model results with experimental results will be carried out. This will validate and determine the accuracy of the numerical model. Then following with the performance of the algorithm, different cases will be studied with different conditions.

5.2 Comparing of numerical and experimental results

In order to examine the validity of the numerical model, comparison with experimental data is essential. Numerical results have been obtained from the cases of moving and curved upper boundary. The dimensionless numbers used are: $Ma=1.6*10^5$, Re=13, Grc=200, based on appropriate physical data for the slag as shown in Table 5.1. Comparison of the experimental data with numerical results can be analyzed in three of measureable parameters: maximum erosion distance, volume of eroded solid and shape of eroded profile at different times. Maximum erosion distance is the priority indication of refractory failure. The volume of eroded solid is critical to justify the performance of the model. The shape of eroded profile indicates the accuracy of the numerical model.

Figure 5.1 presents the maximum corrosion distance as a function of time, by different cases, and compares this with experimental data. It shows that in the case for a constant boundary and flat boundary, the difference between numerical results and the experimental data is 80~100% in the time range show in the figure. The difference for the cases of the moving boundary with flat boundary is 30~50% in the time range. The difference for the cases of moving and curved boundary with constant flat boundary is about 10~40%. The case of moving and curved boundary is the closest to the experimental data.

Table 5.1 Physical Properties used to calculate the dimensionless numbers

Viscosity (Pa.S)[7]	Density (kg/m^3)[7]	Diffusion coefficient (m^2/s)[7]	Surface tension gradient (mN/m) [7]	Characteristic Length(m)
0.43	2.82×10^{3}	1.02×10^{-8}	200	0.03

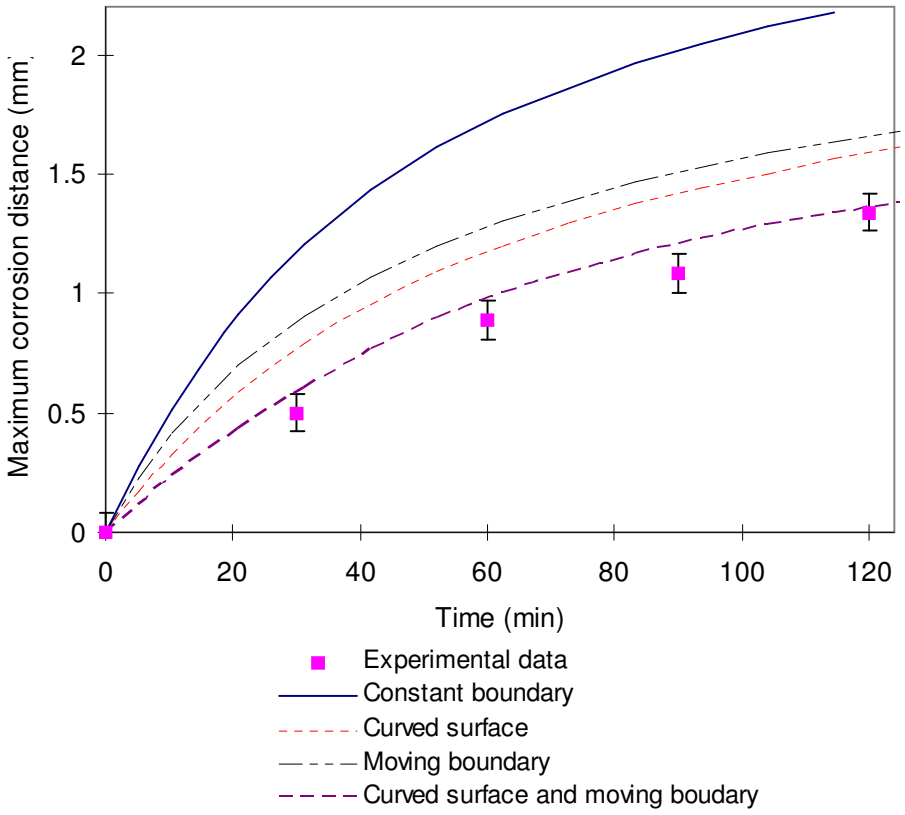

Figure 5.1 Comparing of maximum corrosion distance

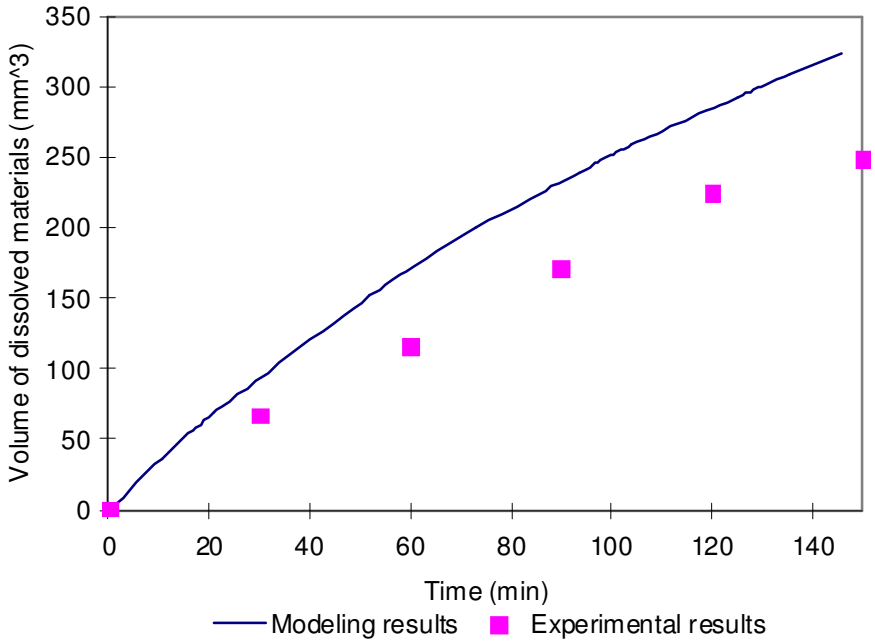

Figure 5.2 Comparing the volume of dissolved materials

The corroded solid volume obtained numerically for the case of moving and curved boundary compared with the experimental results is shown in Figure 5.2. The volume of eroded materials obtained numerically is about 20~30% higher than the experimental results.

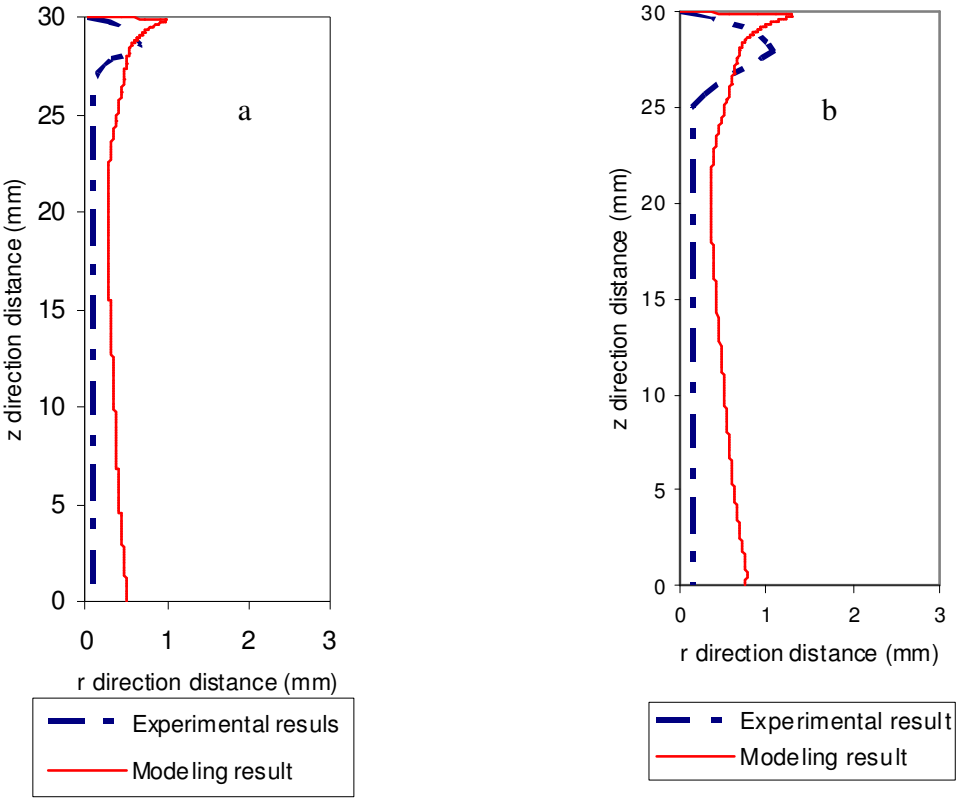

Figure 5.3 Comparing the calculated corrosion profiles with experimental data

(a) Shape of corrosion profile at 60 min

(b) Shape of corrosion profile at 90 min

Figure 5.3(a) (b) shows is the numerical and experimental profiles of eroded rod after 60 and 90 minutes. There are two major deviations: (1) The numerical results show a shallow groove at the top surface. The maximum erosion appears very close to the top surface. The experimental results show a smooth curve at the top. This deviation between the numerical results and experimental data can be attributed to the following: (a) the model assumes, that the top surface is fixed. Therefore at the top surface, the motion in

the vertical direction is neglected. (b) Since the model assumes a fixed top surface, it can only simulate the erosion profile under the initial top surface. In reality when the refractory rod is eroded, the wetting behavior between the solid and liquid changes, which will generate flow climb up the refractory rod. This flow will dissolve the refractory above the initial surface, which the current model could not predict. (2) The model results show greater erosion at the lower rod. The dissolution of the lower part of the rod is controlled by the Reynolds number and Grashof number. The accuracy of those numbers is essential to accurately predict the erosion profile at the lower part. The accuracy of slag properties at high temperature is limited. For example, the data for slag diffusion coefficient can vary by one order of magnitude. The uncertainty in slag properties has an effect on the values of the dimensionless numbers used with the numerical algorithm.

5.3 Sensitivity Study

As a part of comparison of model results with experimental results, a sensitivity study was performed to analyze the effects of Marangoni number, Reynolds number and Grashof number respectively on the erosion rate.

5.3.1 Marangoni number:

The effect of the Marangoni number can be evaluated by keeping the other variables constant and varying the Marangoni number. This affects both erosion rate and erosion profile. Marangoni number is defined as $Ma = \frac{\gamma' \Delta c' L'}{D' \mu'}$, Reynolds number is defined

$\mathrm{Re} = \frac{\gamma' \Delta c' L'}{\upsilon' \mu'}$, and Grashof number is defined as $Gr_c = \frac{\beta_c g' L'^3 (c_s' - c_b')}{\upsilon'^2}$. To vary the Marangoni number while keeping the Reynolds number and the Grashof number as constant, diffusion coefficient D' has to be varied. By increasing diffusion coefficient, Ma decreases, the erosion distance decreases, and the volume of dissolved material decreases as well. As the diffusion coefficient varies $\pm 20\%$, the erosion distance varies by $\pm 0.76\%$, the volume of dissolved material varies by $\pm 12.4\%$.

5.3.2 Grashof number:

The effect of the Grashof number can be evaluated by keeping Marangoni number and Reynolds number constant and varying the Grashof number. In this case, β_c, the concentration expansion coefficient needs to be varied. Positive concentration expansion coefficient means by increasing the concentration of dissolution material, bulk density decreases. Decreasing the bulk density creates buoyancy flow and the direction of the flow is in the opposite direction to Marangoni flow. By increasing the concentration expansion coefficient, the Grashof number increases, erosion distance decreases, as well as the volume of dissolved materials. As the concentration expansion coefficient varies $\pm 20\%$, the erosion distance varies by $\pm 2.4\%$, the volume of dissolved material varies by $\pm 0.56\%$.

5.3.3 Reynolds number:

The effect of Reynolds number can be evaluated by keeping the Marangoni number and Grashof number constant and varying the Reynolds number. To keep the Marangoni number constant, while varying Reynolds number, υ' has to be varied and keep γ', $\triangle c'$, L', and μ' constant. Since $\upsilon' = \frac{\mu'}{\rho'}$, to vary υ' and keep μ' constant, ρ' has to be varied.

Grashof $Gr_c = \frac{\beta_c g' L'^3 (c_s' - c_b')}{\upsilon'^2} = \frac{-\frac{1}{\rho}\frac{\partial \rho}{\partial c} g' L'^3 (c_s' - c_b') \rho'^2}{\mu'^2} = \frac{-\rho' \frac{\partial \rho}{\partial c} g' L'^3 (c_s' - c_b')}{\mu'^2}$, to keep the Grashof number constant, $\rho' \frac{\partial \rho'}{\partial c'}$ needs to be constant, as ρ' varies, $\frac{\partial \rho'}{\partial c'}$ must vary as well, in opposite direction. As the Reynolds number increases, the erosion distance increases, and the volume of dissolved material decreases. By varying Reynolds number $\pm 20\%$, the erosion distance increases by $\pm 1.30\%$ and the volume of dissolved materials varies by $\pm 0.20\%$

The overall numerical modeling error from the variation of Marangoni number, Grashof number and Reynolds number can be calculated based on the error from each individual number. The cumulative error of erosion distance is calculated as 2.8%, the cumulative error of erosion distance is calculated as 12.4%.

5.4 Performance of the Algorithm

5.4.1 Comparison of maximum corrosion distance between the fixed boundary and the moving boundary:

The algorithm is self-starting and is formally second-order accurate in space and first-order accurate in time. Different assumptions for the top surface and the dissolvable left boundary are studied, as listed in Table 5.2. In all cases in this study, Ma=1.5*10^5, Re=15, Grc=200 are used.

Table 5.2 Cases Studied

Case No.	Dissolvable boundary	Top surface
Case 1	Fixed	Flat
Case 2	Moving	Flat
Case 3	Fixed	Curved
Case 4	Moving	Curved

For fixed boundary and flat top surface case (case 1), the mapping function h(z,t) is kept as 1 and the function describe the top surface hz(r) is also kept as 1, that means the dissolved left rod is kept flat and the top surface also is also flat . A grid test is performed at this condition. In order to resolve the flow condition in the boundary layer, a non-uniform grid is used, close to surface and dissolved rod, a fine grid is used. In the rest of the domain, a coarse grid is used. Figure 5.4 illustrates the effects of variation of fine grid size on the accuracy of the results at a location close to the surface. The results show that grid size $\Delta\xi = \Delta\eta = 0.0008$ is satisfactory.

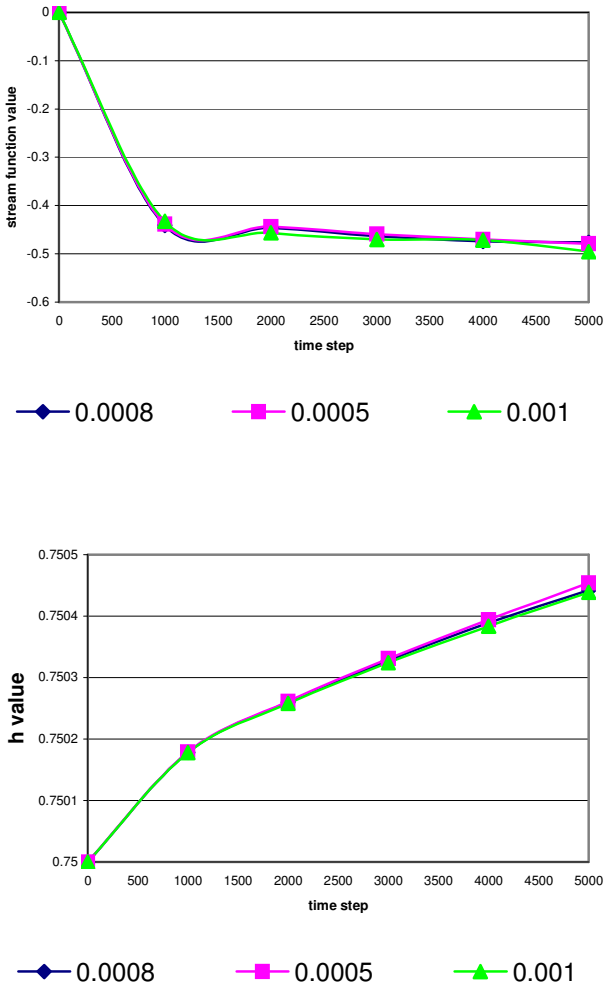

Figure 5.4 Variation of ψ and h at (ξ,η)=(0.8,0.8) at a function of grid size $\Delta\xi,\Delta\eta$.

Figure 5.5(A) illustrates the flow pattern for fixed boundary and flat top surface case (case 1). The positive Ma number corresponds to a system in which the presence of solid species increases surface tension of the liquid. Marangoni flow arises from the surface tension gradients appearing is the liquid. The direction of the flow is from low surface tension to high surface tension. As the melt close to the left side rod has higher

concentration of solid species, it has a higher surface tension. Then, the flow is driven toward the refractory rod, and towards the left, thus creating steep velocity gradients at the surface due to viscous shear effect. Fresh melt material from the bulk is supplied to the refractory rod.

Figure 5.5 (B) shows the concentration field for the constant boundary case (Case 1). The iso-concentration lines are vertical and parallel to the refractory rod if there is no flow in the melt and mass transfer is only by mass diffusion. In this case, due to the steep velocity gradients at the surface, the iso-concentration lines are pulled away from the refractory rod and become horizontal.

Case 2 used moving boundary and flat top surface, which involves the complete problem: the mapping function H(z,t) is determined from the overall dynamics of the liquid, also the effect of the corrosion profile on the flow field is included in the calculation. The flow pattern and concentration fields for this case are shown in Figure 5.5(C) and Figure 5.5(D). Compare Figure 5.5 (A,B) with Figure 5.5(C,D). The flow in the moving boundary case is closer to the dissolvable rod, since after the dissolution of the solid rod, the liquid will move to fill the dissolved space. Due to the moving boundary effect in the flow field, the case of moving boundary has lower iso-concentration lines, which means that in the moving boundary case, the dissolved solid materials disperse faster into the liquid melt than the case of constant boundary. The differences in the flow and concentration fields affect the erosion profiles, which will be discussed later.

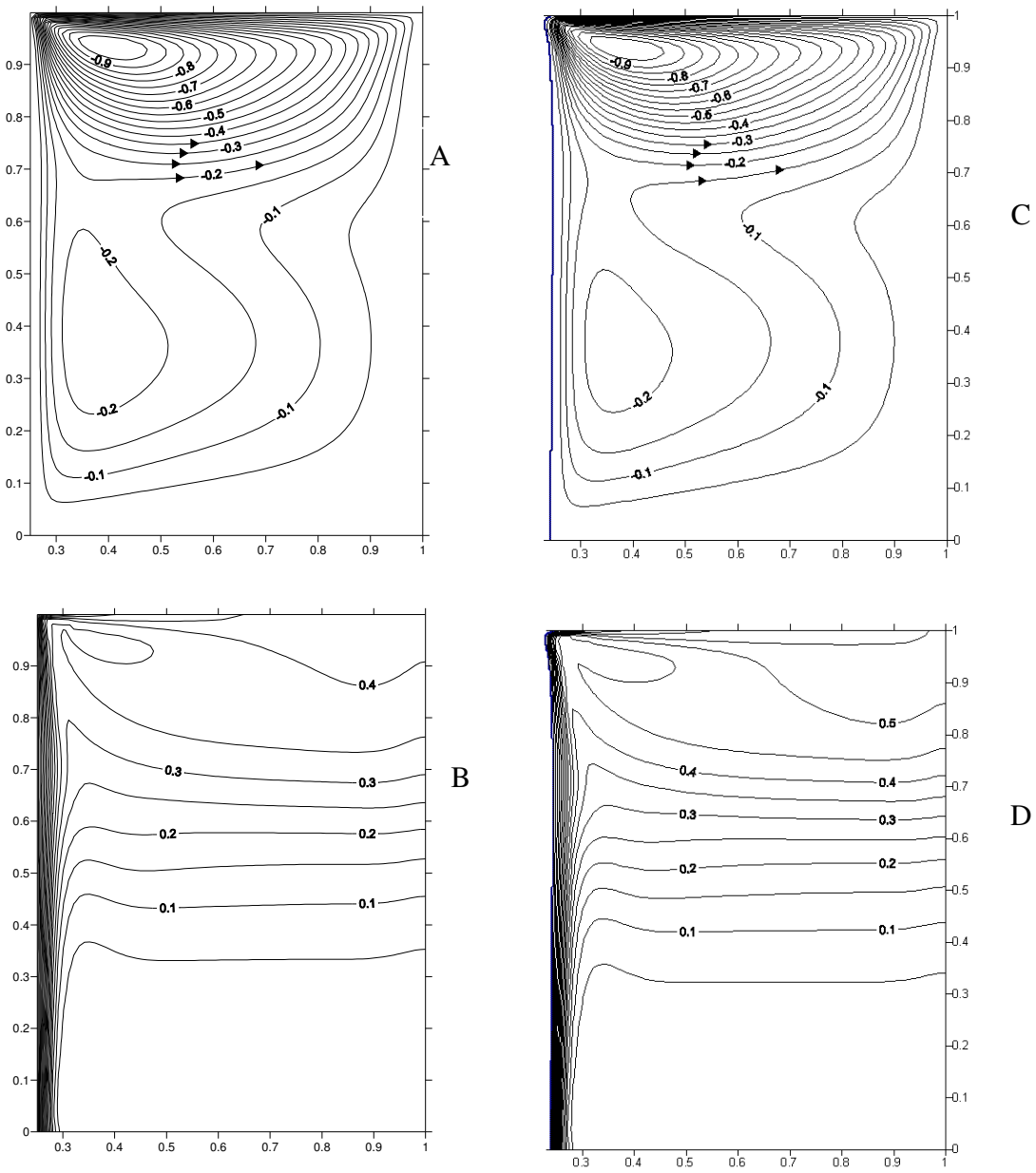

Figure 5.5 Flow field and concentration field at 20 min

Case 1 A: flow field for constant boundary, B: concentration field for constant boundary

Case 2 C: flow field for moving boundary, D: concentration field for moving boundary

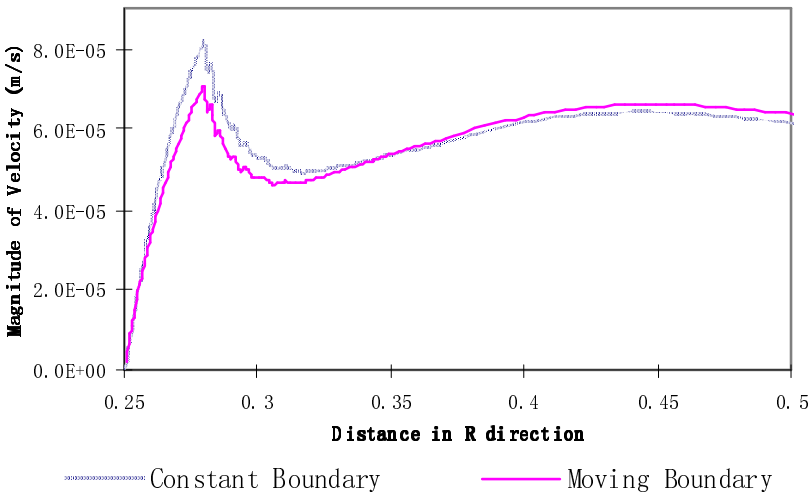

Figure 5.6 Magnitude of velocity distributions at ξ=0.8

In order to examine the velocity differences in constant boundary and moving boundary cases, the velocity distributions at ξ=0.8 are plotted at Figure 5.6. The figure shows the maximum velocity for constant boundary case is about 15% higher than the moving boundary case. The velocity differences in these two cases is caused by the shape of the eroded rod. The moving boundary case results a curved surface on the rod, which reduced the fluid velocity in the field. This result can be used to explain the results in the maximum erosion distance, which will be discussed next.

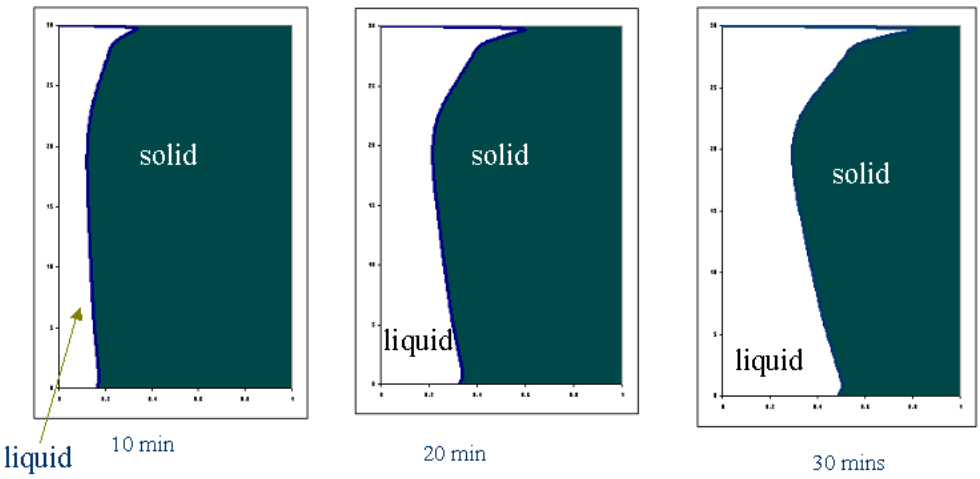

Figure 5.7. The erosion profiles as a function of time for the case of moving boundary and flat top surface (case 2)

The erosion profiles as a function of time for the case of moving boundary are shown in Figure 5.7. Results indicate that, the dissolvable rod is corroded all along the vertical direction, and the maximum erosion is located at the top, just below the fluid surface, which is caused by the Marangoni flow. There is also some erosion at the lower part of the rod casued by density driven buoyancy flow, and less than the corrosion at the slag-line. The maximum erosion distance as a function of time in the constant and moving boundary cases is shown in Figure 5.8. The two results show a significant difference in the maximum erosion after 20 minutes, indicating that the shape of the eroded rod has a big effect on the flow field, and hence, on the refractory erosion rate. Figure 5.6 shows that the maximum fluid velocity for the constant boundary is 15% higher than the moving boundary. Since a diffusion controled process is assumed, the reduced velocity field will result a smaller corrosion rate, which explains the result of Figure 5.8.

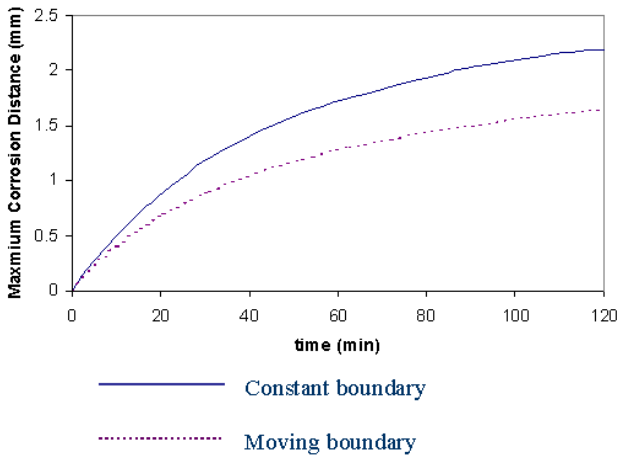

Figure 5.8 Compare the maximum corrosion distance as a function of time between constant boundary (case 1) and moving boundary (case 2)

5.4.2 Comparsion the maximum corrosion distance for the cases of curved surface (Case 3) and flat surface (Case 1):

Experiments have been carried out to determine the shape of the top surface. Experiments was conducted by using cylindrical a MgO crucible containing Al_2O_3-CaO slag at 1600^oC in a furnace equipped with X-ray imaging. The shape of the top surface can be recorded from the X-ray photos. Figure 5.9 shows a typical X-ray photo at time 5 minutes. The shape of the top surface has been digitized and expressed as the function hz(r). In this case study, the hz(r) function remained constant over time. This function was then used to describe the shape of top surface of the slag in numerical simulation of erosion of the MgO rod.

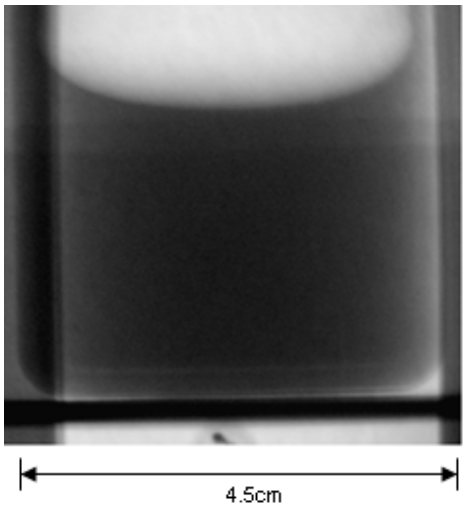

Figure 5.9 X-ray picture shows the curved surface

Case 3 study involves the use of a constant pre-defined curved surface in the numerical algorithm. The effect of moving boundary is suppressed, in order to examine the effect of the curved surface and wetting behavior on the slag-line corrosion phenomenon. hz(r) obtained from the experiments has been used in flow field calculations. The flow pattern and concentration field result from this case are shown in Figure 5.10 (A,B). Comparing Figure 5.5 (A,B) with Figure 5.10 (A,B), shows that the case 3, which used curved surface, has lower iso-stream lines, which means that in the curved surface case, the dissolved solid materials disperse faster into the liquid melt than in the case of flat surface. This difference in the flow and concentration fields is expected to affect the erosion profile.

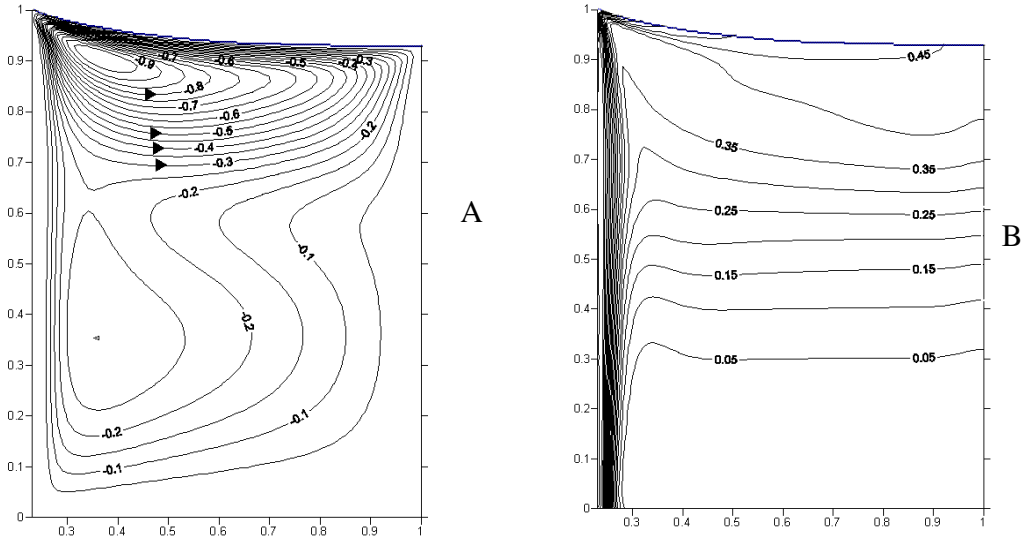

Figure 5.10. Flow field and concentration fields at 20 mins for the curved surface case.

Case 3 A: flow field, B: concentration field

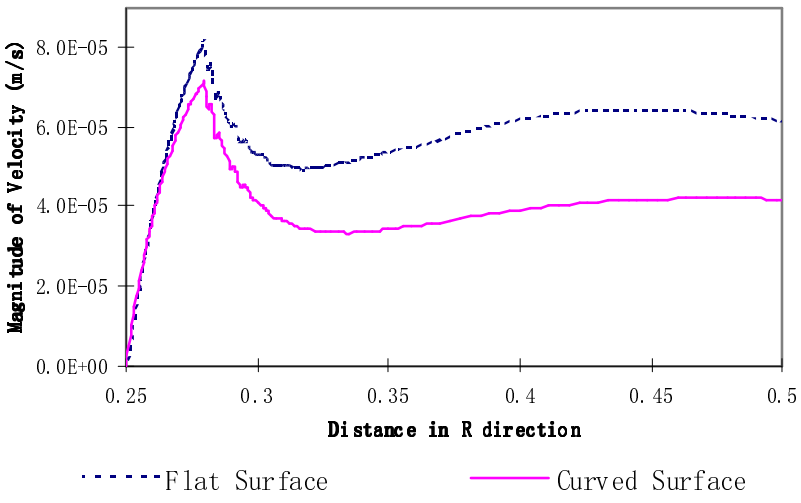

Figure 5.11 Magnitude of velocity distribution at ξ=0.8

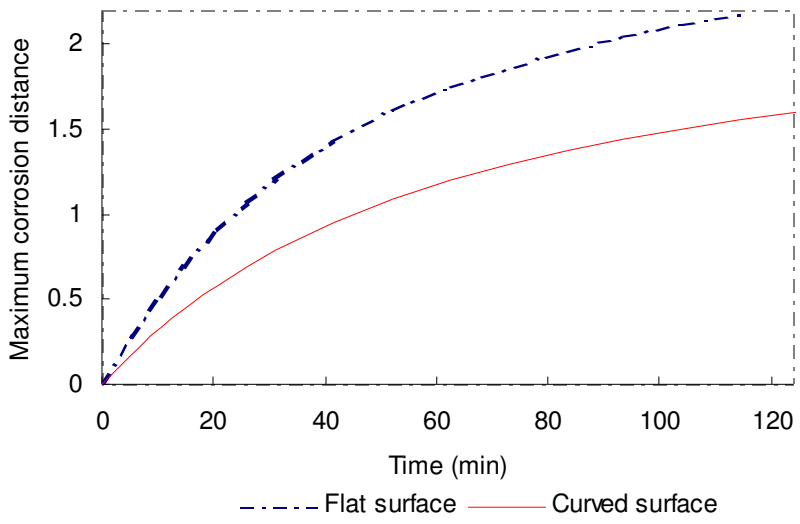

Figure 5.12 Compare the maximum corrosion distance as a function of time between flat top surface (case 1) and pre-defined top surface (case 3)

The velocity distributions at ξ=0.8 for both cases are plotted in Figure 5.11. It is shown in this figure that the magnitude of velocity for the curved surface is lower than the magnitude of velocity for the flat surface case. The maximum velocity difference is as high as 50%. This result shows that the shape of the top surface has a significant effect on the velocity field, and hence on the corrosion rate, which is presented in Figure 5.12, Figure 5.12 shows that the maximum erosion distance for the curved surface case is much lower than the flat surface case. This can be explained by the lower velocity field shown in Figure 5.11. The lower velocity field reduces the stirring effect in the liquid. Since it is assumed that the process is diffusion controlled, the lower stirring results in a lower erosion rate.

5.5 Conclusion

The algorithm for analysis of unsteady Marangoni convection in refractory slag line dissolution developed in Chapter 4 is examined. Comparison of the computational model results and experimental results show that this model can predict the refractory maximum corrosion distance caused by Marangoni flow at the slag line. From the comparison, the corroded material volume shows 20~30% deviation. The shape of the lower part of the corroded rod also shows a significant difference between experimental and numerical results. These deviations are caused by the assumption of a fixed position of the top surface and the uncertainty of slag properties. Numerical results show that the Marangoni effect plays a very important role in slag-line erosion. The comparison of different cases studied shows that both the moving boundary condition and curved surface condition have significant effects on the slag-line erosion rate, and therefore should be included in any model of slag line erosion. Given the effect of including surface curvature, it seems likely that allowing this curvature to move with erosion would have a significant effect and should be included in future work. This change is also likely to improve agreement between the predicted corrosion profile and that observed by experiment.

Chapter 6 General Discussion and Conclusions

Two experimental systems have been studied in order to analyze the erosion mechanism of refractory at the slag-line; MgO refractory in SiO_2-CaO-FeO_x-MgO slag and Al_2O_3-SiO_2-CaO-FeO_x-MgO. The experiments were conducted at 1530^oC for 15min to 90min. The change of MgO concentration with time was observed. There was significant evidence of a spinel phase formed at the slag/refractory interface for slags containing 20wt.% Al_2O_3. This existence of the spinel seems to have retarded the dissolution of the refractory. The mass transfer coefficient has been found for this system. The corrosion of MgO refractory in the CaO-Al_2O_3 slag system was studied at 1575^oC- 1650^oC from 30min to 150min. the decrease in erosion rate in the presence of spinel is in proportion to the decrease in the equilibrium MgO concentration at the slag/solid interface. This result indicates that the indirection dissolution rate is thermodynamic in origin rather than due to the diffusion behavior offered by other workers. The change of MgO concentration with time was observed. The kinetics of the dissolution process was examined. The effective mass transfer coefficients are calculated by kinetic analysis. The activation energy is calculated from the relationship of effective mass transfer coefficient vs. temperature. The activation energy is found in the range of mass transfer activation energy and much smaller than the chemical reaction activation energy. These results provide evidence the MgO erosion process is controlled by mass transfer.

An effective algorithm for analysis of unsteady Marangoni convection in refractory slag line dissolution has been developed. Results from the computation show that the

Marangoni effect plays a very important role in slag-line erosion at this condition; both the moving boundary condition and curved surface condition have significant effects on the slag-line erosion rate. The comparison of experimental and numerical results shows that the model can predict the refractory maximum corrosion distance caused by Marangoni flow at the slag line. However, the eroded material volume was predicted within 20~30% deviation. From prediction, the shape of lower part of the eroded rod also shows a difference between experimental and numerical results. The reasons for these deviations are the assumption of fixed curvature and position of the top surface, the assumption of a constant contact point at the slag line, and the uncertainty of slag properties at high temperatures.

The study gives a reasonable prediction of the refractory erosion by Marangoni induced flow. It is proved by this study that the shape of eroded rod and the shape of top surface of the fluid are very important when modeling refractory erosion, neither of these have included in any previous studies on this topic.

Since this study did not allow the position and curvature of the top surface to change, it is one of the sources of error. As is the case with the developing of flow field and concentration field, the shape of the top surface should deform accordingly. Future work should include numerical modeling which allows the shape and the position of the top surface to deform during the dissolution process.

References

1. Richardson, F.D., *Interfacial Phenomena and Metallurgical Processes.* Canadian Metallurgical Quarterly, 1982. **21**(2): p. 111-119.
2. Scriven, L.E. and C.V. Sternling, *The Marangoni Effects.* Nature, 1960. **187**: p. 186-188.
3. Brimacombe, J.K. in *the Richardson conference*. 1974. Tait: The Institution of Mining and Metallurgy.
4. Egry, I. *Marangoni, Mills and Microgravity*. in *Mills Symposium*. 2002. London: The Institute of Materials.
5. Turkdogan, E.T., *Fundamentals of Steelmaking*. 1996: Maney Publishing.
6. Geiger, G.H. and D.R. Poirier, *Transport Phenomena in Metallurgy*. 1973. Reading, MA, Addison-Wesley Publishing.
7. Eisenhuttenleute, V.D., *Slag Atlas*. 1995, Verlag Stahleisen Gmbh, Düsseldorf: Woodhead Publishing.
8. Lee, W.E. and S. Zhang, *Melt Corrosion of Oxide and Oxide-Carbon Refractories.* International Materials Reviews, 1999. **144**(3): p. 77-104.
9. Zhang, S. and W.E. Lee, *Use of Phase Diagrams in Studies of Refractories Corrosion.* International Materials Reviews, 2000. **45**(2): p. 41-58.
10. Moore, J.J., *Chemical metallurgy*. 1990, London: Butterworth-Heinemann. 153.
11. Mukai, K., *In-situ observation of slag penetration into MgO refractory.* Scandinavian Journal Metallurgy 2002. **31**: p. 68-78.

12. Sandhage, K.H. and G.J. Yurek, *Direct and Indirect Dissolution of Sapphire in Calcia-Magnesia-Alumina-Silica Melts: Dissolution Kinetics.* Journal of American Ceramic Society, 1990. **73**(12): p. 3633-3642.

13. Sandhage, K.H. and G.J. Yerk, *Indirect Dissolution of Sapphire into Silicate Melts.* Journal of American Ceramic Society, 1988. **71**(6): p. 478-489.

14. Cooper, J.A.R. and W.D. Kingery, *Dissolution in Ceramic Systems 1.* Journal of American Ceramic Society, 1964. **47**(1): p. 37-43.

15. Sandhage, K.H. and G.J. Yurek, *Indirect Dissolution of Sapphire into Calcia-Magnesia-Alumina-Silica Melts.* Journal of American Ceramic Society, 1990. **73**(12): p. 3643-3649.

16. Faghihi-Sani, M. and A. Yamaguchi, *Oxidation Kinetics of MgO-C Refractory Bricks.* Ceramics International 2002. **28**: p. 835-839.

17. Zhang, S., H. Sarpoolaky, and N.J. Marriott, *Penetration and Corrosion of magnesia Grain by Silicate Slags.* British Ceramic Transactions, 2000. **99**(6): p. 248-255.

18. Bates, J.L., *Heterogeneous Dissolution of Refractory Oxides in Molten Calcium-Aluminum Silicate.* Journal of American Ceramic Society, 1987. **70**(3): p. 55-57.

19. Fukuyama, H., J. R.Donald, and J.M. Toguri, *Wetting Behavior between Fayalite-Type Slags and Solid Magnesia.* Journal of the American Ceramic Society, 1997. **80**(9): p. 2229-2236.

20. Zhang, P. and S. Seetharaman, *Dissolution of MgO in CaO-"FeO"-CaF2-SiO2 Slags under Static Conditions* Journal of the American Ceramic Society, 1994. **77**(4): p. 970-976

21. Bose, S. and T.D. McGee, *Corrosion of MgO Single Crystals by BOF Slags.* American Ceramic Society Bulletin, 1978 **57**(7): p. 674-684.

22. Mukai, K., *Wetting and Marangoni Effect in Iron and Steelmaking Processes.* ISIJ International, 1992. **32**(1): p. 19-25.

23. Fagerlund, K., S.Sun, and S. Jahanshahi, *Effect of Marangoni-induced flow on the Rate of Refractory Dissolution in Molten Slags.* Scandinavian Journal of Metallurgy, 2002. **31**(6): p. 359-366.

24. Chung, Y. and A.W. Cramb, *Dynamic and Equilibrium Interfacial Phenomena in Liquid Steel-Slag Systems.* Metallurgical and Materials transactions B, 2000. **31B**: p. 957-971.

25. Mills, K.C. and B.J. Keene, *Marangoni effects in welding.* Philosophical Transactions of the Royal Society A, 1998. **356**: p. 911-925.

26. Beskow, K., N.N. Tripathi, and M. Nzotta, *Impact of Slag-Refractory Lining Reactions on the Formation of Inclusions in Steel.* Ironmaking and Steelmaking, 2004. **31**(6): p. 514-518.

27. Mills, K.C. and S. Sridha. *Interfacial Effects on Iron and Steelmaking Processes*. in *2000 Belton Symposium*. 2000.

28. Ghosh, N.K., D.N. Ghosh, and K.P. Jagannathan, *Oxidation Mechanism of MgO-C in Air at Various Temperatures.* British Ceramic Transactions, 2000. **99**(3): p. 124-128.

29. Kozakevitch, P., *Foams and emulsions in steelmaking.* Journal of Metals, 1969. **21**(7): p. 57-68.

30. Jakobsson, D., et al., *Interfacial Tension Effects on Slag-metal Reactions.* Philosophical transactions of the Royal Society of London. A., 1998. **356**(1739): p. 996-1001.

31. Heiple, C.A. and J.R. Roper, *Mechanism for Minor Element Effect on GTA Fusion Zone Geometry.* Welding Journal, 1982. **61**(4): p. 97-102.

32. Mukai, K. *Local Corrosion of Regractory at Slag Surface*. in *First International Conference on Processing Materials for Properties*. 1993. Hawaii.

33. Mukai, K., *Marangoni Flows and Corrosion of Refractory Walls.* Philosophical transactions of the Royal Society of London. A., 1998. **356**(1739): p. 1015-1026.

34. Mukai, K., J.M. Toguri, and N.M. Stubina, *A Mechanism for the Local Corrosion of Immersion Nozzles.* ISIJ International 1989. **29**(6): p. 469-476.

35. Yuan, Z.F., W.L. Huang, and K.Mukai, *Local Corrosion of Magnesia-Chrome Refractories Driven by Marangoni Convection at the Slag-Metal Interface.* Journal of Colloid and Interface Science, 2002. **253**: p. 211-216.

36. Sun, S., L. Zhang, and S. Jahanshahi, *From Viscosity and Surface Tension to Marangoni Flow in Melts.* Metallurgical and Materials Transactions B, 2003. **34B**: p. 517-523.

37. Fagerlund, K.O. and S. Sun. in *6th International Conference on Molten Slags, Fluxes and Salts*. 2000. Stockholm-Helsinki.

38. Mukai, K., E. Ikeda, and Z. Yu. *Direct Observation of Local Corrosion of Trough Materials at Slag Surface*. in *First International Conference on Processing Materials for Properties*. 1993. Hawaii: TMS.

39. Nightingale, S. and G. Brooks, *Corrosion of MgO by Alumina-containing Slags.* The Journal of Australian Ceramic society 1998. **34**(2): p. 33-38.

40. Hrma, P., *Dissolution of a solid body governed by surface free convection.* Chemical Engineering Science, 1970. **Vol.25**: p. 1679~1688.

41. Tsotridis, G., Journal of Applied Physics, 1997. **81**(3): p. p1231-1243.

42. J.Szekly, V.S.a., *The Effect of Surface Driven Flows on the Dissolution of a Partially Immersed Solid in a Liquid-analysis.* Chemical Engineering Science, 1970. **25**: p. 699-715.

43. Szekely, J. and V. Stanek, *The Effect of Surface Tension on the Dissolution of Solids in Liquid in Laminar Flow-analysis.* Chemical Engineering Science, 1969. **24**: p. 11-24.

44. Dunkl, M. and R. Bruckner, *Corrosion of Refractory Materials by a Container Glass Melt under the Influence of Varisou Convection Flows.* Glastechnische Berichte 1989. **62**(1): p. 9-19.

45. Potschke, J. and T. Deinet. *The Corrosion of Amc-Refractories by Steel and Slag*. in *9th Biennial worldwide Congress on Refractories*. 2006.

46. Potschke, J. and R. Simmat. *Corrosion of Dense Refractories by Glass melts or Slags*. in *9th Biennial Worldwide Congress on Refractories*. 2006.

47. Stanek, V. and J. Szekly, *The Effect of Surface Driven Flows on the Dissolution of a Partially Immersed Solid in a Liquid-analysis.* Chemical Engineering Science, 1970. **25**: p. 699-715.

48. Dunkl, M. and R. Bruckner, *Corrosion of Refractory Material Under the Action of Forced Convection Flow by Means of the Rotating Cylinder Face Area at 1500^{o}C.* GLASTECHNISCHE BERICHTE, 1987. **60**(8): p. 261-267.

49. Floryan, J.M. and H. Rasmussen, *Numerical Methods for Viscous Flows with Moving Boundaries.* Applied Mechanics Reviews, 1989. **42**: p. 323-340.

50. Shyy, W., et al., *Computational Fluid Dynamics with Moving Boundaries*. 2007, Mineola: Dover Publications, Inc.

51. Caboussat, A., *Numerical Simulation of Two-Phase Free Surface.* Archives of Computational Methods in Engineering, 2005. **12**(2): p. 165-224.

52. Busby, T.S. and J. Barker, Journal of the American Ceramic Society, 1966. **49**(8): p. 441-446.

53. Preston, F.W. and J.C. Turnbull, *The Physics of Upward Drilling.* Journal of the American Ceramic Society, 1941. **239**(2): p. 92-105.

54. Bird, R.B. and W. E.Steward, *Transport Phenomena*. 2002: Wiley.

55. Nightingale,S.A., Brooks,G.A., and Monaghan,B.J., *Degradation of MgO Refractory in CaO-SiO2-MgO-FeOx and CaO-SiO2-Al2O3-MgO-FeOx Slags Under Forced Convection.* Metallurgical and Materials transactions B, 2005. **36(4)**: p. 453-461.

56. Stanley Osher¤ and Ronald P. Fedkiwy, Level Set Methods: An Overview and *Some Recent Results*, Journal of Computational Physics, 2001. 169: p. 463-502.

57. R.H. Aiken,U.S. Patent 816142, 1906

58. J.J. Moore: *Chemical Metallurgy*, Butterworth and Co., London, 1990, p. 119.

59. B. Deo and R. Boom, *Fundamentals of Steelmaking Metallurgy*, Prentice-Hall International, New York, NY, 1993

60. Mills, K.C. and Hondros, E.D., Interfacial *Phenomena in High Temperature Processes*, Journal of Materials Science, 2005, 40: p2403-2409

61. Monaghan,B.J. and Nightingal,S.A., *The Effects of an Applied Voltage on the Corrosion Characteristics of Dense MgO*, Engineering, 2010, 2: p496-501

62. H. Fukuyama and Y. Waseda, : *High-Temperature Measurements of Materials*, Springer, 2009, p39-59

Appendix (1)

1.1 Calculation of Ω

$$t1 = \mathrm{Re} \times \Delta\xi$$
$$t3 = hz \times \Delta\eta$$
$$t4 = \Delta\xi \times h^{n+1}$$
$$t5 = \xi_0^{\,2}$$
$$t6 = t3 \times t5$$
$$t9 = (h^{n+1})^2$$
$$t10 = t9 \times h^{n+1}$$
$$t11 = \Delta\xi \times t10$$
$$t12 = \xi^2$$
$$t16 = \Delta\xi \times t9$$
$$t18 = \Delta\eta \times \xi_0$$
$$t22 = \xi \times (h^{n+1}(3) - h^{n+1}(7))/(2 \times \Delta\eta)$$
$$t23 = \Delta t \times \Delta\eta$$
$$t24 = \psi^n(1)$$
$$t27 = \psi^n(5)$$
$$t30 = \Delta\xi \times \Delta t$$
$$t31 = \psi^n(3)$$
$$t32 = h^{n+1} \times t31$$
$$t31 = \psi^n(7)$$
$$t32 = h^{n+1} \times t34$$
$$t38 = hz^2$$
$$t39 = \Delta t \times t38$$
$$t40 = \Delta\eta^2$$
$$t40 = \Delta\xi^2$$
$$t45 = t44 \times \Delta t$$
$$t49 = t9^2$$
$$t53 = \mathrm{Re} \times t44$$
$$t55 = t38 \times t40$$

$$t67 = ((hz(5) - hz(1))/(2\times\triangle\xi))^2$$
$$t68 = \eta^2$$
$$t69 = t67\times t68$$
$$t73 = ((h^{n+1}(3) - h^{n+1}(7))/(2\times\triangle\eta))^2$$
$$t74 = t12\times t73$$
$$t75 = \triangle t\times t40$$
$$t79 = t12^2$$
$$t80 = t79\times t73$$
$$t88 = t9\times t38$$
$$t93 = \xi_0\times\xi$$
$$t98 = t93\times h^{n+1}$$
$$t101 = t69\times t44$$
$$t103 = \xi\times h^{n+1}$$
$$t111 = t12\times\xi$$
$$t112 = t111\times t73$$
$$t113 = t112\times\triangle t$$
$$t118 = \mathrm{Re}\times\xi$$
$$t120 = t118\times(h^{n+1}(3) - h^{n+1}(7))/(2\times\triangle\eta)\times\triangle\xi$$
$$t121 = \triangle t\times h^{n+1}$$
$$t122 = hx\times t40$$
$$t129 = t53\times\triangle t$$
$$t130 = t9\times hz$$
$$t138 = 4\times t39\times t40\times t5 + 4\times t45\times t9\times t5 + 4\times t45\times t49\times t12 + 2\times t53\times t9\times t55\times t5$$
$$+2\times t53\times t49\times t55\times t12 + 4\times t39\times t40\times t12\times t9 + 4\times t69\times t45\times t5 + 4\times t74\times t5$$
$$+4\times t80\times t75\times t9 - 8\times t45\times t10\times\xi_0\times\xi + 2\times t45\times t88\times t40 - 4\times t53\times t10\times t55\times t93$$
$$-8\times t39\times t40\times t98 - 8\times t101\times\triangle t\times\xi_0\times t103 + 4\times t101\times\triangle t\times t12\times 9$$
$$-8\times t113\times t40\times\xi_0\times h^{n+1} + t120\times t121\times t122\times t24 - t120\times t121\times t122\times t27$$
$$-t129\times t130\times\triangle\eta\times t131 + t129\times t13\times\triangle\eta\times t34$$
$$t138 = 1/t137$$
$$t142 = \triangle\eta\times t5$$
$$t144 = 4\times t39\times t142$$
$$t146 = \triangle\eta\times t12\times t9$$
$$t148 = 4\times t39\times t146$$
$$t149 = t23\times t5$$
$$t151 = 4\times t74\times t149$$
$$t152 = t23\times t9$$
$$t154 = 4\times t80\times t152$$
$$t155 = t12\times\mathrm{Re}$$
$$t157 = t10\times t38$$

$$t160 = 4 \times t155 \times_{\triangle} \xi \times t157 \times t18$$
$$t162 = \mathrm{Re} \times t111 \times_{\triangle} \xi$$
$$t166 = 2 \times t162 \times t157 \times_{\triangle} \eta \times h^{n}$$
$$t171 = 2 \times \xi \times ((h^{n+1}(3) + h^{n+1}(7) - 2 \times h^{n+1}) /_{\triangle} \eta^{2}) \times \Delta\xi \times t121 \times t142$$
$$t176 = 8 \times t74 \times_{\triangle} \xi \times t23 \times \xi_{0} \times h^{n+1}$$
$$t182 = 4 \times ((h^{n+1}(3) + h^{n+1}(7) - 2 \times h^{n+1}) /_{\triangle} \eta^{2}) \times \Delta\xi \times t9 \times t18 \times_{\triangle} t$$
$$t186 = 2 \times t118 \times \Delta\xi \times t88 \times t142$$
$$t187 = t1 \times_{\triangle} t$$
$$t188 = hz \times \xi_{0}$$
$$t190 = t187 \times t31 \times t9 \times t192$$
$$t192 = hz \times \xi$$
$$t194 = t187 \times t31 \times t9 \times t192$$
$$t196 = t187 \times t35 \times t188$$
$$t199 = t187 \times 34 \times t9 \times 192$$
$$t200 = -t144 - t148 - t151 - t154 + t160 + t166 + t171 + t176 - t182 - t186 - t190$$
$$+ t194 + t196 - t199$$
$$t203 = 4 \times t112 \times \Delta\xi \times t152$$
$$t205 = t38 \times_{\triangle} \eta$$
$$t208 = 2 \times t30 \times h^{n+1} \times t205 \times \xi_{0}$$
$$t212 = 4 \times \xi \times t73 \times_{\triangle} \xi \times t149$$
$$t218 = 2 \times t111 \times ((h^{n+1}(3) + h^{n+1}(7) - 2 \times h^{n+1}) /_{\triangle} \eta^{2}) \times \Delta\xi \times_{\triangle} t \times_{\triangle} \eta$$
$$t222 = 2 \times t162 \times t49 \times t38 \times_{\triangle} \eta$$
$$t226 = 2 \times t30 \times t9 \times t205 \times \xi$$
$$t229 = 8 \times t39 \times_{\triangle} \eta \times t98$$
$$t232 = 8 \times t113 \times t18 \times h^{n+1}$$
$$t237 = 2 \times t118 \times t4 \times t205 \times h^{n} + t5$$
$$t242 = 4 \times t155 \times t16 \times t205 \times h^{n} \times \xi_{0}$$
$$t244 = t1 \times_{\triangle} t \times t34$$
$$t245 = t12 \times (h^{n+1}(3) - h^{n+1}(7)) / (2 \times_{\triangle} \eta)$$
$$t246 = (hz(5) - hz(1)) / (2 \times_{\triangle} \xi) \times \eta$$
$$t247 = t246 \times h^{n+1}$$
$$t248 = t245 \times t247$$
$$t249 = t244 \times t248$$
$$t251 = t1 \times_{\triangle} t \times t31$$
$$t252 = t246 \times \xi_{0}$$
$$t253 = t22 \times t252$$
$$t254 = t251 \times t253$$
$$t255 = t251 \times t248$$

$$t256 = t244 \times t253$$
$$t257 = -t203 + t208 - t212 + t218 - t222 - t226 + t229 + t232 + t237 - t242 + t249$$
$$+t254 - t255 - t256$$
$$t280 = t30 \times_{\Delta} \eta \times (t246 \times hx \times t5 - 2 \times t246 \times hx \times t98 + t246 \times hx \times t9 + t22 \times h^{n+1} \times t5$$
$$-2 \times t245 \times t9 \times \xi_0 + t111 \times (h^{n+1}(3) - h^{n+1}(7)) / (2 \times_{\Delta} \eta) \times t10) \times t138$$
$$t282 = 4 \times t16 \times t5$$
$$t285 = 4 \times_{\Delta} \xi \times t49 \times t12$$
$$t288 = 4 \times_{\Delta} \xi \times t69 \times t5$$
$$t290 = 8 \times t11 \times t93$$
$$t291 = \mathrm{Re} \times_{\Delta} \eta$$
$$t292 = t291 \times t24$$
$$t293 = t292 \times \xi$$
$$t294 = t293 \times t292$$
$$t295 = t291 \times t27$$
$$t296 = h^{n+1} \times hz$$
$$t297 = t296 \times \xi_0$$
$$t298 = t295 \times t297$$
$$t299 = t295 \times t293$$
$$t300 = t292 \times t297$$
$$t303 = (hz(5) - hz(1)) / (2 \times_{\Delta} \xi) \times (h^{n+1}(3) - h^{n+1}(7)) / (2 \times_{\Delta} \eta)$$
$$t305 = t303 \times \eta \times \xi_0$$
$$t306 = t291 \times t24 \times \xi \times t305$$
$$t310 = t303 \times \eta \times h^{n+1}$$
$$t311 = t291 \times t24 \times t12 \times t310$$
$$t314 = t291 \times t27 \times \xi \times t305$$
$$t315 = t282 + t285 + t288 - t290 + t294 + t298 - t299 - t300 + t306 - t311 - t314$$
$$t318 = t291 \times t27 \times t12 \times t310$$
$$t321 = 8 \times t69 \times_{\Delta} \xi \times t12 \times t98$$
$$t325 = 4 \times t69 \times_{\Delta} \xi \times t12 \times t9$$
$$t326 = t67 \times \eta$$
$$t330 = 4 \times t326 \times_{\Delta} \xi \times_{\Delta} \eta \times t5$$
$$t331 = t326 \times_{\Delta} \xi$$
$$t332 = t18 \times t103$$
$$t334 = 8 \times t331 \times t332$$
$$t336 = 4 \times t331 \times t146$$
$$t337 = \eta \times (hz(5) + hz(1) - 2 \times hz) / {}_{\Delta}\xi^2$$
$$t338 = t337 \times_{\Delta} \xi$$
$$t340 = 2 \times t338 \times t6$$
$$t344 = 4 \times t337 \times_{\Delta} \xi \times hx \times t332$$

$$t345 = t12 \times t9$$
$$t348 = 2 \times t338 \times t3 \times t345$$
$$t349 = t246 \times_{\Delta} \xi$$
$$t352 = 2 \times t349 \times t18 \times t296$$
$$t356 = 2 \times t349 \times \xi \times_{\Delta} \eta \times t130$$
$$t357 = t318 - t321 + t325 + t330 - t334 + t336 - t340 + t344 - t348 + t352 - t356$$
$$t362 = t144 + t148 + t151 + t14 + t160 + t166 + t171 + t176 - t182 - t186 - t190$$
$$+ t194 + t196 - t199$$
$$t363 = -t203 + t208 - t212 + t218 - t222 - t226 - t229 - t232 + t249 + t25$$
$$+ t237 - t255 - t256$$
$$t368 = -t288 + t290 - t282 - t285 - t300 + t294 + t298 - t299 + t306 - t311 - t314$$
$$t369 = t318 + t321 - t325 + t330 - t334 + t336 - t340 + t344 - t348 + t352 - t356$$
$$t374 = \psi^{n}(3)$$
$$t379 = \psi^{n}(7)$$
$$t404 = t187 \times_{\Delta} \eta \times (-t374 \times h^{n+1} \times t188 + t374 \times t9 \times t192 + t379 \times h^{n+1} \times t188$$
$$- t379 \times t9 \times t192 + t374 \times (h^{n+1}(3) - h^{n+1}(7)) / (2 \times_{\Delta} \eta) \times t252 \times \xi$$
$$- t374 \times (h^{n+1}(3) - h^{n+1}(7)) / (2 \times_{\Delta} \eta) \times t247 \times t12 - t379 \times (h^{n+1}(3) - h^{n+1}(7)) / (2 \times_{\Delta} \eta) \times t252 \times \xi$$
$$+ t374 \times (h^{n+1}(3) - h^{n+1}(7)) / (2 \times_{\Delta} \eta) \times t247 \times t12 - 2 \times t22 \times h^{n+1} \times t3 \times \psi^{n}(0)) \times t138 / 2$$
$$t405 = \psi^{n}(1)$$
$$t410 = \psi^{n}(5)$$
$$t434 = t187 \times_{\Delta} \eta \times (-t405 \times h^{n+1} \times t188 + t405 \times t9 \times t192 + t410 \times h^{n+1} \times t188$$
$$- t410 \times t9 \times t192 + t405 \times (h^{n+1}(3) - h^{n+1}(7)) / (2 \times_{\Delta} \eta) \times t252 \times \xi$$
$$- t405 \times (h^{n+1}(3) - h^{n+1}(7)) / (2 \times_{\Delta} \eta) \times t247 \times t12 - t410 \times (h^{n+1}(3) - h^{n+1}(7)) / (2 \times_{\Delta} \eta) \times t252 \times \xi$$
$$+ t410 \times (h^{n+1}(3) - h^{n+1}(7)) / (2 \times_{\Delta} \eta) \times t247 \times t12 - 2 \times t16 \times hx \times t3 \times \psi^{n}(0)) \times t138 / 2$$
$$t441 = (t5 - 2 \times t98 + t345) / \mathrm{Re} \times t138$$
$$t443 = Gr \times_{\Delta} \xi \times t121 \times t55 \times t441$$
$$t450 = Gr \times (hz(5) - hz(1)) / (2 \times_{\Delta} \xi) \times \eta \times t44 \times_{\Delta} t \times t296 \times_{\Delta} \eta \times t441$$
$$t451 = t24 \times t374$$
$$t454 = t24 \times t379$$
$$t457 = t27 \times t374$$
$$t460 = t27 \times t379$$
$$t463 = t405 \times t31$$
$$t466 = t405 \times t34$$
$$t469 = t410 \times t31$$
$$t472 = t410 \times t34$$

$$t475 = -t451\times t297 + t451\times t293 + t454\times t297 - t454\times t293 + t457\times t297 - t457\times t293$$
$$-t460\times t297 + t460\times t293 + t463\times t297 - t463\times t293 - t466\times t297 + t466\times t293$$
$$-t469\times t297 + t469\times t293 - t472\times t293$$

$$t508 = t460\times\xi\times t305 - t460\times t12\times t310 - t463\times\xi\times t305 + t463\times t12\times t310 + t466\times\xi\times t305$$
$$-t466\times t12\times t310 + t469\times\xi\times t305 - t469\times t12\times t310 - t472\times\xi\times t305 + t472\times t12\times t310$$
$$+t451\times\xi\times t305 - t451\times t12\times t310 - t454\times\xi\times t305 + t454\times t12\times t310 - t457\times\xi\times t305$$
$$+t457\times t12\times t310$$

$$coef(0) = t1\times h^{n+1}\times t3\times(2\times t4\times t6 + 2\times t11\times t3\times t12 - 4\times t16\times hx\times t18\times\xi + t22\times t24$$
$$-t22\times t23\times t27 - t30\times t32 + t30\times t35)\times t138$$

$$coef(1) = -\triangle\eta\times(t200 + t257)\times t138/2$$
$$coef(2) = -t280$$
$$coef(3) = t30\times(t315 + t357)\times t138/2$$
$$coef(4) = t280$$
$$coef(5) = \triangle\eta\times(t362 + t369)\times t138/2$$
$$coef(6) = -t280$$
$$coef(7) = -t30\times(t368 + t369)\times t138/2$$
$$coef(8) = t280$$
$$coef(9) = t404$$
$$coef(10) = -t404$$
$$coef(11) = -t434$$
$$coef(12) = t434$$
$$coef(13) = -t443$$
$$coef(14) = t443$$
$$coef(15) = t450$$
$$coef(16) = -t450$$
$$coef(17) = -t187\times\triangle\eta\times(t475 + t508)\times t138/2$$

$$\Omega^{n+1} = coef(0)\times\Omega^{n}(0) + coef(1)\times\Omega^{n+1}(1) + coef(2)\times\Omega^{n+1}(2) + coef(3)\times\Omega^{n+1}(3) + coef(4)\times\Omega^{n+1}(4)$$
$$+coef(5)\times\Omega^{n+1}(5) + coef(6)\times\Omega^{n+1}(6) + coef(7)\times\Omega^{n+1}(7) + coef(8)\times\Omega^{n+1}(8)$$
$$+coef(9)\times\psi^{n+1}(1) + coef(10)\times\psi^{n+1}(5) + coef(11)\times\psi^{n+1}(3) + coef(12)\times\psi^{n+1}(7)$$
$$+coef(13)\times c^{n+1}(1) + coef(14)\times c^{n+1}(5) + coef(15)\times c^{n+1}(3) + coef(16)\times c^{n+1}(7) + coef(17)$$

1.2 Calculation of c

$$t1 = hz^2$$
$$t2 = Ma \times t1$$
$$t3 = {}_{\triangle}\eta^2$$
$$t5 = {}_{\triangle}\xi^2$$
$$t6 = (h^{n+1})^2$$
$$t11 = {}_{\triangle}t \times t3$$
$$t14 = ((hz(5) - hz(1))/(2 \times {}_{\triangle}\xi))^2$$
$$t15 = \eta^2$$
$$t16 = t4 \times t15$$
$$t17 = {}_{\triangle}t \times t5$$
$$t20 = \xi^2$$
$$t21 = ((h^{n+1}(3) - h^{n+1}(7))/(2 \times {}_{\triangle}\eta))^2$$
$$t22 = t20 \times t21$$
$$t28 = 1/(t2 \times t3 \times t5 \times t6 + 2 \times t1 \times t11 + 2 \times t16 \times t17 + 2 \times t22 \times t11 + 2 \times t6 \times t17)$$
$$t31 = {}_{\triangle}t \times {}_{\triangle}\eta$$
$$t32 = t1 \times \xi_0$$
$$t34 = 4 \times t31 \times t32$$
$$t38 = 4 \times t31 \times \xi \times t1 \times h^{n+1}$$
$$t39 = {}_{\triangle}t \times {}_{\triangle}\xi$$
$$t40 = h^{n+1} \times {}_{\triangle}\eta$$
$$t43 = 2 \times t39 \times t40 \times t1$$
$$t44 = t31 \times \xi_0$$
$$t46 = 4 \times t22 \times t44$$
$$t49 = t31 \times h^{n+1}$$
$$t51 = 4 \times t20 \times \xi \times t21 \times t49$$
$$t53 = Ma \times t20 \times {}_{\triangle}\xi$$
$$t54 = h^{n+1} \times t6$$
$$t58 = 2 \times t53 \times t54 \times {}_{\triangle}\eta \times t1$$
$$t62 = 4 \times t21 \times {}_{\triangle}\xi \times t44$$
$$t65 = 4 \times t22 \times {}_{\triangle}\xi \times t49$$
$$t71 = 2 \times {}_{\triangle}t \times ((h^{n+1}(3) + h^{n+1}(7) - 2 \times h^{n+1})/{}_{\triangle}\eta^2) \times \Delta\xi \times t20 \times {}_{\triangle}\eta \times t6$$
$$t72 = Ma \times \xi$$
$$t74 = t6 \times {}_{\triangle}\eta$$
$$t77 = 2 \times t72 \times {}_{\triangle}\xi \times t74 \times t32$$
$$t84 = 2 \times t72 \times {}_{\triangle}\xi \times t1 \times h^n \times h^{n+1} \times {}_{\triangle}\eta \times \xi_0$$

$$t88 = 2 \times t53 \times t74 \times t1 \times h^{n}$$
$$t89 = Ma \times_{\Delta} \xi$$
$$t90 = \psi^{n}(3)$$
$$t93 = (h^{n+1}(3) - h^{n+1}(7)) / (2 \times_{\Delta} \eta) \times \xi$$
$$t94 = (hz(5) - hz(1)) / (2 \times_{\Delta} \xi) \times \eta$$
$$t95 = t93 \times t94$$
$$t96 = {}_{\Delta}t \times t89 \times t90 \times t95$$
$$t97 = \psi^{n}(7)$$
$$t100 = {}_{\Delta}t \times t89 \times t97 \times t95$$
$$t101 = {}_{\Delta}t \times t89$$
$$t104 = hz \times t101 \times t90 \times h^{n+1}$$
$$t107 = hz \times t101 \times t97 \times h^{n+1}$$
$$t114 = 2 \times_{\Delta} t \times ((h^{n+1}(3) + h^{n+1}(7) - 2 \times h^{n+1}) / {}_{\Delta}\eta^{2}) \times \Delta\xi \times h^{n+1} \times_{\Delta} \eta \times \xi_{0} \times \xi$$
$$t115 = t34 - t38 - t43 + t46 - t51 - t58 + t62 - t65 + t71 + t7 - t84 + t88 - t96$$
$$+ t100 + t104 - t107 - t114$$
$$t117 = \xi \times h^{n+1}$$
$$t119 = 1 / (-\xi_{0} + t117)$$
$$t120 = t119 \times t28$$
$$t129 = (t93 \times h^{n+1} + t94 \times hz) \times_{\Delta} \xi \times t31 \times t28 / 2$$
$$t132 = 4 \times_{\Delta} \xi \times t6 \times \xi_{0}$$
$$t135 = 4 \times_{\Delta} \xi \times t54 \times \xi$$
$$t138 = 4 \times_{\Delta} \xi \times t16 \times \xi_{0}$$
$$t142 = 4 \times_{\Delta} \xi \times t16 \times \xi \times h^{n+1}$$
$$t143 = t14 \times \eta$$
$$t144 = {}_{\Delta}\xi \times_{\Delta} \eta$$
$$t147 = 4 \times \xi_{0} \times t143 \times t144$$
$$t148 = Ma \times_{\Delta} \eta$$
$$t149 = \psi^{n}(1)$$
$$t151 = t148 \times t149 \times t95$$
$$t152 = \psi^{n}(5)$$
$$t154 = t148 \times t152 \times t95$$
$$t157 = t148 \times t149 \times hz \times h^{n+1}$$
$$t160 = t148 \times t152 \times hz \times h^{n+1}$$
$$t164 = 2 \times t94 \times t40 \times hz \times_{\Delta} \xi$$
$$t169 = 4 \times \Delta\xi \times h^{n+1} \times_{\Delta} \eta \times t143 \times \xi$$
$$t171 = \eta \times (hz(5) + hz(1) - 2 \times hz) / {}_{\Delta}\xi^{2} \times_{\Delta} \xi$$
$$t172 = {}_{\Delta}\eta \times hx$$

$$t175 = 2 \times t171 \times t172 \times \xi_0$$
$$t175 = 2 \times t171 \times t172 \times t117$$
$$t179 = -t132 + t135 - t138 + t142 - t147 - t151 + t154 + t157 - t160 - t164 + t169$$
$$+ t175 - t178$$
$$t184 = -t34 + t38 - t43 - t46 + t51 - t58 + t62 - t65 + t71 + t7 - t84 + t88 - t96$$
$$+ t100 + t104 - t107 - t114$$
$$t188 = t132 - t135 + t138 - t142 - t147 - t151 + t154 + t157 - t160 - t164 + t169$$
$$+ t175 - t178$$
$$t193 = c^n(3)$$
$$t196 = (h^{n+1}(3) - h^{n+1}(7))/(2 \times_{\Delta} \eta) \times (hz(5) - hz(1))/(2 \times_{\Delta} \xi) \times \eta$$
$$t198 = c^n(7)$$
$$t209 = t101 \times_{\Delta} \eta \times (-t193 \times \xi \times t196 + t198 \times \xi \times t196 + t193 \times h^{n+1} \times hz - t198 \times h^{n+1} \times hz)$$
$$\times t120/4$$
$$t210 = c^n(1)$$
$$t213 = c^n(5)$$
$$t224 = t101 \times_{\Delta} \eta \times (-t210 \times \xi \times t196 + t213 \times \xi \times t196 + t210 \times h^{n+1} \times hz - t213 \times h^{n+1} \times hz)$$
$$\times t120/4$$
$$t226 = t149 \times t193$$
$$t229 = t149 \times t198$$
$$t232 = t152 \times t193$$
$$t235 = t152 \times t198$$
$$t238 = t210 \times t90$$
$$t241 = t210 \times t97$$
$$t244 = t213 \times t90$$
$$t247 = -t213 \times t97$$
$$t250 = h^{n+1} \times hz$$
$$t259 = -t226 \times \xi \times t196 + t229 \times \xi \times t196 + t232 \times \xi \times t196 - t235 \times \xi \times t196 + t238 \times \xi \times t196$$
$$-t241 \times \xi \times t196 - t244 \times \xi \times t196 + t247 \times \xi \times t196 + t226 \times t250 - t229 \times t250 - t232 \times t250$$
$$+ t235 \times t250 - t238 \times t250 + t241 \times t250 + t244 \times t250 - t247 \times t250$$
$$coef(0) = t2 \times t3 \times t5 \times t6 \times t28$$
$$coef(1) = -_{\Delta}\eta \times t115 \times 120/4$$
$$coef(2) = -t129$$
$$coef(3) = t39 \times t179 \times t119 \times t28/4$$
$$coef(4) = t129$$
$$coef(5) = -_{\Delta}\eta \times t184 \times 120/4$$
$$coef(6) = -t129$$
$$coef(7) = -t39 \times t188 \times t119 \times t28/4$$
$$coef(8) = t129$$

$$coef(9) = t209$$
$$coef(10) = -t209$$
$$coef(11) = -t224$$
$$coef(12) = t224$$
$$coef(13) = -t144 \times Ma \times \triangle t \times t259 \times t120/4$$

$$c^{n+1} = coef(0) \times c^{n}(0) + coef(1) \times c^{n+1}(1) + coef(2) \times c^{n+1}(2) + coef(3) \times c^{n+1}(3) + coef(4) \times c^{n+1}(4)$$
$$+ coef(5) \times c^{n+1}(5) + coef(6) \times c^{n+1}(6) + coef(7) \times c^{n+1}(7) + coef(8) \times c^{n+1}(8)$$
$$+ coef(9) \times \psi^{n+1}(1) + coef(10) \times \psi^{n+1}(5) + coef(11) \times \psi^{n+1}(3) + coef(12) \times \psi^{n+1}(7) + coef(13)$$

1.3 Calculation of ψ

$$t1 = \triangle \eta^2$$
$$t2 = \xi^2$$
$$t3 = ((h^{n+1}(3) - h^{n+1}(7))/(2 \times \triangle \eta))^2$$
$$t4 = t3 \times t2$$
$$t5 = h^{n+1} \times \triangle \xi$$
$$t7 = 2 \times t5 \times t4$$
$$t11 = 2 \times \xi \times t3 \times \triangle \xi \times \xi_0$$
$$t13 = (h^{n+1})^2$$
$$t15 = t3 \times ((h^{n+1}(3) + h^{n+1}(7) - 2 \times h^{n+1})/\triangle \eta^2) \times \Delta \xi \times t13$$
$$t18 = \xi \times ((h^{n+1}(3) + h^{n+1}(7) - 2 \times h^{n+1})/\triangle \eta^2) \times t5 \times \xi_0$$
$$t19 = hz^2$$
$$t22 = 2 \times t19 \times \xi \times h^{n+1}$$
$$t24 = t3 \times \xi \times t2$$
$$t26 = 2 \times t24 \times h^{n+1}$$
$$t28 = 2 \times t4 \times \xi_0$$
$$t30 = 2 \times t19 \times \xi_0$$
$$t31 = t5 \times t19$$
$$t34 = t1 \times t19$$
$$t36 = \xi \times h^{n+1}$$
$$t38 = ((hz(5) - hz(1))/(2 \times \triangle \xi))^2$$
$$t39 = \eta^2$$
$$t40 = t38 \times t39$$

$$t41 = {}_{\Delta}\xi^2$$
$$t51 = t13 \times h^{n+1}$$
$$t54 = t41 \times t13$$
$$t57 = 1/(-t34 \times \xi_0 + t34 \times t36 + t40 \times t41 \times \xi \times h^{n+1} - t40 \times t41 \times \xi_0 + t24 \times t1 \times h^{n+1}$$
$$-t4 \times t1 \times \xi_0 + t51 \times t41 \times \xi - t54 \times \xi_0)$$
$$t62 = (hz(5) - hz(1))/(2 \times {}_{\Delta}\xi) \times \eta$$
$$t69 = 1/(t4 \times t1 + t54 + t34 + t40 \times t41)$$
$$t72 = ((h^{n+1}(3) - h^{n+1}(7))/(2 \times {}_{\Delta}\eta) \times \xi \times h^{n+1} + t62 \times hz) \times {}_{\Delta}\xi \times {}_{\Delta}\eta \times t69/4$$
$$t74 = 2 \times t13 \times \xi_0$$
$$t76 = 2 \times t40 \times t36$$
$$t77 = \eta \times (hz(5) + hz(1) - 2 \times hz)/{}_{\Delta}\xi^2$$
$$t80 = t77 \times hz \times {}_{\Delta}\eta \times \xi_0$$
$$t82 = 2 \times t51 \times \xi$$
$$t88 = 2 \times t40 \times \xi_0$$
$$t87 = t62 \times hz \times {}_{\Delta}\eta \times h^{n+1}$$
$$t88 = t28 \times \eta$$
$$t92 = 2 \times {}_{\Delta}\eta \times t88 \times \xi \times h^{n+1}$$
$$t95 = 2 \times {}_{\Delta}\eta \times t88 \times \xi_0$$
$$t99 = t77 \times {}_{\Delta}\eta \times hz \times \xi \times h^{n+1}$$
$$coef(1) = t1 \times (t7 - t11 - t15 + t18 + t22 + t26 - t28 - t30 - t31) \times t57/4$$
$$coef(2) = -t72$$
$$coef(3) = t41 \times (t74 - t76 - t80 - t82 + t84 - t87 - t92 + t95 + t99) \times t57/4$$
$$coef(4) = t72$$
$$coef(5) = t1 \times (-t7 + t11 + t26 - t28 - t30 + t15 - t18 + t22 + t31) \times t57/4$$
$$coef(6) = -t72$$
$$coef(7) = t41 \times (-t74 + t76 - t80 + t82 - t84 - t87 - t92 + t95 + t99) \times t57/4$$
$$coef(8) = t72$$
$$coef(9) = -(t36 - \xi_0) \times t41 \times t13 \times t34 \times t69/2$$

$$\psi^{n+1} = coef(1) \times \psi^{n+1}(1) + coef(2) \times \psi^{n+1}(2) + coef(3) \times \psi^{n+1}(3) + coef(4) \times \psi^{n+1}(4)$$
$$+coef(5) \times \psi^{n+1}(5) + coef(6) \times \psi^{n+1}(6) + coef(7) \times \psi^{n+1}(7) + coef(8) \times \psi^{n+1}(8)$$
$$+coef(9) \times \psi^{n+1}(0)$$

Appendix (2)

Experimental Error Analysis

In this section, the error analysis is described. The source of error, their error values are presented. From the current experimental study, the following possible sources of error were identified:

Composition of master slag: As stated in Table 3.5, the master slag composition after 3 times re-melt is: CaO: SiO2 = 48: 52. The initial CaO: SiO_2 weight before slag melting is 1:1. The error of the master slag preparation is 4%.

Temperature inside the crucible: The temperature profile in the vertical direction was measured and hot zone is approximately 50mm. the variation in temperature along the hot zone was 4 degree centigrade maximum. The height of the crucible (40mm) is shorter than the length of the hot zone. Thus, the variation of the temperature inside the crucible was expected to be less than 4 degree. There was no temperature changes during the reaction observed from the thermocouple readout.

Chemical analysis of Mg content: Inductively Coupled Plasma (ICP) technique was used to analyze the slag chemistry after reaction. The error from ICP instrument was evaluated after analyzing several standard reference samples and estimated to be 1%. The error from solution preparation (error from weight, dilution process and etc) was found to be

5% maximum. This was obtained from repeating preparation and analysis process on one slag sample.

Maximum corrosion depth: Maximum corrosion depths were measured from the graphs of optical microscopy on the cross section of MgO samples. By using multiple graphs on one MgO sample, 3% of measurement error was found.

The total error on MgO percentage in bulk slag can be calculated as:

$$E_{MgO} = \sqrt{E_{slag}{}^2 + E_T{}^2 + E_{ICP}{}^2} = 6.4\%$$

The total error on maximum corrosion distance calculated as:

$$E_{Dis} = \sqrt{E_{slag}{}^2 + E_T{}^2 + E_{cor}{}^2} = 5.0\%$$